

**The mechanical response to contact of Soda Lime  
Silica float glass and the effects of hydration and high  
temperature**

by

**Jesús Alberto González Rodríguez**



**A thesis submitted for the degree of Doctor of Philosophy**

**Department of Materials Science and Engineering**

**The University of Sheffield**

**January 2015**



## Abstract

The response of the surface of the Soda Lime Silica float glass to contact was studied by means of instrumented indentation. The research was focused on two specific conditions to which the glass can be exposed during manufacturing and use, first, the change in the hardness and elastic modulus of the near surface of glass exposed to different periods of accelerated weathering at 40°C and 95% relative humidity, and second, changes in the mechanical properties at 520, 540 and 560°C, the latter being the glass transition temperature of this type of glass.

There is an extensive literature about the effects that weathering has on the chemical composition of the air and tin sides surfaces of float glass. Nevertheless, research into the mechanical properties of weathered glass is rather limited. In this study it was found that the air side of the float glass showed an evolution of the nanoindentation hardness and elastic modulus with the exposure time, while in the tin side, the change was almost negligible under the same experimental conditions.

Regarding the contact at elevated temperature on glass, it is possible to find several studies in which hardness is reported over a wide range of temperatures from below 0 up to 700°C. There are discrepancies in the reported results at high temperatures due to the different experimental conditions used by the researchers. This study investigated the effect of the testing parameters such as loading and unloading rate, dwell time, and temperature. The creep behaviour was also studied using mechanical models with Maxwell and Kelvin elements. Such models were fitted to the creep curves and explained well the viscoelastic behaviour near the glass transition temperature. The experiments were carried out on a specially developed apparatus, which has the ability to perform micro and macro-indentations with Vickers and Hertzian indenters from room temperature up to 560°C.

## Acknowledgments

I wish to express my gratitude to my academic supervisor Professor Russell J. Hand for his guidance and support during my PhD, and for many interesting discussions about the science of glass. To my Viva examiners, Dr Adrian Leyland and Dr Paul D Warren. To my industrial supervisors, Miguel Arroyo, Baldomero Gardea and Alberto Hernández from Vitro Automotriz S.A. de C.V., who gave me their complete support and trust not only in this important stage of my professional development, but during all the time I have been part of Vitro.

I specially dedicate this work to my wife Tayde, to my daughters Lucia and Lizbeth, and to my parents and sister Maria de la Luz, Alberto and Jessica.

I would like to thank also Professor Moisés Hinojosa Rivera, from the Autonomous University of Nuevo León, for his words of encouragement and advice all these years.

I'm in debt to the following persons for their support during my stay in Sheffield: Rafael Eufrazio, Martin Legarreta, Miguel Juarez, Erhan Kiliç, Hilmi Mayzan, Shengheng Tan, Dean Haylock and Jules Littlefair. I appreciate very much their friendship.

In addition, I thank the Government of México through the CONACYT, and the Institute of Innovation and Technology Transfer of the Government of the State of Nuevo Leon (I2T2), for the scholarship that allowed me to undertake this PhD.

Lastly, I thank the people of the University of Sheffield, the City of Sheffield and the United Kingdom, for sharing with me and my family their culture and the wonderful experience of science.

## **Preface**

### *Why is Glass such an amazing material?*

Glass has accompanied the mankind since the beginning. Ancient civilizations found in naturally occurring glass (obsidian), an outstanding material to make tools, weapons and ornaments by polishing the stones found into the desired shapes; and even was consider as a magic and sacred stone by pre-Columbian civilizations in Mesoamerica.

Most of the glasses we encounter are made of silicates, which is a material found in abundance in the Earth. A remarkable feature of glass is its ability to go from hard to soft smoothly and continuously with temperature, allowing the glass worker to use different techniques to obtain great variety of shapes and objects. With the beginning of glassmaking many centuries ago in different cultures around the world, societies were favoured with the appearance of glass windows, as well as bottles and containers for many other uses. Craftsmen dominated the melting and forming techniques and started to experiment with new additives and processes to add features to the glass such as colour, strength, and to ease the manufacture and create more complex shapes.

Glass technology continued its development and nowadays we find in this material countless and irreplaceable applications in many sectors such as information technology, nuclear, automotive, architectural, food, medicine, energy and aerospace between others. With all this present and future applications of glass, it is exciting to engage in the scientific research and technological development of this material.

My career in glass began 18 years ago while I was still an undergraduate of mechanical and electrical engineering. I joined a glass company and started working as a process engineer in the automotive glass plant. Through the years I held other positions in the company and I learned that every day was different when working with glass, and that, in order to achieve better results and better products, our understanding of this material has to be increased.

*Jesús González Rodríguez, Sheffield, January 2015.*

## Table of Contents

Abstract .....	iii
Acknowledgments.....	iv
Preface.....	v
List of Figures.....	ix
List of Tables.....	xv
1. Introduction.....	1
2. Literature review .....	4
2.1 The glass theory .....	4
2.2 The float process .....	6
2.3 Manufacturing of automotive glass.....	8
2.4 Characteristics of float glass surfaces.....	11
2.5 Hydration of the surface of float glass .....	13
2.6 Indentation and mechanical properties of glass at room temperature .....	16
2.6.1. Blunt or Hertzian indentation .....	17
2.6.2. Sharp Indentation .....	21
2.6.3. Instrumented indentation.....	25
2.7 Properties and surface contact of glass at high temperatures .....	31
2.7.1. The surface contact at high temperature in the industry.....	31
2.7.2. The properties of glass at high temperature .....	33
3. Hydration and mechanical properties .....	42
3.1 Introduction.....	42
3.2 Experimental procedure .....	43
3.2.1. Preparation of hydrated samples .....	43
3.2.2. Nanoindentation.....	44
3.2.3. SEM/EDX analysis .....	47
3.2.4. Hertzian indentation .....	47
3.3 Results.....	48
3.3.1. Nanoindentation and SEM/EDX results .....	48
3.3.2. Hertzian indentation results .....	54
3.4 Discussion.....	55
4. Apparatus for high temperature indentation .....	60
4.1 Description of the apparatus .....	60
4.2 Description of the Data Acquisition Program .....	64

4.3	Calibration and verification procedures .....	65
4.3.1.	Load cell.....	65
4.3.2.	Displacement Sensor.....	66
4.3.3.	Thermocouples .....	66
4.3.4.	Drift rate .....	67
4.3.5.	Tip Area Function .....	68
4.3.6.	Machine compliance .....	70
4.4	Conclusions .....	79
5.	High temperature contact with the glass.....	81
5.1	Introduction.....	81
5.2	Case study of the contact at elevated temperatures in an industrial process.....	82
5.2.1.	Background .....	82
5.2.2.	Analysis techniques and results.....	84
5.2.3.	Discussion and Conclusions.....	88
5.3	Thermal analysis of Soda Lime Silica glass specimens .....	91
5.3.1.	Introduction.....	91
5.3.2.	Dilatometry .....	91
5.3.3.	Differential Thermal Analysis (DTA).....	93
5.4	Design of Experiments in high temperature indentation .....	95
5.4.1.	Introduction.....	95
5.4.2.	Experimental procedure .....	96
5.4.3.	DoE Results .....	96
5.5	Analysis methodology for instrumented indentation at room and high temperatures .....	100
5.5.1.	Room temperature indentations.....	100
5.5.2.	High temperature Vickers and Hertzian indentation.....	101
5.6	Experiments at high and room temperature .....	109
5.6.1.	Sample preparation.....	109
5.6.2.	Experimental procedure room temperature indentation....	110
5.6.3.	Experimental procedure high temperature indentation. ....	110
5.6.4.	Results .....	113
5.7	Discussion.....	135
6.	Conclusions and suggested further work.....	141
6.1	Introduction.....	141
6.2	Hydration and mechanical properties .....	141

6.3 Apparatus for high temperature indentation.....	142
6.4 Indentation at high temperatures .....	143
6.5 Further research work.....	145
References.....	147
Appendix A: Software control interface for instrumented macroindentation.....	159

## List of Figures

<i>Figure 1.1: Thesis Layout.</i> .....	2
<i>Figure 2.1: Manufacturing process of flat glass by the float process.</i> .....	6
<i>Figure 2.2: Tin chamber of a float glass process.</i> .....	7
<i>Figure 2.3: Automotive laminated glass is made of two panes of glass of similar or different thickness and a layer of PVB which can be between 0.76 and 1 mm thick. Solar control films are sometimes included in the lamination along with the PVB. ....</i>	8
<i>Figure 2.4: Manufacturing process of automotive windscreens.</i> .....	10
<i>Figure 2.5: Typical heating and cooling profile of a windscreen in a continuous furnace.</i> .....	11
<i>Figure 2.6: Tin concentration profiles (EPMA) on clear float glass for different glass thicknesses. b) Tin concentration profile (SIMS) for the outer layer of the surface of both top and bottom sides. (after Verità et al. 1992).</i> .....	12
<i>Figure 2.7: Hydronium and sodium concentration profiles in SLS glass hydrated at 90°C for 540 hrs (after Lanford et al. 1979).</i> .....	16
<i>Figure 2.8: Diagram of spherical (blunt) indentation on the glass surface.</i> .....	17
<i>Figure 2.9: Sequence describing the crack system formed under Hertzian indentation (after Lawn 1993).</i> .....	19
<i>Figure 2.10: Morphology of the crack system after Vickers indentation in Soda Lime Silica glass. The schematic shows the general shape of the cracks and the direction of the median/radial and lateral cracks (from Whittle and Hand 2001).</i> .....	22
<i>Figure 2.11: Schematic of an idealised crack system after the Vickers indentation. c depicts the radial cracks that are measured for the toughness calculation (after Ponton and Rawlings, 1989a).</i> .....	25
<i>Figure 2.12: Relation of an arbitrary point in the periphery of a spherical indenter and the radial distance <math>r</math> given in equation 2.12</i> .....	27
<i>Figure 2.13: Relationship between load (<math>P</math>) and contact radius (<math>a</math>) in terms of penetration depth (<math>h</math>) and indenter cone half angle (<math>\alpha</math>).</i> .....	29
<i>Figure 2.14: Young's Modulus of SLS float glass as a function of temperature measured with ultrasonic echography. (After Rouxel 2007)</i> .....	34

<i>Figure 2.15: Studies of Hv as a function of temperature in the range of RT to near and above glass transition temperature for soda lime silica glass.....</i>	<i>36</i>
<i>Figure 2.16: Vickers macroindentation hardness of float glass as a function of the indenter displacement at different temperatures (Wilantewicz and Varner 2008). The lines are only a visual guide. ....</i>	<i>37</i>
<i>Figure 2.17: Variation of viscosity (log) with <math>T_g/T</math> for different glass systems. Fused Silica has a linear variation of viscosity with temperature hence is classified as strong. The other systems exhibit a non-linear variation and are called fragile (after Kurkjian and Prindle 1998).....</i>	<i>38</i>
<i>Figure 2.18: Modulus to Hardness ratio E/H as a function of temperature for SLS float glass. (Kese at al 2008) .....</i>	<i>40</i>
<i>Figure 3.1: Samples inside the weathering chamber .....</i>	<i>44</i>
<i>Figure 3.2: Variation of the contact radius (indenter) as a function of the contact depth.....</i>	<i>46</i>
<i>Figure 3.3: Evolution of nanoindentation hardness of glass exposed to different periods of accelerated weathering conditions (95% relative humidity at 40°C): a) air side and b) tin side of Soda Lime Silica float glass. ....</i>	<i>49</i>
<i>Figure 3.4: Evolution of the reduced modulus of glass exposed to different periods of accelerated weathering conditions (95% relative humidity at 40°C): a) air side and b) tin side of Soda Lime Silica float glass. ....</i>	<i>50</i>
<i>Figure 3.5: Secondary electron images of air side surface of float glass before (a) and after (b) exposure to 12 days of accelerated weathering at 95% relative humidity at 40°C.....</i>	<i>51</i>
<i>Figure 3.6: Images of tin side surface of float glass before (a) and after (b) exposure to 12 days of accelerated weathering at 95% relative humidity at 40°C.....</i>	<i>51</i>
<i>Figure 3.7: X-ray dot maps of a) calcium rich and b) calcium and sodium rich features on the air-side of samples exposed to 12 days of weathering at 95% relative humidity at 40°C .....</i>	<i>53</i>
<i>Figure 3.8: Minimum load required to propagate pre-existing surface cracks on tin and air surfaces as a function of exposure to weathering. Error bars represent +/- 1 standard error from the mean. ....</i>	<i>55</i>
<i>Figure 4.1: Experimental apparatus for the indentation of glass at elevated temperatures. ....</i>	<i>61</i>

<i>Figure 4.2: Interior view of the furnace.</i> .....	62
<i>Figure 4.3: Indenter shapes and measurements a) Vickers, b) tungsten carbide ball</i> .....	63
<i>Figure 4.4: Displacement-Time curve of the indentation test at a maximum load of 50 N with a second dwell time at 5 N in the unloading stage.</i> .....	68
<i>Figure 4.5: Three dimensional image of Vickers indenter tip used in the High temperature experiments.</i> .....	69
<i>Figure 4.6: Profile of Vickers indenter tip obtained from the optical profilometer.</i> ....	70
<i>Figure 4.7: Load-displacement curve adjusted for machine compliance.</i> .....	71
<i>Figure 4.8: System compliance for the indentation test.</i> .....	71
<i>Figure 4.9: Total Stiffness (<math>S_T</math>) for the specimen and the machine</i> .....	73
<i>Figure 4.10: Machine compliance factor (<math>C_m</math>) obtained with the Vickers indentation on Fused Silica</i> .....	74
<i>Figure 4.11: Machine compliance factor calculated with the indentation of Fused Silica at different temperatures. The bars indicate the 95% confidence intervals for the mean.</i> .....	75
<i>Figure 4.12: Loading and Unloading curve of Hertzian indentation on Fused Silica</i> 77	
<i>Figure 4.13: Loading and unloading curves with second degree Polynomial Fitting. Residuals shown in the inset.</i> .....	78
<i>Figure 5.1: Photograph of the two panes of glass over the mould entering the bending furnace. (Courtesy of Vitro Automotriz S.A. de C.V.)</i> .....	82
<i>Figure 5.2: Mould marks can be observed close to the edge of a finished windscreen (labelled with a red circle). The location of the marks correspond to the area that is in contact with the mould ring.</i> .....	83
<i>Figure 5.3: Micrographs of mould marks observed in the optical microscope. Image a) shows residues of foreign elements along with scratch type marks. Images b) and c) show embedded particles with a glossy surface, and image d) shows an opaque embedded particle.</i> .....	84
<i>Figure 5.4: Optical profilometry of an embedded particle in a glass specimen. The profile in the bottom image shows the height of the particle (distance marked between the red and green reference lines), the penetration depth and the profile of the affected area.</i> .....	85

<i>Figure 5.5: Pit on the surface of a mould mark specimen. The red and green lines in the optical profilometer image are aids to measure the depth of the feature from the glass surface. ....</i>	<i>86</i>
<i>Figure 5.6: SEM image of the particle embedded in the glass surface and the principal chemical elements found in the 3 regions analysed by EDX identified with blue circles and labels. ....</i>	<i>87</i>
<i>Figure 5.7: Images of mould contact surface before and after polishing observed with optical microscope. Ra was reduced from 87 to 17 nm. ....</i>	<i>89</i>
<i>Figure 5.8: Dilatometry to determine <math>T_g</math> of SLS float glass used in the experiments of this work. <math>T_g</math> is the intersection of regression lines between low and high sections of the expansion curve. ....</i>	<i>93</i>
<i>Figure 5.9: DTA of SLS float Glass. <math>T_g</math> of 565°C is obtained from the midpoint between the extrapolated onset temperature and the extrapolated end temperature as described in ASTM E1356 (inset). ....</i>	<i>95</i>
<i>Figure 5.10: DoE Main effects plot. The mean of the hardness in GPa is plotted versus the levels of each factor. The Dwell time shows a larger effect in the hardness following by the Loading speed and a negligible effect of the unloading speed. ....</i>	<i>98</i>
<i>Figure 5.11: DoE Interaction Plot. The mean of the hardness (in GPa) can be read in the vertical axis of each chart. The factor and the levels are indicated in the horizontal axes. ....</i>	<i>99</i>
<i>Figure 5.12: Basic mechanical elements used to represent viscoelastic behaviour. a) Spring where the stress is proportional to the strain and the elastic modulus and b) Dashpot, where the stress is proportional to the strain rate and the viscosity (Scherer 1986). ....</i>	<i>104</i>
<i>Figure 5.13: a) Maxwell element, spring and dashpot are arranged in series. b) Kelvin element, spring and dashpot are arranged in parallel. ....</i>	<i>104</i>
<i>Figure 5.14: Stages describing creep of viscoelastic materials. ....</i>	<i>105</i>
<i>Figure 5.15: Four element model, Maxwell + Kelvin. ....</i>	<i>105</i>
<i>Figure 5.16: Furnace cycle for indentation experiments. ....</i>	<i>111</i>
<i>Figure 5.17: Load-Displacement curve of an indentation experiment in SLS glass. ....</i>	<i>113</i>

<i>Figure 5.18: 3D image of a Vickers indentation at room temperature in SLS glass</i>	114
<i>Figure 5.19: Profile of a Vickers indentation at room temperature</i>	115
<i>Figure 5.20: Effect of the testing temperature in the load-displacement curve of a Vickers indentation.</i>	116
<i>Figure 5.21: Effect of dwell time in the shape of the unloading section of the curve.</i>	117
<i>Figure 5.22: Apparent Vickers hardness as a function of dwell time for SLS at 560°C on tin and air sides. Error bars are <math>\pm 1</math> std. error form the mean.</i>	118
<i>Figure 5.23: Vickers hardness as a function of dwell time for 560°C obtained by imaging of the residual imprint. Error bars are <math>\pm 1</math> std. error in the mean.</i>	118
<i>Figure 5.24: Vickers hardness obtained by imaging for the air side as a function of temperature. Dwell time of these experiments was 120s. Error bars are <math>\pm 1</math> std. error in the mean.</i>	119
<i>Figure 5.25: Air side hardness as a function of dwell time for the three experimental temperatures. Error bars are <math>\pm 1</math> std. error in the mean.</i>	120
<i>Figure 5.26: Measured apparent plain strain modulus as function of dwell time at 560°C for tin and air sides.</i>	121
<i>Figure 5.27: Apparent plain strain modulus as a function of dwell time for 520 and 540°C.</i>	121
<i>Figure 5.28: Optical profilometry of an indentation imprint at 520°C and 120 s. dwell time.</i>	123
<i>Figure 5.29: Optical profilometry of an indentation imprint at 560°C and 120 sec dwell time.</i>	124
<i>Figure 5.30: Profilometry of the cross-section of indentations at 22, 520, 540 and 560°C showing the pile-up extent.</i>	125
<i>Figure 5.31: Micrographs of indentations at a) 520°C, b) 540°C and c) 560°C with a dwell time of 60 s.</i>	126
<i>Figure 5.32: Creep data for Vickers indentation at 520°C. The red line is the fitting curve of the Maxwell + 1 Kelvin element model and the residuals are displayed in the inset.</i>	129

- Figure 5.33: Creep curve of Vickers indentation at 520°C and 120s dwell time. The red line is the fitting curve and the residuals plot in the inset indicate good agreement. .... 129*
- Figure 5.34: Indentation creep as a function of temperature for SLS glass. Higher creep rates are observed as the temperature of the test increases. .... 130*
- Figure 5.35: Creep curves of a Vickers indentation experiment with two different loading rates at 560°C and a constant load of 50 N for a dwell time of 120 seconds. .... 131*
- Figure 5.36: Vickers indentation creep curve at 560°C. Fitting curves were obtained with different dwell times. The models calculated after 90s fit better the data than the models obtained at shorter times..... 132*
- Figure 5.37: Vickers indentation creep curve at 520°C. Fitting curves were obtained at different dwell times. The models calculated with 60, 90 and 120 s fit better the data than the fitting curve calculated with 30s..... 133*
- Figure 5.38: Creep curve of Hertzian indentation at 560°C and 150s dwell time. The fitting curve was obtained with a Maxwell + 1 Kelvin element model. Residuals of the fitting are shown in the inset. .... 134*

## List of Tables

<i>Table 2.1: Tin maximum depth and concentration on clear and green glass for different thicknesses manufactured by the float process. (after Pantano et al.1993). Clear glass usually contains less than 0.1% of iron oxide while green glass contains between 0.1and 0.2 % of this oxide. ....</i>	13
<i>Table 2.2: Equivalent cone angles for Berkovich and Vickers indenters.....</i>	30
<i>Table 2.3 Parameters used to obtain the experimental data shown in Figure 2.15.</i>	36
<i>Table 4.1: Movements Routine for the indentation testing apparatus. ....</i>	63
<i>Table 4.2 Load cell verification. ....</i>	65
<i>Table 4.3 Verification of displacement sensor by comparing with readings in the machine display. Values are in <math>\mu\text{m}</math>.....</i>	66
<i>Table 4.4 Verification of thermocouples used in the experimental apparatus. ....</i>	67
<i>Table 4.5 Elastic properties with temperature of Fused Silica and Diamond tip indenter.....</i>	75
<i>Table 4.6 Numerical results of the quadratic fitting to loading and unloading curves. ....</i>	79
<i>Table 5.1: Factors and Levels used in the DoE. Two levels were chosen for loading and unloading speeds and 3 for dwell time. ....</i>	96
<i>Table 5.2: p-values for the studied factors and interaction between them. The R-Sq. of 97.89% indicates that the factors account for most of the variability of the experiment.....</i>	97
<i>Table 5.3 Experimental parameters for Vickers indentation at high temperatures.</i>	112
<i>Table 5.4: Reduced Modulus and Hardness of soda lime silica glass obtained by instrumented macro-indentation. Values are expressed as the mean <math>\pm</math> 1 standard error. ....</i>	114
<i>Table 5.5: Fitting results (scaled h Vs. time) for Maxwell + 1, 2 and 3 Kelvin elements of a Vickers indentation test at 520°C and 120s dwell time.....</i>	128
<i>Table 5.6: Fitting constants for Maxwell +1 Kelvin elements according to equations 5.22 and 5.23. Vickers indentation test at 520°C and 120s dwell time.....</i>	128

<i>Table 5.7: Fitting constants of the Maxwell + 1 Kelvin elements model for indentation creep data at 520, 540 and 560°C, with a dwell time of 120s and a loading rate of 1.6N/s. ....</i>	<i>131</i>
<i>Table 5.8: Effect of loading speed on fitting constants of Vickers indentation. Model Maxwell + 1 Kelvin element at 560°C, 120s dwell time. ....</i>	<i>132</i>
<i>Table 5.9: Fitting constants using the Maxwell + 1 Kelvin element in Hertzian indentation experiments at 560°C and 150s according to equation 5.21. ....</i>	<i>133</i>
<i>Table 5.10 Comparative table of Vickers hardness at 560°C. ....</i>	<i>136</i>

## 1. Introduction

This thesis is a contribution to the research of glass and address an issue related to how surface of Soda Lime Silica float glass responds to contact. This type of glass is used for example in the manufacturing of flat glass, where the resistance of the surface to contact damage is of great importance. The addition of new functionalities, increased quality requirements and more complex shapes represent a challenge to the manufacturing processes. Therefore, scientific research in this field plays an important role in understanding the behaviour of this material during its fabrication and through its usage.

During the production and handling of glass, its surface is exposed to contact with metallic and/or ceramic rollers, with conveyors and grippers and/or with other glass during storage. As a result of the contact, the surface is damaged and depending on the intensity of the damage this could affect the functionality or aesthetics of the final product. The mechanism of damage can involve different variables such as temperature, humidity, contaminants, glass composition, surface chemistry, pre-existing surface stresses, load and time.

The defects on the glass surface that result from contact can have complex shapes and configurations, however, during the evolution of the glass research, especially in the last three or four decades, several experimental techniques have been developed and improved to study the mechanics of contact and to measure the glass properties. Most of the studies in this period have considered sharp and blunt indentation as ways of assessing the mechanical response of the glass surface to contact damage under different conditions.

Some of the mechanical properties that can be measured or correlated with the results of indentation measurements are the elastic modulus, surface stresses, hardness, toughness and viscosity.

The present work is an examination of the response of Soda Lime Silica float glass to contact at ambient and at elevated temperatures near to the

glass transition. As described in the thesis layout in Figure 1.1, two main subjects are studied: first, the hydration and change of the mechanical properties and surface composition of float glass at room temperature; and second, the mechanical properties and viscoelastic behaviour around the glass transition temperature of this composition which is 560°C.

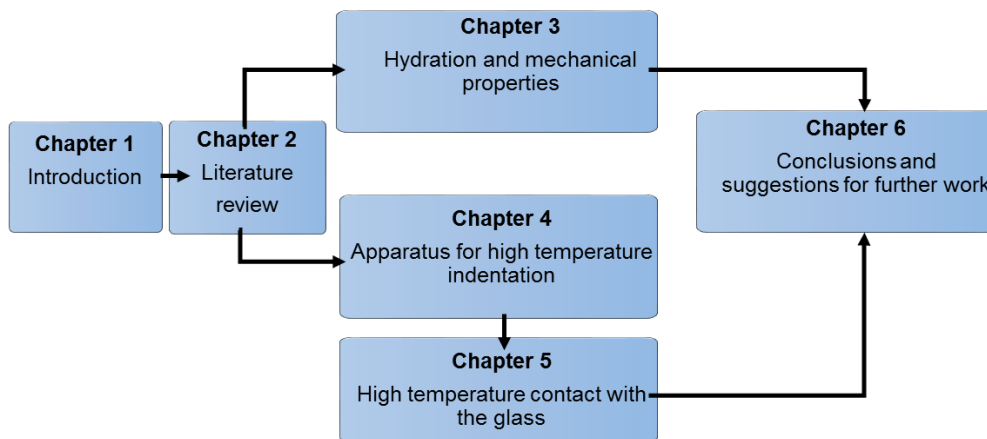


*Figure 1.1: Thesis Layout.*

Both studies are closely related to real conditions during manufacturing, usage and storage of automotive and architectural float glass. It is intended with this work to obtain a better understanding of how the properties of this material vary and to provide experimental values that could be used in further studies to improve manufacturing processes and thus product performance.

The literature review in Chapter 2 starts with a brief description of the manufacturing of flat glass by the float process and the manufacture of automotive windscreens. Knowledge of how the float glass is made is important for the further understanding of the chemical differences that exist on both surfaces of this type of glass. A review of the chemical characteristics of the bulk and the surface of the soda lime silica float glass are provided along with the reactions that occurs during hydration of the surface.

Since most of the experiments in this work are based on the study of the properties through indentation, the techniques of blunt and sharp indentation at room and at high temperatures are described. These have been used to

measure mechanical properties such as hardness, elastic modulus and creep.

Chapter 3 is dedicated to hydration and mechanical properties, the reaction of the water vapour in the environment with the glass surface is studied through nanoindentation and scanning electron microscopy (SEM)/energy dispersive X-Ray (EDX) spectroscopy. These techniques are used to measure and provide a more detailed description of the effect that this reaction has on the hardness and elastic modulus on both surfaces of the float glass.

Experiments at elevated temperatures involving macro-indentations on the surface using an instrumented device were also conducted. These used a specially developed apparatus (described in Chapter 4) to obtain load-displacement curves for which the data was subsequently analysed, and the mechanical properties calculated. Chapter 5 provides a description of the experimental procedures and results, as well as a discussion of this subject.

Final conclusions and suggested further work are provided in Chapter 6.

## 2. Literature review

### 2.1 The glass theory

Strictly speaking, glass is a word that can be used to refer to a wide range of materials and therefore it is not easy to provide a simple definition of it. Glasses can be organic or inorganic, they can be manufactured by melting and cooling, by chemical or deposition procedures, or can be made from different compounds. However, the most significant characteristic is that its state is that of a frozen liquid in which molecular disorder exists in its structure. This state is also called vitreous or glass-like. For the purpose of this study, we will focus on the characteristics of inorganic glasses manufactured by the fusion of oxides in which silica is the principal constituent, and more specifically, on Soda Lime Silica glasses (SLS) made by the float process which is described later in this chapter.

In oxide silicate glasses, when the glass melt is cooled below the glass transition temperature, the atoms do not get enough time to rearrange into a crystalline structure and thus remain in an amorphous state. The liquid-like behaviour of the melt changes to a solid-like behaviour, and therefore to a glass-like or amorphous state within a temperature range, known as the glass transition. The glass transition temperature  $T_g$  is a value within this transition range used to define a point where this phenomenon nominally occurs and is obtained with standardized procedures. During  $T_g$ , the thermal expansion of the glass also changes, being this larger for the liquid than for the solid. Dilatometry is an experimental technique that can be used to measure this change in thermal expansion and therefore to detect the glass transition (see section 5.3.2).

A number of requirements need to be met for the material to reach the glassy state. In the case of oxide glasses, there are several hypotheses that try to address the conditions for glass formation (Varshneya 2006). Perhaps the most accepted is the so called random network hypothesis firstly assumed by Zachariasen (1932) and then widely explained and supported by

the work of Warren (1934) using X-ray diffraction analysis. A number of rules for the glass forming were deduced by Zachariasen as described in the following lines.

Depending on the function that they have in the glass network, the glass components can be: network formers, intermediates and modifiers.

Network formers like Si, B, Ge, As, and P are elements which can build polyhedra networks together with oxygen. The nature of the bond with the oxygen atoms is covalent and they are linked together very strongly resulting in a solid network with outstanding properties.

In silicate glasses, the network-forming cation is  $\text{Si}^{4+}$  which is bounded by oxygen ions forming tetrahedra around them. These oxygen ions may be of two kinds:

- Bridging oxygen ions which link between two polyhedra and,
- Non-Bridging Oxygen (NBO) ions which only link to one polyhedron.

When these polyhedra can arrange themselves adequately, a crystal structure can be obtained (forming quartz or cristobalite). The cooling rate of the melt needs to be very slow to form a crystal, but if this doesn't happen, or because there is a presence of "foreign" element ions interfering with the crystal structure, the glass-like state develops. These "foreign" elements that interfere with the symmetry of the polyhedra structure are called network modifiers and intermediates.

Network modifying ions like Li, Na, K, Ca, Ba, and Sr, balance the charge of NBO. The bond with oxygen is less strong affecting some of the properties; for instance, the viscosity and chemical durability may be decreased.

Intermediates like Al, Zn, Pb, and Ga have an in-between behaviour. Their search for coordination is not strong enough to build a network of polyhedra of their own, but they can be incorporated into an existing polyhedron network of another network former without disrupting it. Their presence in the network increases the viscosity and the chemical durability. Small amounts of

intermediates in the glass network generally will decrease the tendency to crystallize, but at higher concentrations this tendency will increase again.

## 2.2 The float process

Soda Lime Silica glass is commonly used in automotive and architectural products and is manufactured with the float process, developed by the Pilkington Company in the late 1950s in England. Such invention represented a breakthrough in the glass manufacturing industry because it greatly increased the production rates by avoiding the need of grinding and polishing of the surfaces as was required in the other flat glass production processes such as sheet and plate production (Pilkington 1969).

The raw materials used for the melting of Soda Lime Silica glass are primarily sand, limestone, soda ash and dolomite. Other oxides are incorporated as colorants, or refining agents. These raw materials contain the oxides required for the glass fabrication (Tooley 1984). Also, a proportion of cullet (recycled glass) is added to the mix for economic reasons as it lowers the melting point of the batch and reduces the raw material usage.

In the first step of the manufacturing process (Figure 2.1), raw materials are weighed and mixed to form a batch that is fed to the melting furnace which is typically operated at a temperature of 1500°C.

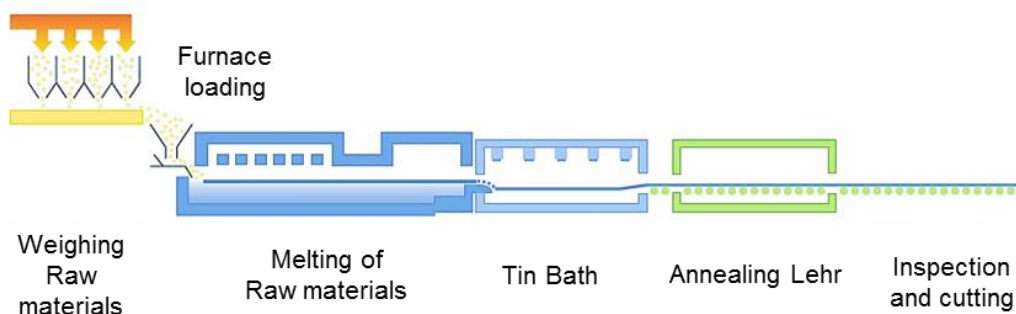


*Figure 2.1: Manufacturing process of flat glass by the float process.*

The melt is stabilized in the melting furnace where gas bubbles are removed (fining) and then is deposited onto a bath of tin at high temperature (Figure 2.2). Because of the difference in density, the glass floats over the

molten tin forming a ribbon with flat parallel surfaces of a given thickness that can be controlled by the residence time and by mechanical devices inside the chamber that restrict the glass lateral spread or by applying forces in the direction of movement. Tin is immiscible with the glass but it oxidises at elevated temperatures, therefore, the bath is enclosed in a temperature controlled chamber with a reducing atmosphere of  $N_2/H_2$  which inhibits oxidation of the tin and the glass surface. The glass ribbon formed on the surface of the tin bath is gradually cooled as it moves through the chamber until the viscosity is sufficiently high to allow it to be lifted and deposited continuously in a roller conveyor that takes it through the annealing furnace. The end product has excellent uniformity of thickness and optical quality.

The surface which was formed in contact with the molten tin is called the “tin side” whilst the upper surface, which was in contact with the chamber atmosphere, is called the “air side”. The contact of the tin side with the molten tin at high temperature results in some incorporation of this element into the surface as we will discuss with more detail in the following section.

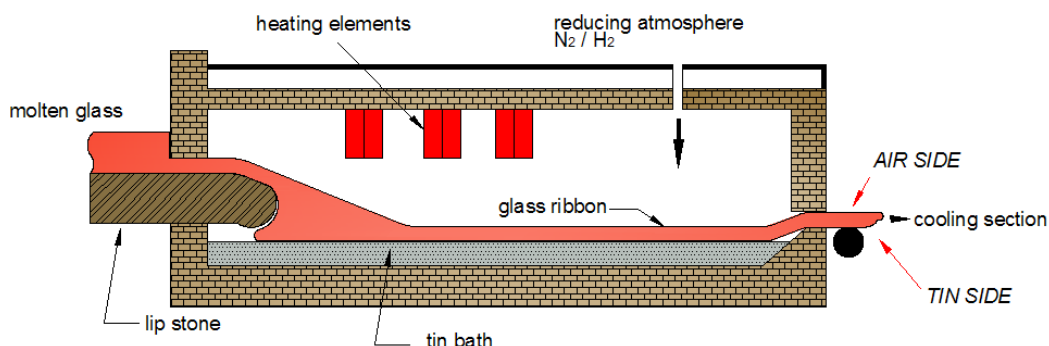


*Figure 2.2: Tin chamber of a float glass process.*

After the glass ribbon exits the float chamber, it enters the annealing furnace where it is transported over steel rollers for approximately 100 meters. In the annealing furnace, the ribbon is cooled gradually to minimize the thermal stresses and reduce the possibility of fracture. In the final stage or cold end, the ribbon is scanned for defects and cut to specific dimensions automatically. Finally, the slabs are stacked vertically in containers usually by automatic manipulators.

## 2.3 Manufacturing of automotive glass.

The glass used in automobiles in modern times fulfils important functions in vehicle performance, aesthetics, comfort and safety. The safety feature is obtained by tempering or lamination.

In tempering, the aim is to obtain a highly resistant glass that in the case of breakage, will break into small, blunt particles that will not exceed a certain size and weight. This characteristic is obtained by heating and forming the glass at temperatures around 620°C and then quenching it rapidly with air to generate compression stresses in the surface which will make it more resistant to impacts. Existing surface flaws will also be less prone to propagation. For fully tempered glass, the surface compression is larger than 69 MPa and is used generally for the doors and rear windows of the vehicles. Door windows can also be laminated and the glass used is semi-tempered or heat strengthened with surface compression stress values between 24 and 52 MPa to provide additional strength to the laminate.

The front glass of the vehicle or windscreen is laminated and the glass is annealed (Figure 2.3), meaning that residual stresses are almost non-existent. This is desired because it will be more flexible and this would help to absorb impacts either from the exterior or the interior in the case of collision. If it breaks, the fragments will remain adhere to each other due to the bonding given by an interlayer of polyvinyl butyral (PVB).

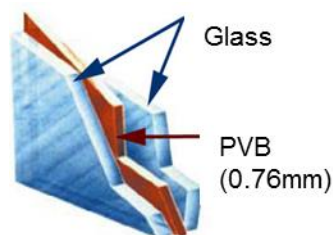


*Figure 2.3: Automotive laminated glass is made of two panes of glass of similar or different thickness and a layer of PVB which can be between 0.76 and 1 mm thick. Solar control films are sometimes included in the lamination along with the PVB.*

Figure 2.4 is a schematic of the manufacturing process of laminated glass. The process starts with the reception of the flat slabs from the float plant and, in the pre-processing stage, the glass is cut to shape and the edges ground

using diamond tools. The next step is the screen printing of a ceramic band usually on the inner layer of the windscreen. This ceramic band hides the adhesive that joins the windscreen to the car body and protects it against degradation caused by the UV rays.

The following phase is the forming and annealing of the two panes of glass. In a process such as the one shown in Figure 2.4, the two layers of glass travel horizontally one on top of the other on a metallic mould that will give the final shape to the windscreen. The glass is heated continuously as it travels inside the furnace until reaching a temperature around 600°C. During this process, the two layers of glass begin to bend under the effect of gravity and heat until they conform to the shape of the mould. A typical heating profile of the glass inside a continuous furnace is shown in Figure 2.5. In this chart, temperature is plotted against time and the different stages of heating and cooling are divided into different colours for a better visualization of the process. A variation of the forming process is so called press bending, in which the glass is pressed by a metallic die from the top in the final stage of the heating section to help it to conform to the mould. After heating, the glass and mould keep travelling through the annealing section where there are heat interchangers with air flowing inside them to gradually cool down the glass. In the last step of this process, the glass is cooled by air nozzles and unloaded from the mould.

In the lamination process, the curved glass is washed again and assembled with the PVB, which has been cut previously to the size of the windscreen. The air remaining in between the assembly is removed using vacuum rings installed around the windscreen, vacuum bags, or by passing the assembly between rubber rolls that will push the air out. The application of heat during this de-airing process provides temporary adhesion of the PVB to the panes of glass. In the following process, the windscreen enters an autoclave where it is exposed to a chamber pressure of around 14 bar and a temperature close to 150°C for around two hours in order to promote the adhesion of the PVB to the glass and make it transparent. In the final stage, brackets and accessories are fitted to the windscreen if required and the final inspection and packaging takes place.

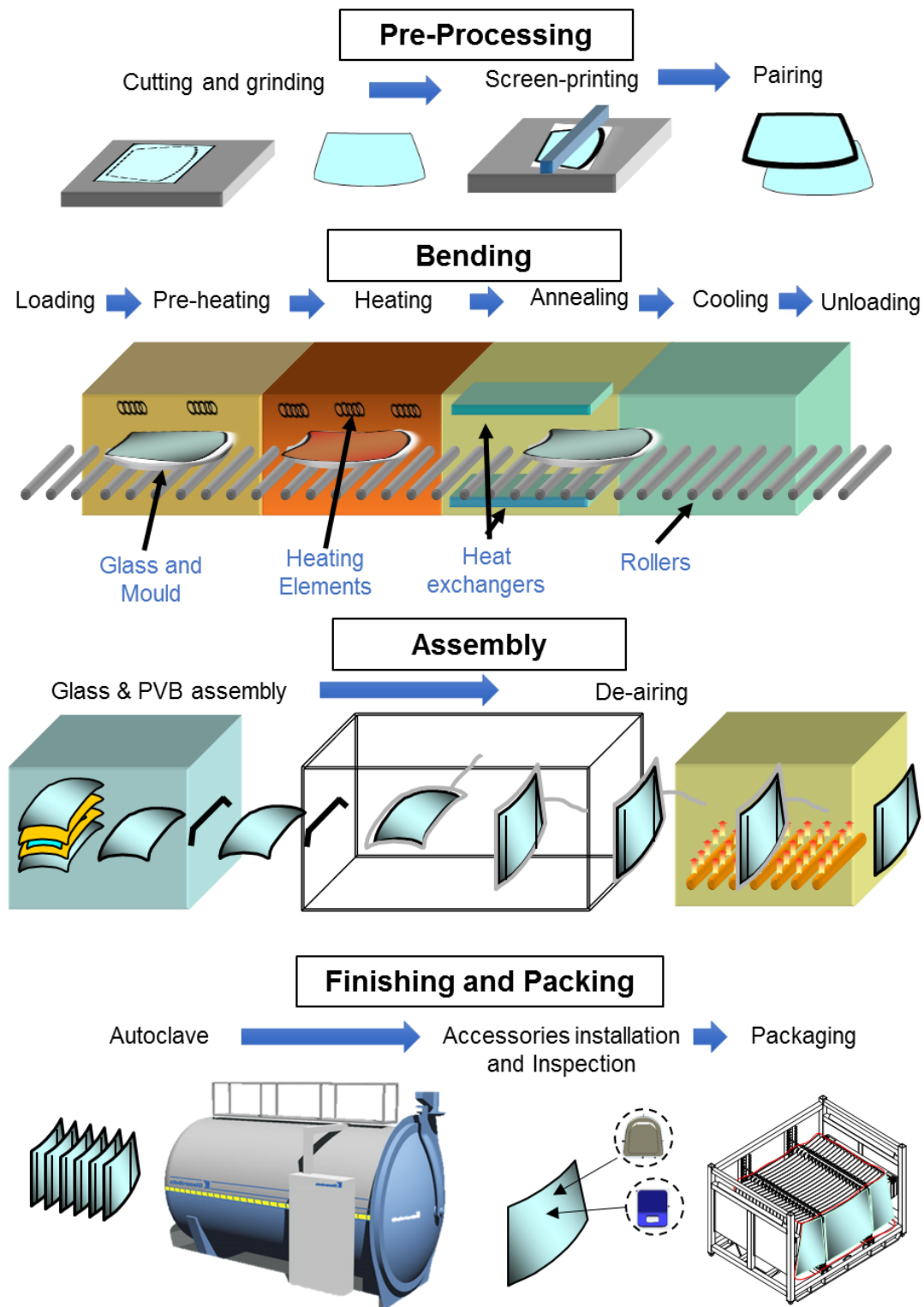


Figure 2.4: Manufacturing process of automotive windscreens.

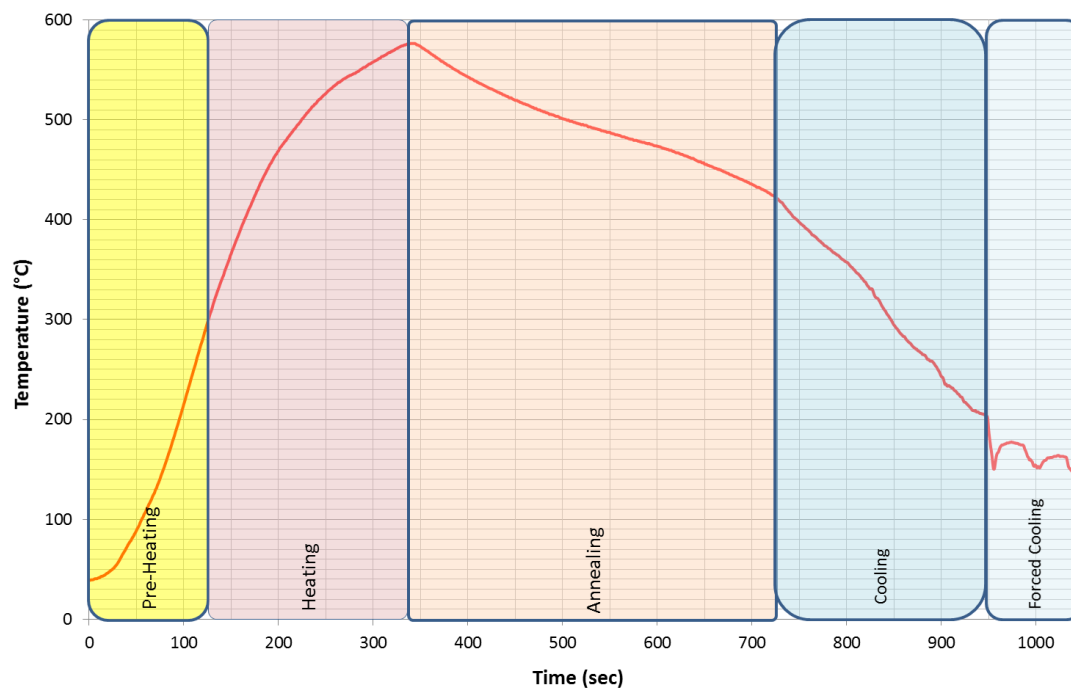


Figure 2.5: Typical heating and cooling profile of a windscreen in a continuous furnace.

## 2.4 Characteristics of float glass surfaces

The typical chemical analysis of green tinted glass manufactured in the float process in % weight is 70-75% SiO<sub>2</sub>; 0-4% Al<sub>2</sub>O<sub>3</sub>; 5-10% CaO; 0-5% MgO; 10-15% Na<sub>2</sub>O; 0-3% K<sub>2</sub>O; 0.86-0.91% Fe<sub>2</sub>O<sub>3</sub> and 0.15-0.18% SO<sub>3</sub>. Clear float glass can be produced by decreasing the iron oxide content to about 0.1% weight and also other colours can be obtained with the addition of metal oxides in proportions less than 1% weight. The addition of these metal oxides do not change the basic physical properties, other than the colour and light transmission. Nevertheless, these changes in optical properties can alter the way that the glass is processed in the forming and annealing furnace. And, as described in section 2.2, both of the surfaces of the float glass have a slight difference in chemical composition because of the contact of the bottom side with the molten tin inside the float tank.

The diffusion of the tin into the surface of float glass has been studied in the past using micro-analytical techniques such as electron microprobe analysis (EPMA) which can provide a measure of the chemical composition

through the depth, secondary ion mass spectrometry (SIMS) that can give a semi-quantitative chemical analysis of the near surface, typically less than one micron deep, and waveguide mode analysis, which is a non-destructive method that uses refractive index changes to assess the diffusion profile of the tin (Verità et al. 1992, Pantano et al. 1993 and Townsend et al. 1998). The quantitative results of those analyses indicate that the penetration of tin can go from 10 to 40 microns into the surface and will depend mainly on fabrication factors such as processing time and temperature profile.

It is known that tin exists in float glass in the form of  $\text{Sn}^{2+}$  and  $\text{Sn}^{4+}$  (Williams et al. 1998),  $\text{Sn}^{2+}$  being more common near the surface. However, for the sake of simplicity, the tin concentration profile in Figure 2.6a is shown for  $\text{SnO}_2$  for different glass thickness in the 30 microns depth range. Traces of tin have also been found in the upper side, but the concentration is almost negligible in comparison with the bottom side as we can see in Figure 2.6b. which shows the concentration profile in the first 500 nanometres depth from the surface.

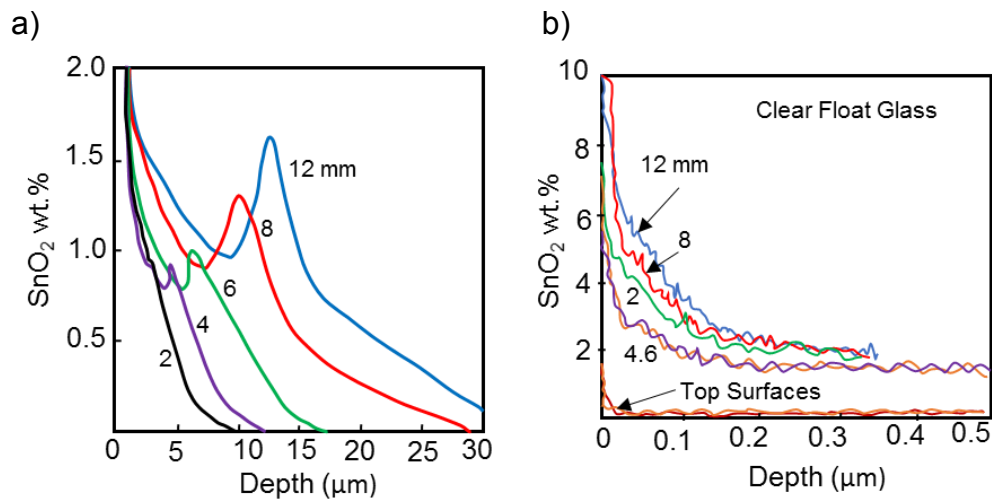


Figure 2.6: Tin concentration profiles (EPMA) on clear float glass for different glass thicknesses. b) Tin concentration profile (SIMS) for the outer layer of the surface of both top and bottom sides. (after Verità et al. 1992).

The processing time of the glass is related to the thickness of the sheet. Table 2.1 illustrates the relationship between the tin concentration and penetration depth of two types of glasses with different iron oxide content (clear and green glass) and different thicknesses. As explained before, a higher content of iron oxide will make the glass greener affecting mainly the

optical and solar properties. An additional feature of these results is that near surface concentration is not related to the thickness, but it is suggested that it is determined mostly in the final part of the process.

*Table 2.1: Tin maximum depth and concentration on clear and green glass for different thicknesses manufactured by the float process. (after Pantano et al. 1993). Clear glass usually contains less than 0.1% of iron oxide while green glass contains between 0.1 and 0.2 % of this oxide.*

Clear Glass				Green Glass		
Sample Thickness (mm)	Contact Time (sec)	Max. Sn Depth ( $\mu\text{m}$ )	Near Surface $\text{SnO}_2$ (%wt)	Contact Time (sec)	Max. Sn Depth ( $\mu\text{m}$ )	Near Surface $\text{SnO}_2$ (%wt)
2.1	150	10.0	6.2	210	9.5	6.0
4	290	12.0	5.0	380	15	4.7
6	460	20	5.4	560	21	3.4
8	570	31	10			
12	880	40	10			

The previous studies in the literature report differences in the concentration profiles of tin for different glass manufactures and colours, basically caused by the manufacturing conditions explained before. However, in all the cases the typical profile is a concentration gradient diminishing as it extends into the bulk with a bulge in the first 5 to 15 microns from the surface as observed in Figure 2.6a. The formation of the bulge is associated with the change of the oxidation state of the glass surface when enters the reducing atmosphere in the float chamber in glasses with high content of  $\text{Fe}_2\text{O}_3$ . There is evidence that the bulge forms at the position where the maximum  $\text{Sn}^{4+}$  exists due to the interaction between the diffusion process of tin and the redox reactions taking place (Frischat et al 2001 and Hayashi et al 2001).

## 2.5 Hydration of the surface of float glass

Although soda lime silica glass is a highly durable material, there is still a reaction with water that is important to consider since this will affect the optical and mechanical properties of the product depending on the type and

conditions of the exposure. Some differences might exist if this exposure is in aqueous solution or by weathering.

Immersion in aqueous solution leads to several stages of reaction (Doremus 1994). Firstly, ions exchange involving hydronium and the alkalis of the glass; secondly, a diffusion of water molecules into the glass and finally, the reaction with the silicon-oxygen network. If the solution is kept static, the water pH increases as result of the sodium ions entering it. Therefore, there is a depletion of the sodium from the surface and this is converted to a more hydrated layer. The reaction rate will be affected by the temperature, glass composition and pH of the solution (Doremus 1979). This process has been extensively studied for nuclear waste borosilicate glasses (Doremus 1981, Ojovan et al. 2005).

The reaction by weathering is of special interest to the glass manufacturers since this is the condition usually seen during storage and service. Depending on the severity of this reaction, the optical and mechanical properties of the surfaces may be degraded. The reaction of recently fabricated glass with water vapour in the atmosphere starts after the production process and continues during the life of the product, but factors such as temperature cycles and high humidity levels accelerate this reaction.

In some cases, water droplets may remain in the surface causing localized attacks similar to those outlined in the reaction with aqueous solutions, but in most cases, the reaction is only with the vapour in which there is no washing away of the alkalis that have migrated to the surface and there is also a deposit of reaction products with contaminants from the environment (Clark et al. 1979).

Studies on the corrosion of soda-lime-silica glass surfaces conducted by Bange *et al.* (2002) and Verità *et al.* (2009) identified the formation of sodium and calcium carbonate on the surfaces following weathering. Other studies have identified sulphates rather than carbonates due to the presence of contaminants such as SO<sub>2</sub> in the ambient environment (Lombardo et al. 2005).

As explained previously for the case of weathering, the hydration process involves interdiffusion of water, probably as  $\text{H}_3\text{O}^+$  (hydronium) and  $\text{Na}^+$  ions leading to the formation of near surface compressive stresses. Hydration of Si-O-Si bonds may also occur ( $\text{Si-O-Si} + \text{H}_2\text{O} \rightarrow 2 \text{Si-OH}$ ). These two phenomena can occur simultaneously or one of them can predominate over the other (Doremus et al. 1983, Scholze 1988). Successive hydration of Si-O-Si bonds leads to the formation of a gel-like structure on the surface. Such a layer may have different mechanical properties such as lower hardness and lower elastic modulus in comparison to the bulk (Tadjiev and Hand 2010). The depth or thickness of the hydrated layer varies with the exposure time and composition. Highly durable compositions exposed to water show negligible variation in their near surface mechanical properties and only a very thin hydrated layer can be detected.

The interdiffusion of the different constituents of the glass with water is time dependent and increases with temperature (Doremus 1981, Lanford et al. 1979), for SLS glass, the sodium is released initially at a rate proportional to the square root of time and reaches a plateau after a long period becoming proportional to time. Figure 2.7 depicts the concentration profiles of hydronium and sodium. It can be observed how the sodium is depleted while the hydronium concentration is increasing reciprocally.

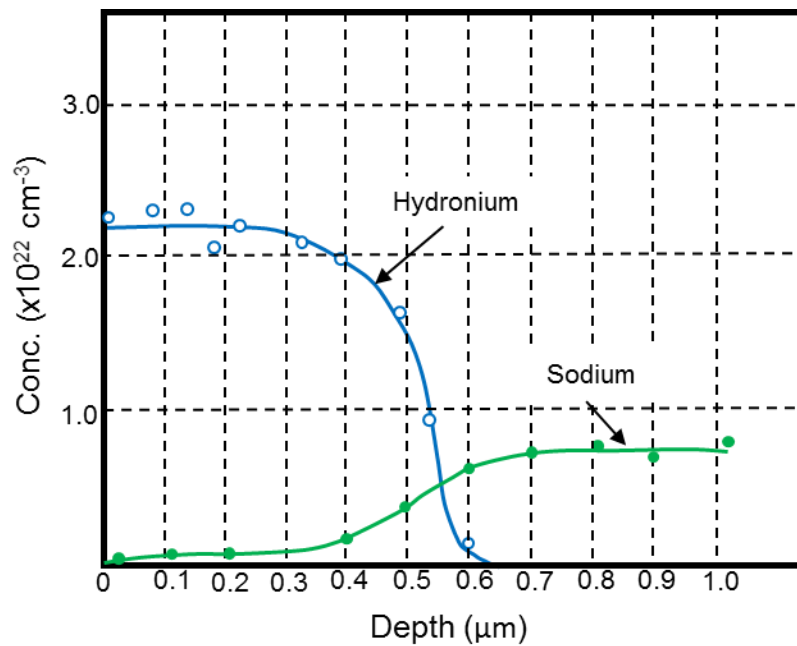


Figure 2.7: Hydronium and sodium concentration profiles in SLS glass hydrated at 90°C for 540 hrs (after Lanford et al. 1979).

## 2.6 Indentation and mechanical properties of glass at room temperature

Indentation is an experimental technique that can be used to measure some mechanical properties of glass such as hardness, elastic modulus, toughness and surface stresses among others. Different types of indenter can be used but the most common are spherical (blunt or Hertzian) and pyramidal (sharp) indenters. In micro and macro-indentation, the indenter reaches one or more microns in depth and is most commonly used to obtain the hardness and toughness by measuring the imprint and the crack length left in the surface by the indenter using an optical microscope. Instrumented indentation has the advantage of providing a load-displacement curve of the indentation experiment that can be analysed and the properties extracted as discussed later in this section. Testing of the surface at the nanometre scale is carried out using nanoindenters which also relies on instruments and sensors to obtain the indentation data avoiding the need of imaging the indents which because of their size is complex and time consuming.

### 2.6.1. Blunt or Hertzian indentation

Hertzian indentation has been used as a tool to obtain different mechanical properties of glass and other brittle materials. Equations have been derived to obtain surface stresses (Roberts et al. 1999, Bisrat and Roberts 2000 and Bao et al. 2002), strength of parts in service (Bao and Gao 2008), and in some occasions for the determination of toughness (Warren 1995, Geandier et al. 2003) as will be discussed subsequently.

In this type of contact, the glass is deformed elastically under the load of a spherical indenter until failure, and the relationship of load and penetration is given by the contact solution developed by Hertz (1896),

$$P = \frac{4}{3} R^{1/2} E_r h^{3/2} \quad 2.1$$

where  $P$  is the load,  $h$  is the penetration,  $R$  is the radius of the sphere and  $E_r$  is the reduced modulus given by the following equation,

$$\frac{1}{E_r} = \frac{1 - \nu_i^2}{E_i} + \frac{1 - \nu_s^2}{E_s} \quad 2.2$$

where  $E$  is the Young's modulus,  $\nu$  is Poisson's ratio, and  $i$  and  $s$  refer to the indenter and the sample respectively.

The deformation of the surface by the load  $P$  is described by the contact radius  $a$  as shown in Figure 2.8.

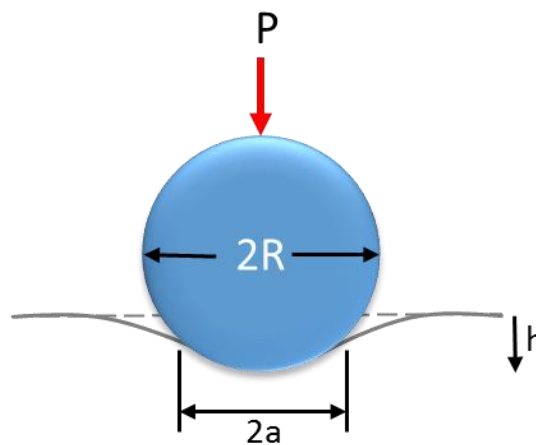


Figure 2.8: Diagram of spherical (blunt) indentation on the glass surface.

The crack system formed by the Hertzian or blunt indentation follows a sequence of events as described below and depicted in Figure 2.9 (Lawn, 1993):

1. At the beginning of the contact of the sphere with the glass surface, starts the development of high compression stresses beneath the sphere and high tensile stresses in the circular area adjacent to contact region.

2. As the load is increased, also the tensile stresses in the contact region increase. At this point, the magnitude of the tension stresses causes the development of a circular or ring crack originating from a pre-existing microscopic flaw in the surface. This crack is normal to the surface and extends a few microns inboard.

3. The circular or ring crack continues growing downward due to the tensile stress fields developed below the surface

4. The cone crack is then formed and propagated when the load reaches a critical value.

5. The cone crack continues growing if the load continues increasing.

6. When the load is removed, the surface tries to recover (elastic recovery), but the ring and the cone cracks leave a distortion near the surface trace of the circular crack.

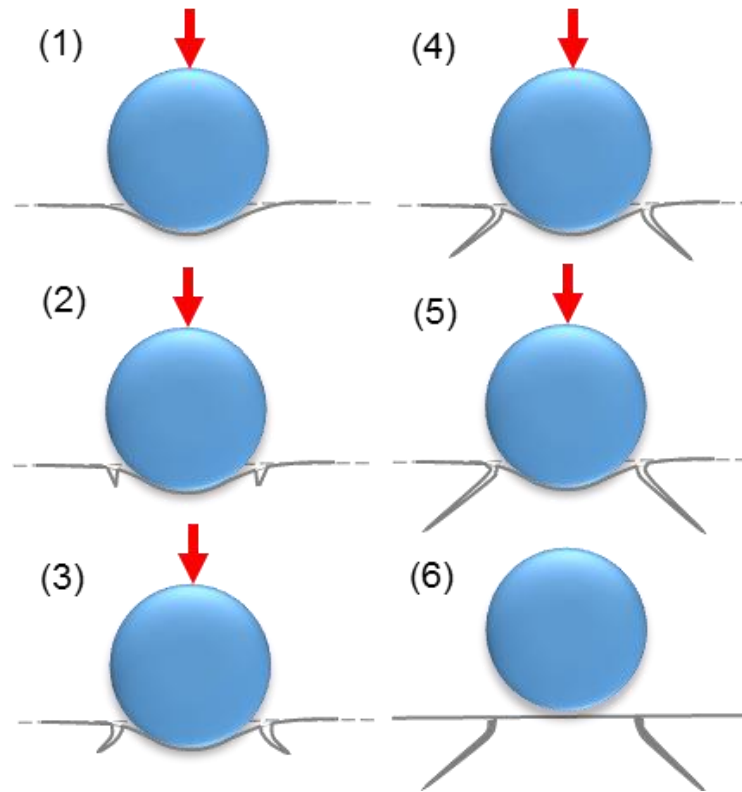


Figure 2.9: Sequence describing the crack system formed under Hertzian indentation (after Lawn 1993).

Glass toughness can be calculated by measuring the crack dimensions after the indentation experiment. Two different approaches have been developed: that of Warren (1995) and Frank and Lawn (1967). The Warren approach is the most practical solution for the toughness calculation. It is based on crack initiation from a pre-existing surface flaw and the critical load necessary to propagate it.

This model correlates the toughness and the critical load using:

$$K_{IC} = \left( \frac{E_r P_{min}}{P_{FN}^{min} R} \right)^{1/2} \quad 2.3$$

where,  $P_{min}$  is the critical load for crack initiation,  $R$  is the indenter radius,  $P_{FN}^{min}$  is a constant that depends on the elastic properties of the sample and the indenter (Young's modulus, Poisson's ratio and friction coefficient between sample and indenter). Roberts et al. (1999) provide  $P_{FN}^{min}$  values for different combinations of indenter and substrate materials.

$P_{min}$  should be obtained directly from the experiment, however, in the case that cannot be detected during the test, this value can be related with the theoretical radius of the contact area  $a$  through the following equation (which corresponds to the Hertzian theory expression explained in more detail in section 2.6.3):

$$P_{min} = \frac{3Ea^3}{4kR} \quad 2.4$$

In this expression,  $E$  is the elastic modulus of the substrate,  $a$  can be estimated with the relation below using the surface crack radius  $r_c$  which can be measured from the ring crack after the experiment.

$$a = \frac{r_c}{\beta} \quad 2.5$$

where  $\beta$  is  $\sim 1.2-1.3$  for most typical Hertzian experiments.  $k$  is defined as:

$$k = \frac{9}{16} \left[ (1-\nu_i^2) + (1-\nu_s^2) \frac{E_s}{E_i} \right] \quad 2.6$$

Here, the subscripts  $i$  and  $s$  refer to indenter and substrate respectively.

Most of toughness results reported in the literature for Soda Lime Silica glass using Hertzian indentation are in the range between 0.7 and 0.8 MPa m<sup>1/2</sup> (Warren and Hills 1994, Warren 1995, Roberts et al. 1999, Geandier et al. 2003). If the indenter and the specimen are made of different materials, a correction factor has to be applied to consider the elastic mismatch between both, as expressed in equation 2.3, otherwise, the  $K_{ic}$  value can be overestimated. An additional consideration should be the surface stresses of the sample since pre-existing compression stresses will superimpose on the stresses generated by the indenter.

One of the problems during the indentation with blunt indenters has been the detection of the crack initiation in order to obtain the minimum load ( $P_{min}$ ) required to calculate the glass toughness. However, the use of acoustic emission monitoring can help to identify the crack initiation since this is an energy release event in the material which emits a high amplitude signal that can be detected by sensors and correlated with load and displacement

during indentation testing using data acquisition software and hardware. Some workers have found reproducible acoustic emission signals during Hertzian indentation at the loading, holding and unloading stages (Kim and Sachse 1984, Faisal et al. 2011). It has been found that the amplitude of the acoustic emission signal is a function of testing parameters such as the cross head speed and indenter size.

The techniques of crack detection consist in attaching an acoustic emission sensor to the glass sample and then performing the indentation. The energy released by the fracture initiation is propagated as an acoustic signal along the surface and will be detected by the piezoelectric sensor. This signal is amplified and sent to a computer for monitoring through a data acquisition card and software.

### **2.6.2. Sharp Indentation**

Under Vickers indentation, a residual impression is left on the glass surface as a result of plastic deformation caused by densification and viscous flow. (Bridgman and Simon 1953, Peter 1970, Lawn and Wilshaw 1975 and Arora et al. 1979). On Soda Lime Silica glasses, densification below the indentation and pile-up around it are observed (Yoshida et al. 2007).

During the indentation, the material adjacent to the plastically deformed zone becomes elastically strained and it remains like that after the removal of the load and the indenter. This zone is called the residual stress field and is related to the initiation and growth of cracks in the indentation site. The residual stress field is a function of the Young's modulus of the material (Lawn et al. 1980).

The fracture system in Soda Lime Silica glass generated under this test has been studied by several authors including Lawn and Swain (1975), Cook and Pharr (1990), Whittle and Hand (2001). Although it has been found that crack system may present some variations depending on the material composition, dwell time or peak load applied (Cook and Pharr, 1990), the following sequence of crack formation during the indentation is representative

for the soda lime silica glass and Figure 2.10 depicts the crack system after Vickers indentation.

1. The plastic deformation starts with the application of the load,
2. When a threshold is reached, an induced flaw nucleates and grow underneath the indenter aligned with the corners, this crack is called median crack.
3. The median crack continues growing as long as the load continues increasing.
4. Unloading starts and the median crack continues to extend up to the surface. However, radial cracks can also nucleate in this stage starting from the corners of the indenter especially at low loads.
5. Lateral cracks parallel to the surface are formed during the late part of the load removal.
6. After the complete removal of the load, the lateral cracks continue to grow and it was found by Whittle and Hand (2001) that they will follow a direction away from the surface due to the residual stress field.

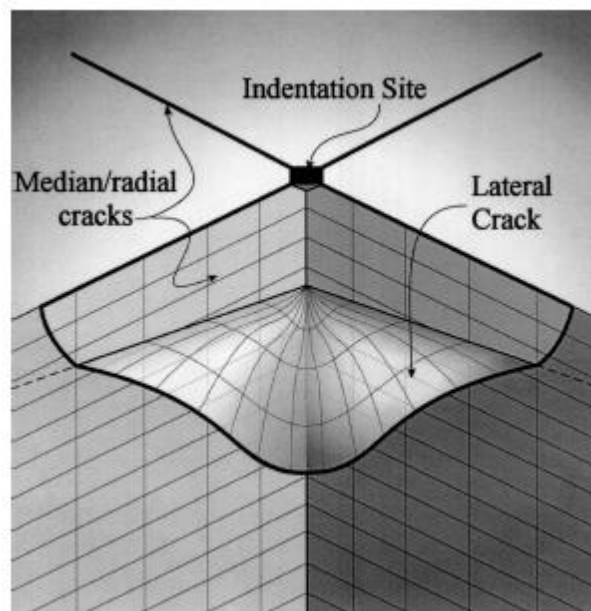


*Figure 2.10: Morphology of the crack system after Vickers indentation in Soda Lime Silica glass. The schematic shows the general shape of the cracks and the direction of the median/radial and lateral cracks (from Whittle and Hand 2001).*

The basic definition of hardness is the resistance of a material to deformation. The Vickers method is commonly used for micro and macro-

indentation of glass and the formula used to calculate the hardness value, generally denoted as  $H_v$  in SI units  $GPa$ , is:

$$H_v = 1854 \frac{F}{d^2} \quad 2.7$$

where  $F$  is the load in Newtons and  $d$  is the average size of the two diagonals of the plastic deformation left by the indenter measured in microns.

The indentation load used in the test defines its nomenclature; nanoindentation is used to characterize very thin films and the load used is usually below the 0.05 Kgf (0.49 N), microindentation is carried out in the range of 0.05 to 1 Kgf (0.49 to 9.81 N) and macroindentation uses loads larger than 1 Kgf (9.81 N).

A typical value of hardness for Soda Lime Silica glass has been found between 5.4 and 6.6 GPa. (Anstis et al. 1981, Le Houerou et al. 2003).

The dependence of the Vickers hardness number in glass is associated with other mechanical properties of the material as the Young's modulus and the average bond strength given by the composition of the material (Yamane and Mackenzie 1974). Thus, glasses compositions that contain oxides, such as BeO, Al<sub>2</sub>O<sub>3</sub> for example, will exhibit larger hardness numbers since the Young's modulus and bond strength of these oxides are large. Recently, Smedskjaer et al (2010) have proposed, based on their experiments, that hardness is also influenced by thermal history, in other words, with increasing annealing time, there will be a reduction of the fictive temperature and an increase of the material's hardness at room temperature because of the increasing structural density. The fictive temperature  $T_f$  is a concept that was initially used to describe the glass state in terms of an equivalent liquid state (Tool 1946), in theory, it is the temperature from which the glass has been quenched rapidly from the melt to freeze the structure in a particular state. Given the previous definition, it might seem that  $T_f$  is a synonymous with the glass transition temperature  $T_g$ . However, while  $T_g$  is a temperature value inside the glass transition range customarily used to indicate the onset of the transition to the glassy state, the fictive temperature can change within the

glass transition range depending on the cooling rate from the melt (Varshneya 1986).

Toughness is a measure of a material's ability to absorb energy before failure. In other words, it is a measure of its resistance to fracture or crack growth. Toughness can be obtained by several experimental techniques such as chevron-notched beam (CNB), surface crack in flexure (SCF) and single-edge pre-cracked beam (SENB) (ASTM C1421-10). Vickers indentation has been also used for this purpose and has been studied by several researchers who have formulated different equations and models to calculate the toughness in ceramic materials from indentation. For this reason, Ponton and Rawlings (1989a), reviewed and standardized nineteen of the most significant papers in order to compare their results on different materials. Nevertheless, for the case of toughness calculation on glasses, the most commonly used equation was developed by Anstis et al. (1981). This equation is described as follows:

$$K_{IC} = 0.016 \left( \frac{E}{H} \right)^{\frac{1}{2}} \frac{P}{c^{3/2}} \quad 2.8$$

where  $E$  is the elastic modulus,  $H$  the hardness,  $P$  is load and  $c$  is the average radial crack length after indentation. This radial crack length is the known as the median/radial crack that nucleates under the indenter perpendicular to the surface and that usually follows the axis of the imprint diagonals as shown in the following schematic.

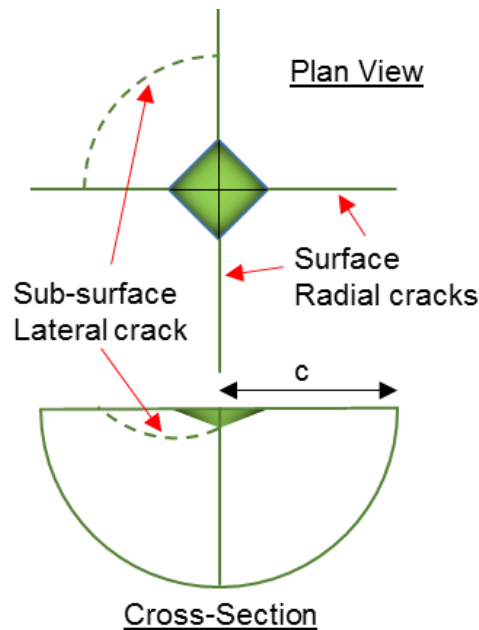


Figure 2.11: Schematic of an idealised crack system after the Vickers indentation.  $c$  depicts the radial cracks that are measured for the toughness calculation (after Ponton and Rawlings, 1989a).

The typical value of toughness for Soda Lime Silica glass using the Vickers indentation test that is reported in the literature is between 0.70 and 0.76  $\text{MPa}\cdot\text{m}^{1/2}$ , (Anstis et al. 1981, Gong et al. 2001, Dériano et al 2004).

The Vickers indentation test has been a widely used method for toughness measurement on glass due to its inexpensive and fast sample preparation and easy equipment set up. Nevertheless, the validity of the test for this purpose on brittle materials has been challenged (Quinn and Bradt 2007) because of the complexity of the crack system caused by the indenter that intervenes with desired clean and fast propagation of a crack, as well as the discrepancies found in the values reported for the same material using the different equations published in the literature (Ponton and Rawlings 1989a,b).

### 2.6.3. Instrumented indentation

Instrumented indentation is a mechanical testing method that uses high resolution sensors and specialized software to continuously record the load and displacement data during the indentation experiment, expanding the information that can be extracted from the test. This method eliminates the need to image the residual footprint to calculate the hardness; allows the determination of the plain strain modulus and makes possible to study other

properties such as viscosity and creep in viscoelastic materials. It has been applied primarily to nanoindentation where the imaging of the imprint is a complicated and time consuming task. Nevertheless, the application in macro and micro-indentation is also broad and the technology development is bringing more sophisticated commercial equipment that can perform the test at temperatures and environments different to those of room conditions.

The load displacement curve that can be plotted from the indentation data can exhibit different features depending on the material's behaviour, the indenter type and the test parameters such as the loading scheme.

Under Vickers indentation in elastic-plastic materials, there will be plastic and elastic deformation during the loading stage, and pure elastic recovery at unloading. The difference between the starting point of the loading section and the end point of the unloading reflects the depth of the permanent or plastic deformation caused by the indenter on the surface. The blunt or Hertzian indenter will cause only an elastic deformation in the same material, therefore, the resulting curve will look similar for loading and unloading if no fracture has taken place.

The indentation of a viscoelastic material will exhibit creep during a dwell time at a constant load. The displacement rate of the indenter while keeping a constant load will vary according to the material viscous behaviour at a given temperature.

It is worth mentioning that the conditions at which the test is conducted, such as loading/unloading rate, dwell time, and maximum load, influence the profile of the resulting curve, especially in viscoelastic materials. It is also necessary to correct the load displacement curve for factors such as machine compliance and indenter tip shape (generally referred as Tip Area Function or TAF) as will be discussed below.

The analysis of the data obtained by instrumented indentation is based on the equations of contact mechanics of solid bodies. The two systems that are of special interest for this purpose are the Hertzian contact (spherical indenter), and the sharp contact (conical or pyramidal indenter).

The Hertzian theory (equation 2.9) states that the radius of the circle of contact  $a$  between two solid bodies is determined by the load  $P$ , the radius  $R_1$  and  $R_2$  of the bodies, and the combined elastic constants:

$$a^3 = \frac{3 PR}{4 E_r} \quad 2.9$$

where  $E_r$  is the reduced modulus as described in equation 2.2,  $R$  is the combination of radius of both bodies with the form:

$$\frac{1}{R} = \frac{1}{R_i} + \frac{1}{R_s} \quad 2.10$$

In indentation experiments, the specimen is usually a flat surface, or a body of large radius in comparison to the area of contact that can be considered as flat for the analysis ( $R \rightarrow \infty$ ), therefore,  $R$  refers in indentation analysis to the radius of the indenter only.

Another important analysis is the deformation of the surface by the spherical indenter. Consider first a contact between the indenter and the surface without any applied load (Figure 2.12):

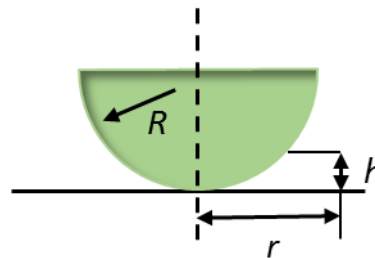


*Figure 2.12: Relation of an arbitrary point in the periphery of a spherical indenter and the radial distance  $r$  given in equation 2.12*

The distance  $h$  between an arbitrary point in the periphery of the indenter and the correspondent vertical point on the surface at a radial distance  $r$  from the symmetry axis will be:

$$h = \frac{r^2}{2R} \quad 2.11$$

When a load is applied, assuming an ideal rigid indenter,  $h$  will be given by:

$$h = \frac{1}{E_r} \frac{3}{2} \frac{P}{4a} \left( 2 - \frac{r^2}{a^2} \right) \quad r \leq a \quad 2.12$$

Rearranging the above equations and assuming  $r=0$ , the point of maximum penetration depth  $\delta$  for an ideal rigid indenter will be:

$$\delta^3 = \left( \frac{3}{4E_r} \right)^2 \frac{P^2}{R} \quad \text{and } \delta=h \quad 2.13$$

And by substituting equation 2.9 in 2.13, we obtain:

$$\delta = \frac{a^2}{R} \quad 2.14$$

Expressing equation 2.13 in terms of  $h$ , we obtain the equation that relates the load  $P$  with the penetration depth  $h$  which also considers the elastic constants of the specimen and the indenter:

$$P = \frac{4}{3} E_r R^{1/2} h^{3/2} \quad 2.15$$

Sharp or pyramidal indenters (Figure 2.13) are treated first as a conical indenter and the equivalence between both is given later in this section. The equations for a contact between this rigid conical indenter and an elastic half space were developed in the 1960s by Sneddon (1965). The relationship between the load  $P$  and the contact radius  $a$  is provided in equation 2.16.

$$P = \frac{\pi a}{2} E_r a \cot \alpha \quad 2.16$$

where  $\alpha$  is the indenter cone half angle. The displacement of the surface of the specimen and the indenter is given by:

$$h = \left( \frac{\pi}{2} - \frac{r}{a} \right) a \cot \alpha \quad r \leq a \quad 2.17$$

The same relationship expressed in terms of the penetration depth  $h$  is:

$$P = \frac{2}{\pi} E^* h^2 \tan \alpha \quad 2.18$$

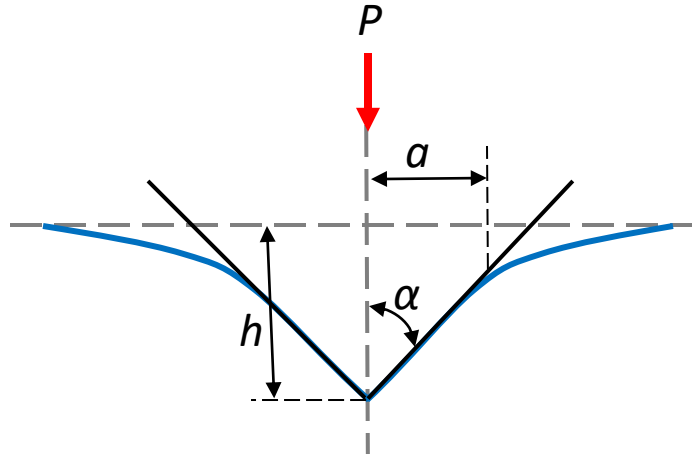


Figure 2.13: Relationship between load ( $P$ ) and contact radius ( $a$ ) in terms of penetration depth ( $h$ ) and indenter cone half angle ( $\alpha$ ).

The previous equation allows now the calculation of the contact stiffness, which is an important value in the analysis of data of instrumented indentation. Taking the derivative of  $P$  with respect to  $h$  of equation , the following relation is obtained:

$$\frac{dP}{dh} = 2 \left[ \frac{2}{\pi} E^* \tan \alpha \right] h \quad 2.19$$

And substituting again in first equation, we find:

$$P = \frac{1}{2} \frac{dP}{dh} h \quad 2.20$$

where  $\frac{dP}{dh}$  is the stiffness or the slope of the load-displacement curve for elastic loading. A further development of this equation leads to the expression that describes the relation of load, maximum displacement  $h_{max}$ , stiffness and contact depth  $h_c$  with the geometry of the indenter,

$$h_{max} = h_c + \left[ \frac{2(\pi - 2)}{\pi} \right] \frac{P}{dP / dh} \quad 2.21$$

The relationship of the indenter displacement  $h$  and the radius of the circle of contact  $a$  when  $r=0$  is given by:

$$h = \frac{\pi}{2} a \cot \alpha \quad (r = 0) \quad 2.22$$

Substituting the above equation in equation 2.19 we obtain:

$$\frac{dP}{dh} = 2E_r a \quad 2.23$$

And knowing that  $A = \pi a^2$ , it is possible to obtain now the reduced modulus  $E_r$  using the following expression:

$$E_r = \frac{1}{2} \frac{dP}{dh} \sqrt{\frac{\pi}{A}} \quad 2.24$$

This last relationship is applicable for all axisymmetric indenters such as a cone, a sphere and a cylindrical flat punch. The stiffness  $\frac{dP}{dh}$  is obtained experimentally from the load displacement curves; and the contact area  $A$  can be deduced from the geometry of the indenter and the depth of the circle of contact (contact depth)  $h_c$ .

As was mentioned earlier, pyramidal indenters are treated as an equivalent conical indenter, and the same contact area to depth ratio is maintained with the equivalent  $\alpha$  angle (Table 2.2). The relationships of area  $A$  with contact depth  $h_c$  for the Berkovich and Vickers indenters are given in equations 2.25 and 2.26, respectively.

Table 2.2: Equivalent cone angles for Berkovich and Vickers indenters

Indenter	Indenter half angle ( $\theta$ )	Equivalent cone half angle ( $\alpha$ )
Berkovich	65.27°	70.296°
Vickers	68°	70.3°

Berkovich Indenter,

$$A = 3\sqrt{3}h_c^2 \tan^2 \theta \quad 2.25$$

$$A = 24.49h_c^2$$

Vickers Indenter

$$A = 4h_c^2 \tan^2 \theta \quad 2.26$$

$$A = 24.504h_c^2$$

The hardness  $H$  can be obtained from the instrumented indentation (equation 2.27), in this case, the area ( $A_{max}$ ) to consider includes the elastic and plastic effects at maximum load  $P_{max}$ .

$$H = \frac{P_{max}}{A_{max}} \quad 2.27$$

The previous equation assumes a perfect indenter shape, however, as is not possible to have a perfect tip shape due to manufacturing of the indenter tip or wear, a function needs to be applied to take in account this deviation. This correction is called Tip Area Function (TAF) and is explained in detail in section 4.3.5.

## 2.7 Properties and surface contact of glass at high temperatures

### 2.7.1. The surface contact at high temperature in the industry

The surface damage of glass originated at high temperature has been investigated especially in glass container manufacturing. Rawson (1988) proposed that there are two mechanisms of surface damage of glass while in contact with other materials during manufacturing and before annealing, these are:

- Transfer of foreign materials to the glass surface, and;
- Adhesion to the contacting surface and the development of local stresses of high magnitude during contact.

Regarding the transfer of materials to the glass surface, there were some studies in the University of Sheffield in the mid 1970's (Puyane, 1976; Puyane and Rawson, 1979) where particles found in the surface of glass bottles were characterized. These particles were of irregular sizes and shapes and were firmly embedded into the surface. The particle size varied from 30 to 200  $\mu\text{m}$  and with the help of EPMA analysis it was found that their composition was rich in carbon and iron. It was inferred that the particles came from the contact with the forming mould commonly made of cast iron.

Further SEM analysis showed evidence of cracks around the embedded particles and it was believed that the cracks were generated during the cooling process due to the differences in thermal contraction of the particle and the glass.

Puyane (1976) carried out laboratory experimentation to measure the effect of the surface damage at high temperature on the glass strength. Glass discs were impacted at 600, 800 and 1000°C with particles of different size and materials. An indentation was done as well with a 3mm silica rod with a rounded tip. The biggest impact on the strength was found with the glass discs at 800°C. It was reported also that the strength decrease of the samples at 600°C was similar to that of samples damaged at room temperature. However, it is important to notice that the force of the particles against the surface was given only by the effect of gravity and particle mass; no additional pressure was exerted over the surface on this experiment.

One of the main conclusions was that the size and shape of the particles abrading the glass play an important role on the degradation of strength, with temperature being an important factor. At lower temperature particles cause mechanical damage, at higher temperatures, the particles embedded causing a different type of microcracking.

In regards of the adhesion of glass to the forming mould at processing temperatures, this problem will increase with forming temperature but, the material of the mould is important as well since, in the case of metals, adhesion will occur at lower temperatures if an oxide layer is present. For this reason, the container industry has utilised coatings for example nickel deposited electrolytically since it shows weaker adhesion and thus a higher temperature has to be reached before adhesion occurs (Coney 1978).

Other factors contributing to damaging the glass at high temperature are (Rawson, 1988):

- sharp corners in contact with the surface
- dirt on the interface between the glass and metal

- inadequate cushioning during the process causing excessive impact on the glass

Glass-metal contact at high temperatures has been analysed from different perspectives, for example the effect of abrading materials at different glass temperatures (Budd et al. 1980) and the effect of the abrading materials at different temperatures in comparison to the glass temperature (Bourne et al. 1984). In the first case, it was found that if the metal is coated with materials that can reduce friction, it will help to reduce the damage in the glass. In the latter case, if the abrading materials are at lower temperature than the glass, there will be a thermal gradient and hence a stress field thermally induced in the surface that, along with a further impact or indentation, will cause more severe damage on the glass surface. The damage to the glass is also increased with the hardness of the abrading materials. Silicon, steel and chromium are commonly present in the processing of glass and are very harmful because their hardness is higher than the glass at elevated temperatures. (Bourne et al. 1984).

### 2.7.2. The properties of glass at high temperature

*Vickers hardness and Young's modulus as a function of temperature.*

The hardness of glass or, its resistance to a permanent deformation under indentation, is the sum of the resistances to densification, shear flow and elastic deformation. The shear flow is related to the shear modulus, the bond strength factor and the elastic deformation, which is governed by the bulk modulus, as stated by Yamane and Mackenzie (1974) in the following equation:

$$Hv = 0.19(\alpha GB)^{1/2} \quad 2.28$$

where  $G$  is the shear modulus,  $B$  is the bulk modulus (both of which are related to the Young's modulus and Poisson ratio in isotropic materials) and  $\alpha$  is the average bond strength. Therefore, we can infer that if there is a decrease in the elastic modulus and in the bond strength, the hardness will decrease as well.

Studies by Spinner (1956), Shinkai et al. (1981) and Rouxel (2007), the last two on float glass, show a decrease of the elastic modulus with temperature (Figure 2.14). The curve starts with a slight decrease from room temperature up to the glass transition temperature  $T_g$ , and a steep decrease after this temperature.

The explanation of the decrease of the Young's modulus with temperature is given by the relation:

$$E = \frac{1}{r_o} \left( \frac{dF}{dr} \right)_{r=r_o} \quad 2.29$$

which states that the Young's modulus ( $E$ ) is inversely proportional to the distance between atoms ( $r_o$ ) (Makishima and Mackenzie, 1973). Therefore, a thermal expansion as a result of increased temperature, will increase the inter-atomic spacing ( $r_o$ ) and hence will reduce the Young's modulus. This is true for the majority of glasses, however, fused silica presents an anomalous behaviour in which the Young's modulus increases slightly with temperature (Spinner 1962, Brückner 1970). This behaviour is because the occurrence of a reversible structural rearrangement (Si-O-Si bonds rotation) resulting in a stiffer structure that superimposes on the weakening of the interatomic bonding due to temperature (Huang and Kieffer 2004).

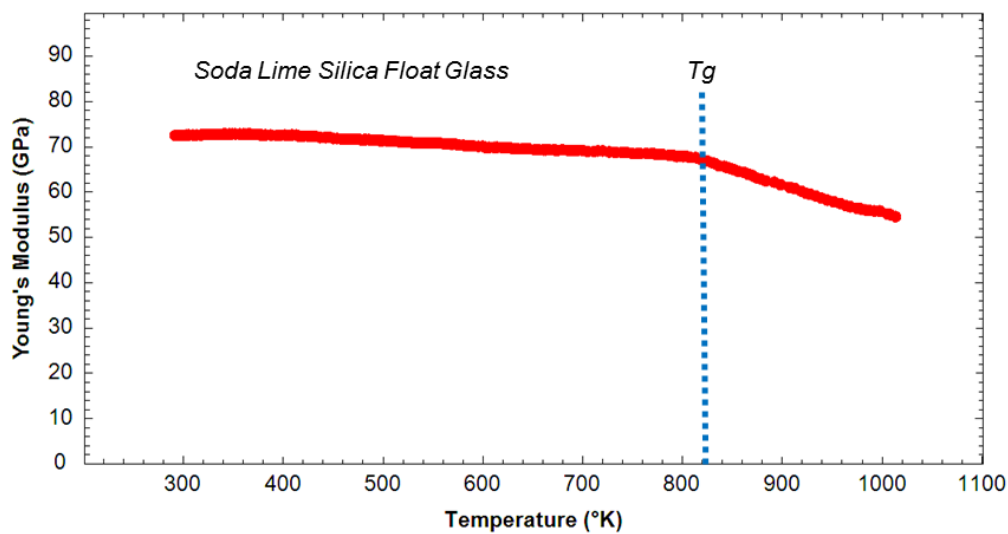


Figure 2.14: Young's Modulus of SLS float glass as a function of temperature measured with ultrasonic echography. (After Rouxel 2007)

One of the first studies of Vickers hardness on Soda Lime Silica glass at different temperatures was carried on by Westbrook (1960). He compared the hardness of some simple glasses including fused silica. The experiments were conducted in vacuum with loads ranging from 10 to 200 grams (0.098 to 1.962 N), a loading rate of 1mm/min and the results showed a continuous decrease of hardness with temperature starting from room temperature up to 250°C. Similar results were obtained by Michel et al (2004) for Soda Lime Silica glass in a temperature range of 20 to 400°C under normal air, with loads of 5 to 40N and a dwell time of 60s. The results of these two studies differ from those of Le Bourhis and Metayer (2000) or Watanabe et al. (2001) for example, where almost no change in hardness is noticed in the range of room temperature to 350°C. Michel *et al.* believe that the reason for these differences behaviour is because creep becomes dominant due to the high dwell time they applied.

Recent studies have increased understanding of the behaviour and resistance of the glass surface near the glass transition temperature (Kese et al. 2008, Le Bourhis and Rouxel 2003; Shang et al. 2006; and Wilantewicz and Varner 2008). Primarily Vickers indentation has been used for these studies. The hardness of the glass and the crack behaviour has been characterized over the temperature range room temperature to around 600°C. Hardness decreases with increasing temperature. Time and load become increasingly important as the glass reaches a viscoelastic state with lower contact times resulting in higher hardness. The variations in data reported by different publications on this matter (Figure 2.15), especially near and above  $T_g$ , arise because of the different test parameters used (Table 2.3), but they concur in the major role that the viscous behaviour plays in determining the magnitude of the indentation.

The results shown in Figure 2.15 indicate a small change in hardness from room temperature up to 200°C, after this temperature, there is a continuous decrease as a function of temperature and a more sharp decrease after the glass transition temperature of around 560°C for this type of glass. It can be notice a general agreement in the results from these different studies in the

range up to 400°C, but then after that temperature, the difference between the results is significant.

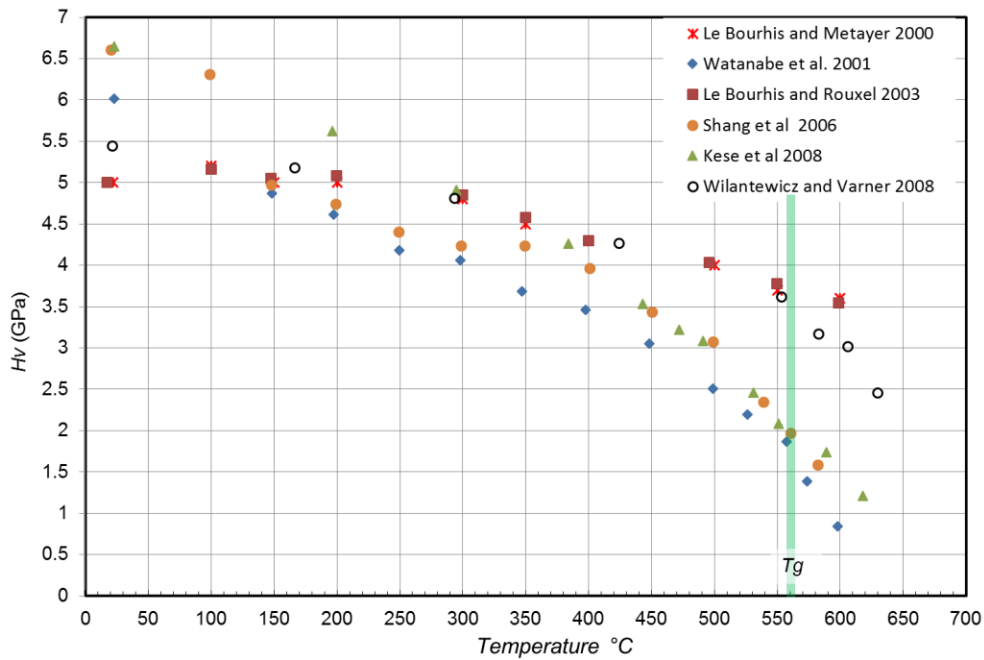


Figure 2.15: Studies of Hv as a function of temperature in the range of RT to near and above glass transition temperature for soda lime silica glass.

Table 2.3 Parameters used to obtain the experimental data shown in Figure 2.15.

Authors	Loading Rate (mm/min)	Dwell Time (sec)	Max. Load (N)	Hv@Tg (GPa)	Atmosphere	Float Side
Le Bourhis and Metayer 2000	10	30	4.9	3.7	Argon	Air
Watanabe et al 2001	N/S	15	0.49	1.65	Vacuum	N/S
Le Bourhis and Rouxel 2003	10	30	4.9	3.7	Argon	Air
Shang et al 2006	N/S	30	.196	2.0	Ambient	Tin
Kese et al 2008	0.1	0	49	1.7	Ambient	Air
Wilantewicz and Varner 2008	0.012	0	9.8	3.4	Ambient	Air

N/S: not specified by the author

It is not clear from table 2.3 how the test parameters influence the hardness value, and it is logical to think that a longer contact time during the

different stages of the experiment will translate into a lower hardness due to the viscoelastic behaviour of the material at the glass transition temperature. Nevertheless, it not possible to infer from the published reports, the relevance of each factor.

Figure 2.16 (Wilantewicz and Varner, 2008) represents the results of different indenter displacement rates against hardness for different temperatures. It can be noticed in this graph that the effect of the loading rate is meaningless at 22°C because the viscoelastic effect is not present, but results more relevant as the temperature increases.

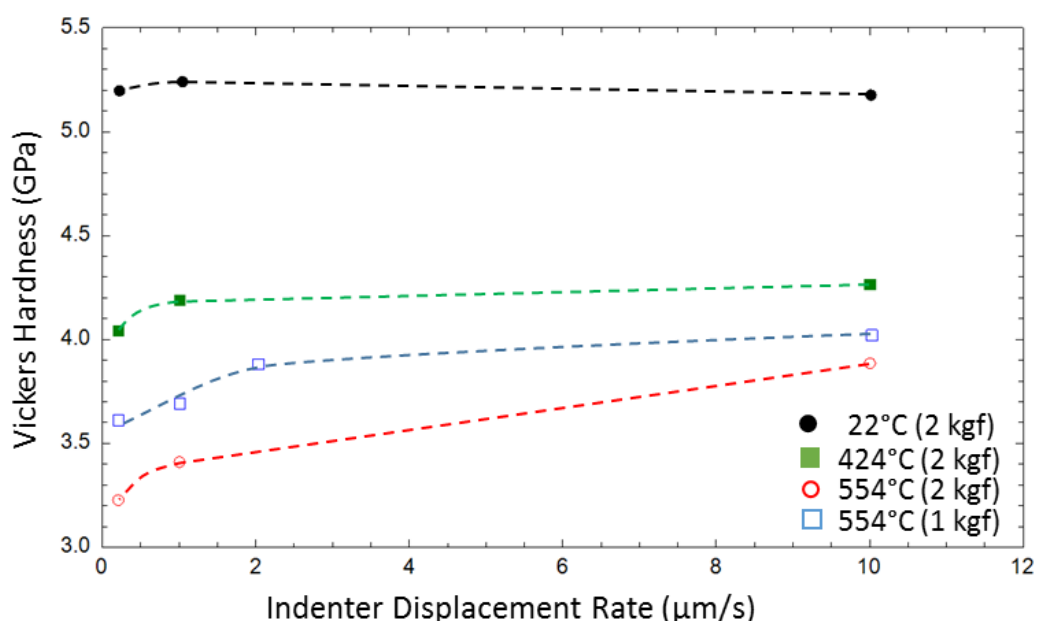


Figure 2.16: Vickers macroindentation hardness of float glass as a function of the indenter displacement at different temperatures (Wilantewicz and Varner 2008). The lines are only a visual guide.

Watanabe et al. (2001) studied the response of Vickers hardness in a vacuum and temperatures ranges between RT and  $T/T_g=1.1$  of fragile and strong (see below for a definition) glass-forming systems. They reported a gradual decrease in hardness in all cases with increasing temperature up to  $T/T_g<0.9$ . But, in the transition range, fragile glasses showed a steep decrease in the hardness whereas strong glasses still showed a gradual decrease until they reach almost  $T/T_g=1.1$  when the hardness decreased sharply. They concluded that the Vickers hardness at temperatures around  $T_g$  is also strongly influenced by the glass composition.

Strong and fragile glasses are defined in terms of their Arrhenius behaviour or, in other words, the variation of viscosity with temperature above  $T_g$  (Kurkjian and Prindle 1998). Strong glasses are those that keep a linear or near linear variation with temperature in the liquid region, as fused silica (see Figure 2.17). Fragile glasses for the contrary, exhibit a non-linear (non-Arrhenius) variation and are represented by a curve in the same figure.

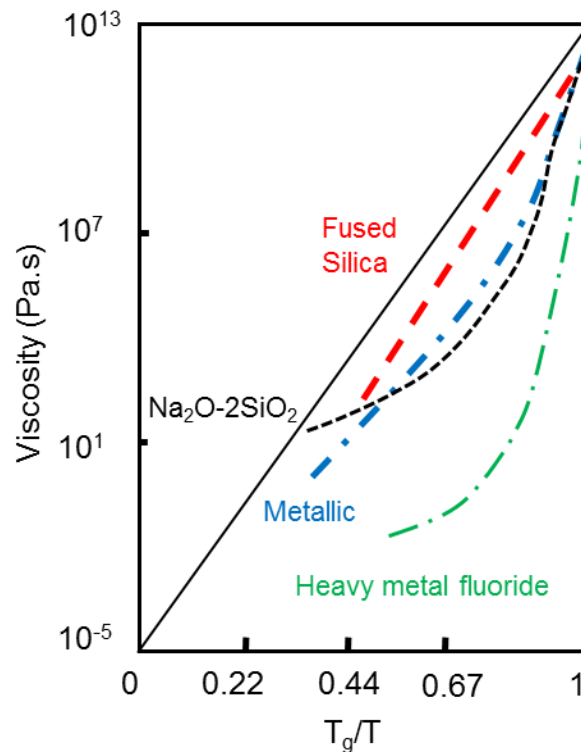


Figure 2.17: Variation of viscosity (log) with  $T_g/T$  for different glass systems. Fused Silica has a linear variation of viscosity with temperature hence is classified as strong. The other systems exhibit a non-linear variation and are called fragile (after Kurkjian and Prindle 1998).

There is also a phenomenon that occurs after indentation that might influence the results of the Vickers hardness. This is the shrinkage in the indentation footprint during the annealing and cooling of the sample after the test. Yoshida et al. (2001) have reported a reduction on the indentation diagonal's size of up to 10% depending on the load and the annealing time. This phenomenon is related to the relaxation of the densified material around the indentation during annealing.

*Cracking behaviour during Vickers indentation at high temperature.*

Relatively recent works that have measured the size of the median/radial cracks length generated by a Vickers indentation in SLS glass from room temperature to around  $T_g$  (Michel et al 2004, Kese et al 2008, Wilantewicz and Varner 2008) reveal a tendency of the crack length to increase with temperature until it reaches a temperature around 400°C, and then the crack length start to decrease again as it get closer to  $T_g$ .

Re-writing Equation 2.8, Equation 2.30 relates the crack length  $c$  of a Vickers indentation and the material properties for a constant indentation load  $P$  in ceramic and glasses (Anstis et al 1981):

$$c = \left[ 0.016 \frac{\left( \frac{E}{H} \right)^{1/2} P}{K_c} \right]^{2/3} \quad 2.30$$

The ratio of the Young's modulus with hardness  $E/H$  is recognized as the parameter that describes the indentation fracture driving force in brittle materials. And as can be inferred from equation 2.30, an increase of the  $E/H$  ratio should increase crack length  $c$ . As discussed previously, both  $E$  and  $H$  decrease with temperature in SLS glasses, but despite this, the  $E/H$  ratio tends to increase in the temperature range below 400°C because the hardness decreases faster. The behaviour of the  $E/H$  ratio with temperature is described by Kese et al (2008) in Figure 2.18 where the Young's modulus values with temperature were obtained by means of an ultrasonic method and the hardness measured from their experiments.

Above  $T_g$  (560°C for Soda Lime Silica glass), a decrease in the crack length is expected since viscous flow will predominate at and above this temperature which will relieve the crack tip stress. Moreover, the disappearance of the crack in indentations made above  $T_g$  for SLS glass has been reported by most of the related works cited previously. In practice, inspection of the high temperature indentation site can reveal only surface cracks such as the radial crack system and possible lateral cracks. Median

vents nucleating under the indenter might be harder to detect because these are subsurface.

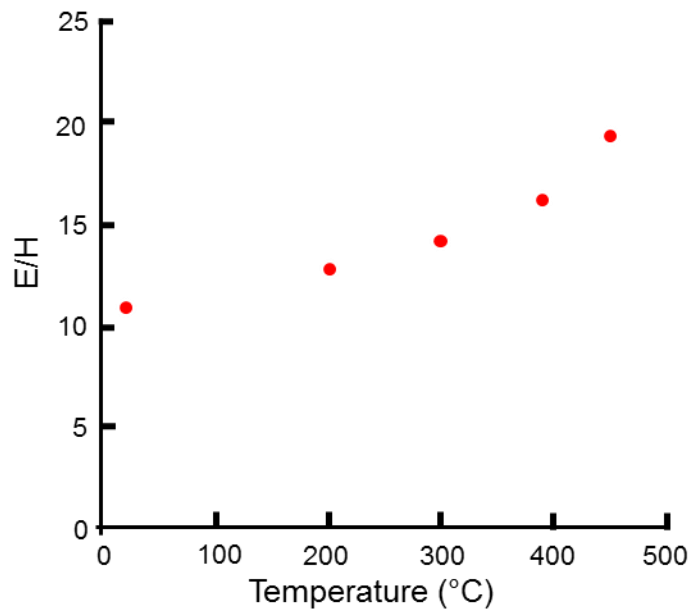


Figure 2.18: Modulus to Hardness ratio  $E/H$  as a function of temperature for SLS float glass. (Kese et al 2008)

#### *Hertzian indentation at high temperature*

Very few published papers are available regarding the Hertzian indentation at high temperature in soda lime silica glass. Beek and Lawn (1972) published the development of a device for conducting Hertzian indentation at elevated temperatures in controlled atmospheres although in their report, glass was tested at maximum 100°C with three different water-vapour pressures and reported the critical load to cone fracture under those conditions. A more recent publication is the work of Bernard et al. (2010) where they studied the indentation creep of Soda Lime Silica glass between 540 and 640°C using four types of indenters, including a half sphere of 1.5 mm. diameter made of sapphire. They designed and built a stand-alone device to carry out instrumented micro-indentations at temperatures up to 1100°C with the different indenters that allowed them to investigate the relation of viscosity with temperature in glass. The main advantage of this method was the small volumes required for the experiment and the easy preparation of the specimens.

As described previously, an important parameter for the Hertzian testing is the detection of the crack initiation during the application of the load, since this parameter is used to calculate the toughness. However, for indentation testing at high temperatures, it is difficult to use common piezoelectric sensors in contact with the glass to detect the acoustic emission of the crack inside the heating chamber, since most of them are designed to withstand a maximum temperature of 200°C. Some special sensors are rated for use up to 550°C but their special characteristics makes them expensive and difficult to fit in laboratory equipment because of their size. Some alternative solutions for this problem have been tested and reported by specialists such as Berndt (1989) where they have used waveguides to transmit the signal from the sample in the hot environment to a sensor located in a place at room temperature. These waveguides are metallic wires attached to the sample with high temperature resistant couplers and connected to the sensor at the cool end. The loss of sensitivity because of the use of the waveguides has been also measured, and it is reported for example, for lengths of 5 meters, there is only about 2 dB loss. (Zakharov et al. 2010).

### **3. Hydration and mechanical properties**

#### **3.1 Introduction**

In this chapter, the evolution of the hardness and the modulus of the SLS float glass in the near surface is investigated in terms of exposure to weathering at 40°C and 95% relative humidity (r.h.) and by means of nanoindentation. It is important to understand how the mechanical properties of the tin and air sides of the float glass change due to the effect of the water vapour in the atmosphere since these will determine the response to contact in service. Previous studies have been published with exposure at 80°C and 95% r.h. (Hayashi et al. 2002), however these conditions are very different from likely in-service conditions. This study therefore has used conditions which although are still relative aggressive, are not far from what could be seen in extreme in-service and storage environment, and are significantly closer to a wider range of practical conditions.

The resistance to fracture of both the tin and the air sides as a function of exposure time to accelerated weather conditions was also studied in this work. The study was conducted using Hertzian indentation. This type of indentation generates an elastic deformation and a tensile stress field in the contact area around the indenter, such stress field increases as the applied load increases and promotes the crack growth of a flaw of critical size just outside the contact area of the indenter (see section 2.6.1). There will be a minimum load at which the flaws will propagate into a ring or cone crack. This crack propagation was detected using an acoustic emission system and therefore, the load at which this happens (minimum load) was obtained.

## 3.2 Experimental procedure

### 3.2.1. Preparation of hydrated samples

2 mm, green thermo-absorbent, float glass samples were obtained directly from Vitro Glass, Mexico. The primary usage of this glass is in the manufacturing of automotive laminated glazing. The glass was cut into 15x15 cm specimens from larger slabs taken from the warehouse. It was stated by the manufacturer that the glass was from recent production.

The float side of each specimen was identified using a short wave, 180-280 nm, UV lamp (Ultra-violet Products Ltd, Cambridge UK); under UV light the tin side is fluorescent and reflects a “milky” white image. In order to keep the tin side and air side identified for the rest of the testing process, a small section was removed by grinding one of the corners of the specimens on the tin side. Smaller specimens of 2x2 cm used for nanoindentation testing and SEM/EDX were identified in the same way.

The approximate composition of the samples received was measured by Energy Dispersive X-ray (EDX) spectroscopy on a scanning electron microscope Phillips PSEM 500. The specimen was prepared previously by mounting it on a sample holder suitable for this microscope and applying a carbon coating. The specimen was measured and the composition obtained for the air side was (weight %) 73% SiO<sub>2</sub>, 1.4% Al<sub>2</sub>O<sub>3</sub>, 8% CaO, 4.1% MgO, 12% Na<sub>2</sub>O; 0.1% K<sub>2</sub>O; 0.38% Fe<sub>2</sub>O<sub>3</sub> and 0.2% SO<sub>3</sub> which was in agreement with the composition range provided by the manufacturer. Similarly, the tin side was measured and the composition obtained was (weight %) 71.4% SiO<sub>2</sub>, 1.05% Al<sub>2</sub>O<sub>3</sub>, 8.1% CaO, 4.0% MgO, 13.21% Na<sub>2</sub>O; 0.25% K<sub>2</sub>O; 0.38% Fe<sub>2</sub>O<sub>3</sub>, 0.15% SO<sub>3</sub> and 1.3% SnO<sub>2</sub>.

EDX analysis indicated that in the glass studied here the tin side contained ~1.3wt% tin as SnO<sub>2</sub>. This is a little lower than the values reported by Verità et al. (1995) who found an average tin content over a 40 µm depth of up to 3wt% SnO<sub>2</sub> as discussed in section 2.4. It should also be noted that Verità et al observed a much greater tin concentration of up to 10wt% within 20 nm of the tin side glass surface i.e. a significant tin gradient in the near surface

region can be expected. In comparison the current EDX result will reflect an average value over  $\sim 1 \mu\text{m}$  depth.

All the samples were cleaned with isopropanol on both sides and dried with dry compressed air. The glass samples were accommodated inside a weathering chamber (Environmental Chamber Mod. MTH-2400, Sanyo Electric Biomedical Co, LTD, Japan) using a specially fabricated stand (Figure 3.1) designed to hold the samples vertically and supported only from one of the edges allowing around 20 mm separation between samples.

The samples inside the weathering chamber were continually exposed to 95% relative humidity at  $40^\circ\text{C}$  for periods of 3, 7, 12, 15, 19 and 49 days.



*Figure 3.1: Samples inside the weathering chamber*

### **3.2.2. Nanoindentation**

After each weathering period, one sample for testing the tin side and one for testing the air side was taken from the chamber and the near surface mechanical properties measured by nanoindentation using a Hysitron Triboscope® (Hysitron Inc., Minneapolis, MN, USA) mounted on a vibration resistant table and equipped with a noise and temperature insulation hood. A Berkovich diamond (Young's modulus 1141 GPa and Poisson's ratio 0.07) tip was used for the nanoindentation.

Before nanoindentation of the samples, calibration was carried out on a fused silica sample which has a Young's modulus of 72 GPa and a Poisson's ratio of 0.17 which gives a reduced modulus for the combined tip and sample of 69.6 GPa. For calibration 7 automated arrays of  $8 \times 8$  indentations with 4  $\mu\text{m}$  separation between indents were made on the fused silica sample. The loading scheme was 5 s up-load, 5 s dwell and 5 s download with 60 s between indentations. The load range used for the calibration was from 20 to 10,000  $\mu\text{N}$  with more emphasis being paid to obtaining data in 0 to 100 nm indentation depth range. The basic analysis followed the method of Oliver and Pharr (1992) but the calibration function was obtained as an equivalent radius,  $r_c$ , following the protocol proposed by Tadjiev et al (2010) which was designed for shallow depth calibration. Figure 3.2 shows the variation of  $r_c$  of the indenter as a function of the contact depth  $h_c$ .

For the tip used in this work the following equivalent radius function was found:

$$\begin{aligned} r_c &= 1.9902h_c + 14.9636h_c^{1/2} + 49.9165 & h_c < 62.1 \text{ nm} & \quad 3.1 \\ r_c &= 2.666h_c + 125.83 & h_c \geq 62.1 \text{ nm} & \end{aligned}$$

The corresponding tip area function,  $A$ , can then be obtained using

$$A = \pi(r_c^2) \quad 3.2$$

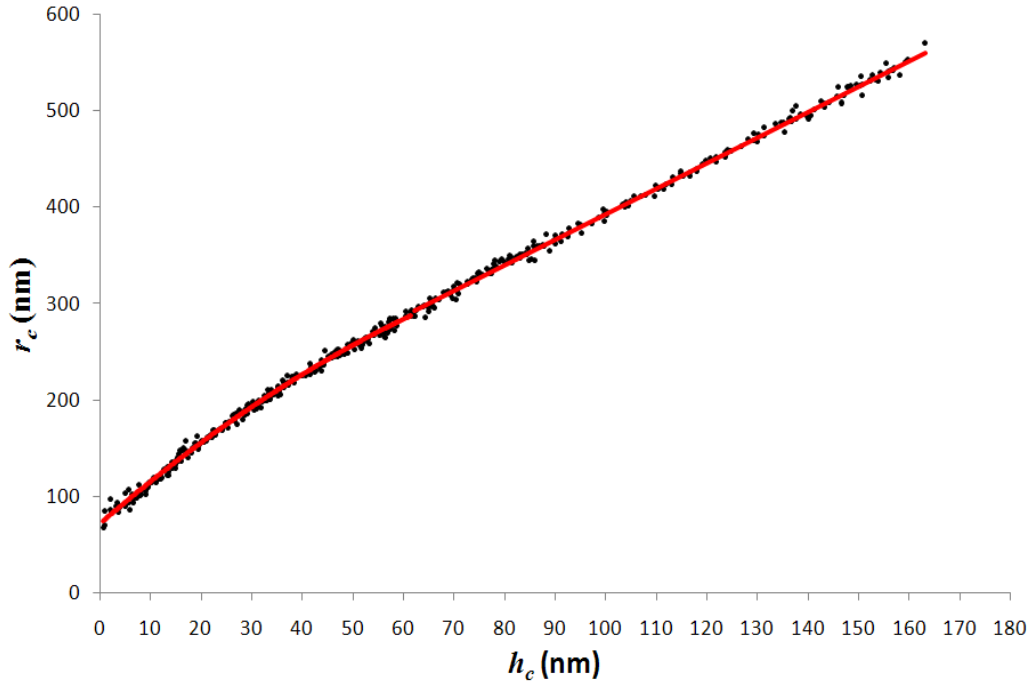


Figure 3.2: Variation of the contact radius (indenter) as a function of the contact depth

Nanoindentation of the glass samples was performed using two automated arrays of  $9 \times 9$  indents with  $3.5 \mu\text{m}$  between indentations in both the  $x$  and  $y$  directions. The loading scheme was again 5 s load, 5 s dwell and 5 s unload. For the testing the loading range was usually between 20 and 5,000  $\mu\text{N}$ . The glass samples were extracted from the weathering chamber and subjected to a stream of dry compressed air to remove any loose debris. The samples were then immediately tested in the nanoindenter. In addition to the weathered samples both sides of “as received” samples were also tested. For all samples prior to nanoindentation the nanoindentation site was scanned using the Dimension 3100 (Veeco Digital Instruments, Santa Barbara CA, USA) atomic force microscope mounted on the nanoindenter to ensure that the test area was uniform. The unloading stiffness,  $S$ , determined by the Oliver and Pharr method and was used to calculate the reduced modulus of the samples using

$$E_r = \frac{S}{2.1r_c} \quad 3.1$$

The nanoindentation hardness was calculated using

$$H = \frac{P_{\max}}{A_{\max}} \quad 3.2$$

where  $P_{\max}$  is the maximum load during an indentation and  $A_{\max}$  is the corresponding tip (contact) area.

### 3.2.3. SEM/EDX analysis

The glass surface of samples “as received” and after 12 days exposure to weathering were also studied using a scanning electron microscope (JSM 6400, JEOL Ltd. Tokyo, Japan) equipped with an X-ray detector (Oxford Instruments, Oxfordshire, UK). X-ray mapping of various regions using a beam energy of 20 keV, a probe current of  $10^{-9}$  A. The specimens were mounted on a suitable support and carbon coated to avoid charging.

### 3.2.4. Hertzian indentation

The Hertzian indentation test used WC-6%Co sphere with a diameter of 6.35mm (Euro Products Ltd, Stourbridge, UK) mounted on a universal testing machine (Hounsfield Test Equipment Ltd, UK, Mod. H100KS). The crosshead speed was 0.1 mm/min and the maximum load applied was 1500 N with a hold time of 20 s. The test was stopped manually after a crack initiation signal was received. At least 30 samples were tested for each surface condition and for both tin and air sides.

Crack initiation was detected using an acoustic emission system (Micro 30, Physical Acoustics Ltd, Cambridge, UK) with the piezoelectric sensor installed in the indenter and adjusted to a threshold of 45 dB which experimentally was found to be sufficient to distinguish the signal from the noise associated with the machine. All the samples were examined in an optical microscope after the test to verify the existence of the ring or cone crack.

The critical load at which the crack was initiated was detected monitoring the signals from the load cell and from the acoustic emission system on the same computer screen using software and hardware supplied by the AE

system manufacturer (USB Node and AEdwin, Physical Acoustics Ltd. Cambridge, UK) in order to obtain a precise indication of the load at which the crack propagated.

### **3.3 Results**

#### **3.3.1. Nanoindentation and SEM/EDX results**

Figure 3.3 a) and b) show the evolution of the nanoindentation hardness of the air and tin sides respectively. Figure 3.4 a) and b) similarly show the evolution of the reduced moduli of the air and tin sides respectively. It is clear that the nanoindentation hardness and near surface moduli of the air side are greatly reduced as the surface undergoes accelerated weathering whereas there is relatively little change in the properties of the tin side.

Both Figure 3.3 a) and b) indicate that within the first 10 nm the nanoindentation hardness of both tin and air sides is reduced even on the as-received samples. Although it is possible that this is fundamentally a calibration issue it is notable that with increasing hydration of the air side the nanoindentation hardness decreases towards the values seen at the very lowest depths on the as-received samples.

Air side samples with longer exposure times (15, 19 and 49 days) exhibited a formation of a hydration layer with a thickness greater than the maximum indentation depth obtainable on the nanoindenter. Therefore it is assumed that the hydrated layer was more than 250 nm deep for these longer exposure times.

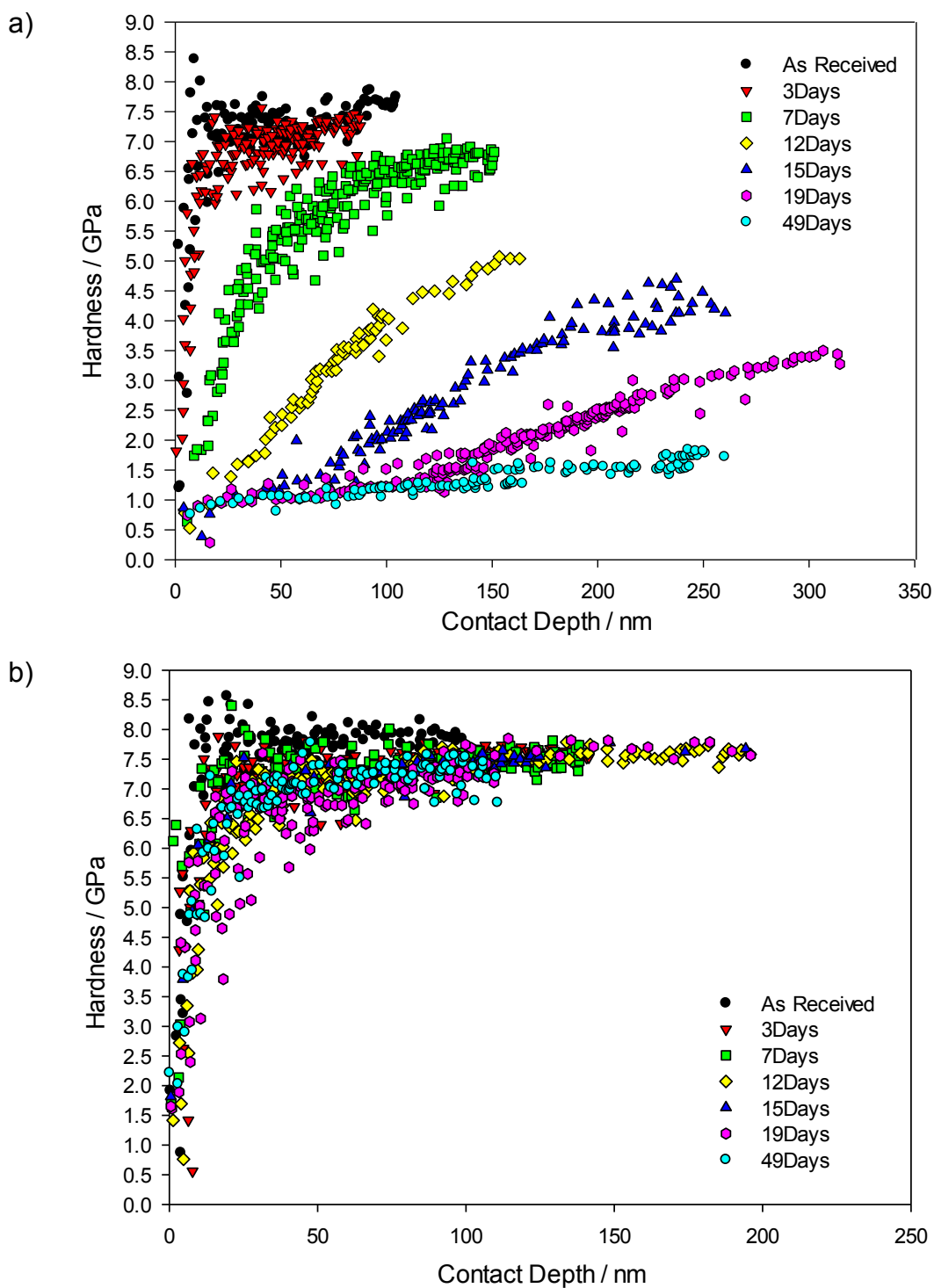


Figure 3.3: Evolution of nanoindentation hardness of glass exposed to different periods of accelerated weathering conditions (95% relative humidity at 40°C): a) air side and b) tin side of Soda Lime Silica float glass.

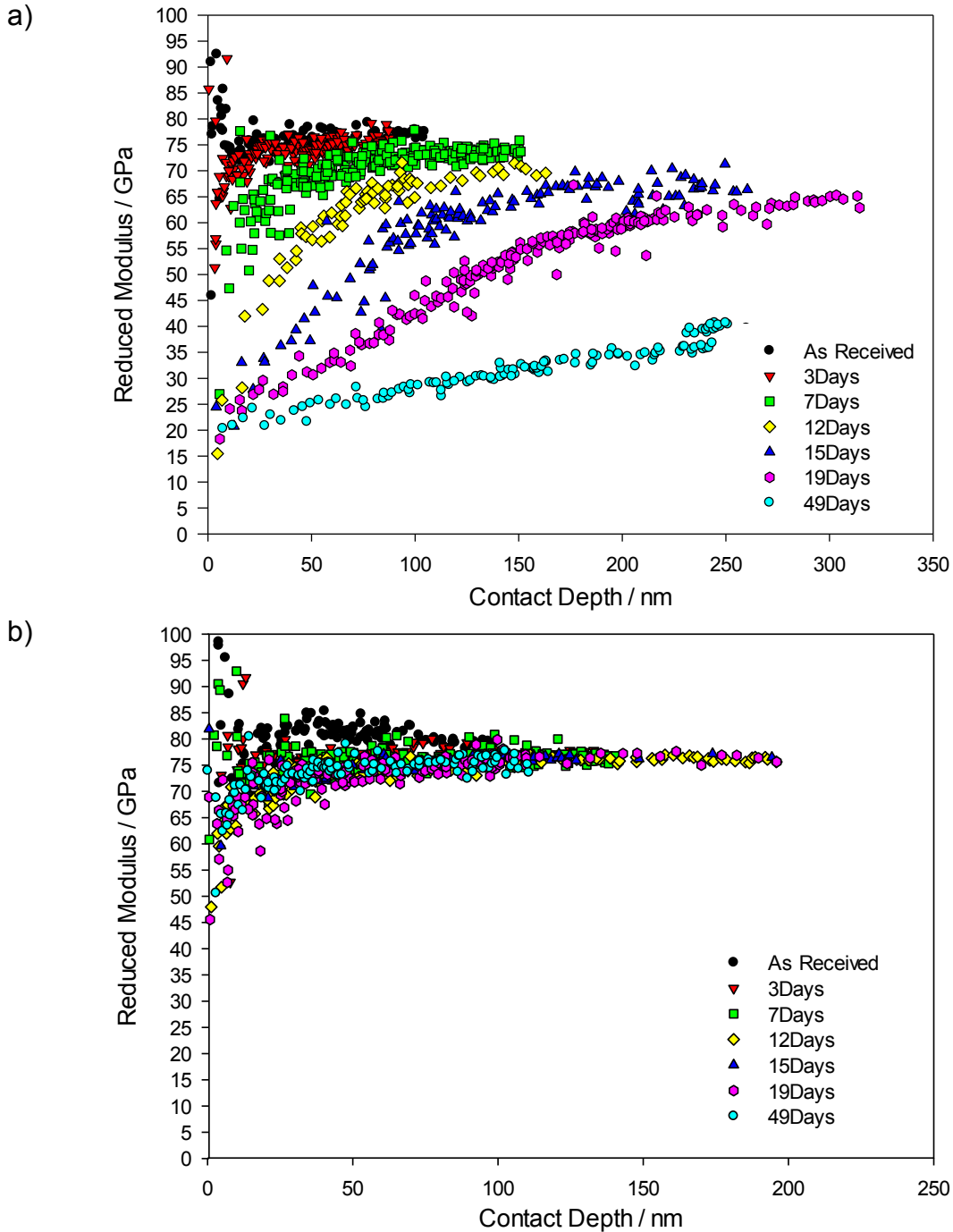
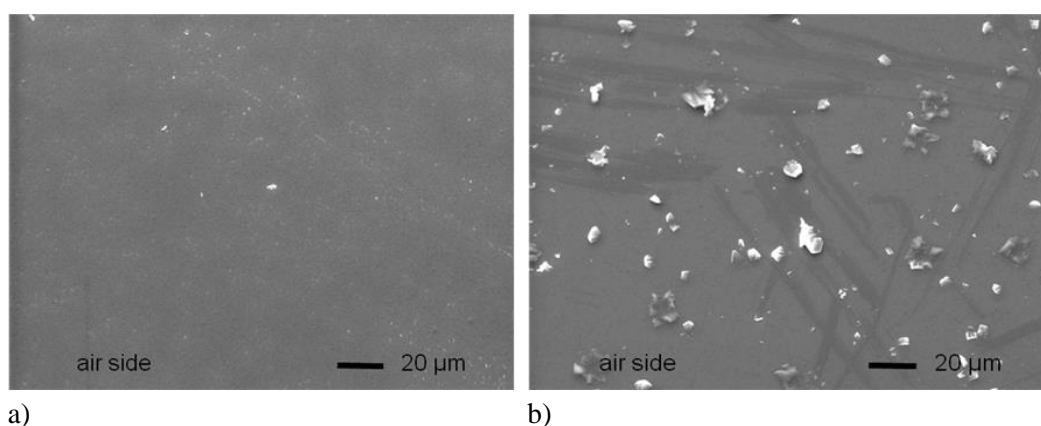


Figure 3.4: Evolution of the reduced modulus of glass exposed to different periods of accelerated weathering conditions (95% relative humidity at 40°C): a) air side and b) tin side of Soda Lime Silica float glass.

Visual inspection of the samples after weathering, especially those subjected to longer exposure times revealed a whitish alteration layer formed on the surface. It was decided only to dry the surface with dry compressed air before indentation, rather than undertake any more active cleaning process, to enable evaluation of the “as tested” surface condition. For this reason,

although an effort was made to perform the indentations in selected zones with uniform roughness using the AFM, some of the data exhibits increased noise which is attributable to indentations made over this rough layer.

SEM imaging before and after weathering shows the formation of alteration products on the air side (Figure 3.5) whereas the tin side (Figure 3.6) is apparently almost unaffected, after the same period of exposure to accelerated conditions.



*Figure 3.5: Secondary electron images of air side surface of float glass before (a) and after (b) exposure to 12 days of accelerated weathering at 95% relative humidity at 40°C*

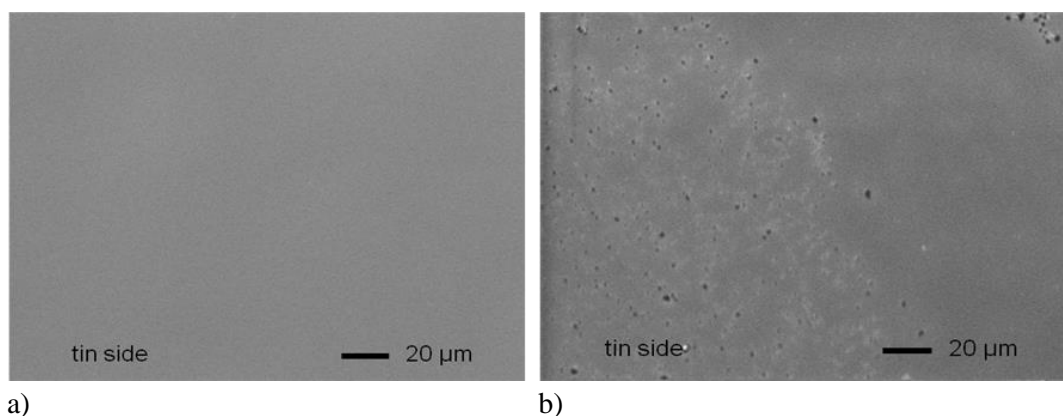
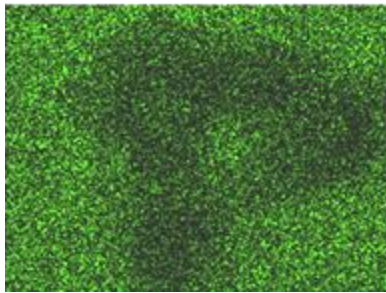
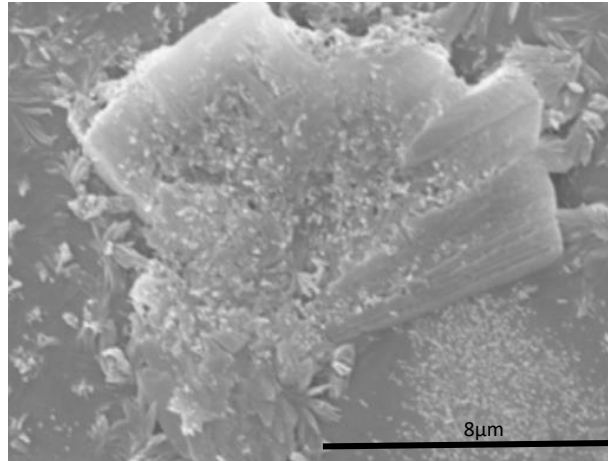


*Figure 3.6: Images of tin side surface of float glass before (a) and after (b) exposure to 12 days of accelerated weathering at 95% relative humidity at 40°C*

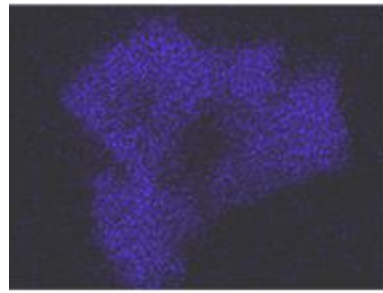
X-Ray mapping (Figure 3.7a and b) of the air side surface exposed to 12 days weathering was used to obtain qualitative information on the gross variation in composition of the features on the surface. The mapping shows

that the white layer on the surface is comprised of crystals that contain mainly calcium (Figure 3.7a or sodium Figure 3.7b).

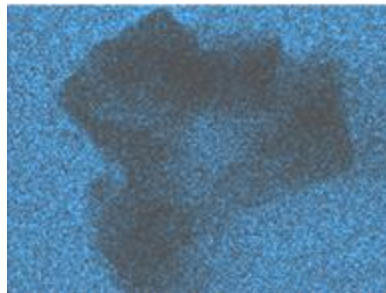
a)



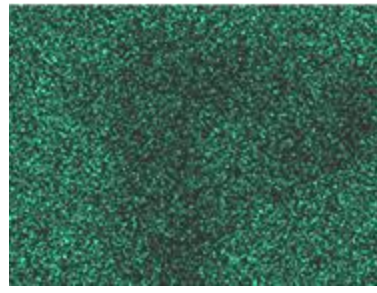
Na



Ca



Si



Mg

b)

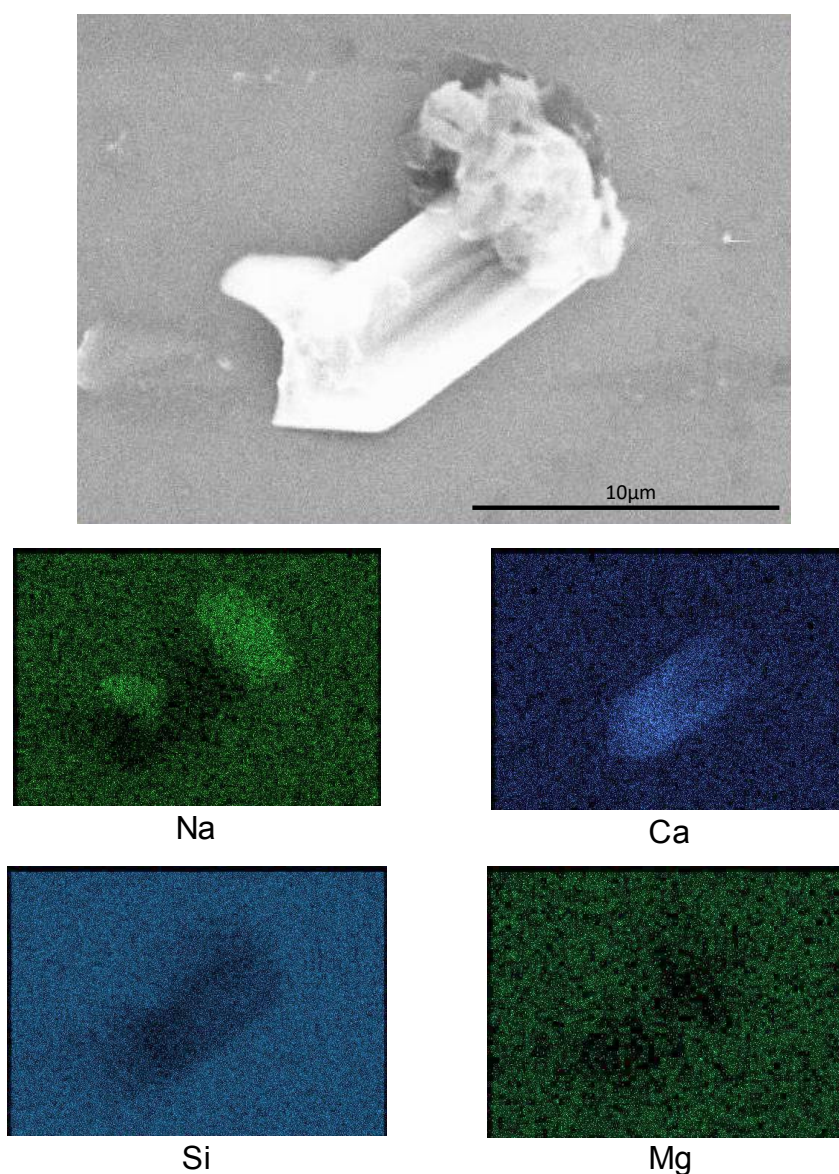


Figure 3.7: X-ray dot maps of a) calcium rich and b) calcium and sodium rich features on the air-side of samples exposed to 12 days of weathering at 95% relative humidity at 40°C

Overall these results demonstrate that the tin side is much more resistant to surface hydration than the air side, which is presumably due to the presence of tin in the surface. Bent *et al.*(1998) and Ziemath *et al.*(2005), in studies on SnO<sub>2</sub> doped glasses, present evidence that SnO<sub>2</sub> acts as a network former in the glass structure, thereby reducing the number of non-bridging oxygens. Although this might be expected to increase the diffusion rate of more mobile ions Ziemath *et al.* suggest that the high field strength of Sn<sup>4+</sup> leads to a more compact structure there by reducing the mobility of the

alkalis and thereby the rate of diffusion. In addition the tin side can be expected to be depleted in sodium ions to at least 100 nm depth (Verità et al 1995). The presence of an already sodium depleted layer may delay interdiffusion of sodium and hydronium ions which will delay the formation of high pH alkali rich droplets on the surface that can lead to the formation of a gel layer by network hydration.

### 3.3.2. Hertzian indentation results

The critical or minimal load required to propagate pre-existing surface flaws in the surface by the Hertzian indentation test was influenced by the time of exposure to weathering as shown in Figure 3.8. The data was better fitted by a Weibull distribution from which the mean was calculated using:

$$mean = \gamma + \eta \cdot \Gamma\left(\frac{1}{\beta} + 1\right) \quad 3.3$$

where  $\gamma$ ,  $\eta$  and  $\beta$  are the location, scale and shape parameters of the distribution and  $\Gamma$  is the Gamma function (NIST/Sematech 2012).

Lower loads were required to propagate the surface flaws into ring or cone cracks as the weathering time was increased. It is currently unclear whether this is due to static fatigue involving absorbed water; or to a change in the near surface mechanical properties (e.g. hardness and modulus) as described in the previous section.

The water in the environment will react with the strained bonds at the crack tips breaking the Si-O-Si bonds (Wiedehorn 1967 and Michalske and Freiman 1983) which ultimately provide the resistance to fracture.

Another feature of the results in Figure 3.8 is the difference in the critical load required to propagate a crack between the air and tin sides. This difference is attributed to the increased flaw density of the tin side surface because it is the surface in contact with the rollers during the manufacturing process of the float glass. This larger density increases the probability of finding a crack inside the tensile stress field of the indentation with enough size to satisfy the Griffith criterion of fracture (Griffith 1921).

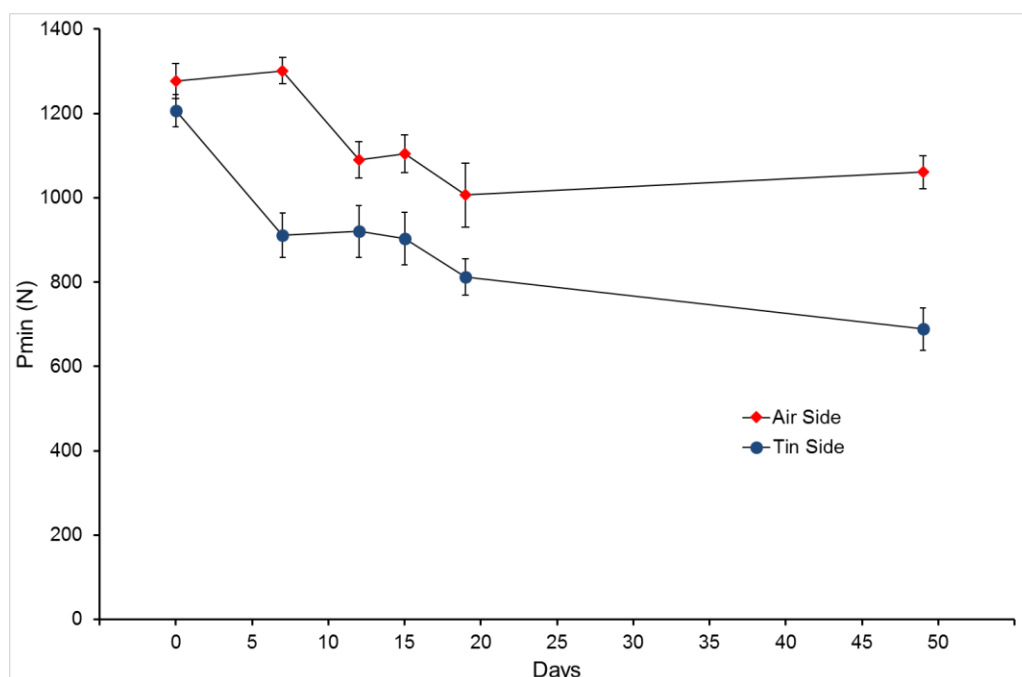


*Figure 3.8: Minimum load required to propagate pre-existing surface cracks on tin and air surfaces as a function of exposure to weathering. Error bars represent +/- 1 standard error from the mean.*

### 3.4 Discussion

The exposure of SLS float glass to weathering causes a change in the mechanical properties of the glass surface, but the extent of this change is different on the air side and in the tin side. The chemical difference that exists in both surfaces of this type of glass is inherent to the manufacturing process. On the air side, with longer exposures periods to weathering, the surface layer affected by the ion exchange of the alkalis of the glass with the hydronium of the environment grows rapidly, leading to a degradation of the hardness and the near surface elastic modulus as well. The tin side has been found to be more resistant to the effect of the weathering and to retain its optical and mechanical properties for longer.

The reduced modulus and nanoindentation hardness behaviour of the air side when exposed to the different weathering periods can be compared to

the S-shape profiles arising from the interdiffusional ion exchange of alkali ions and hydronium ions (see Figure 2.7). However this does not prove that the observed variation in properties arises from a continuous variation in sodium/hydronium concentrations as essentially similar modulus profiles are predicted by consideration of a 2 layer system (Perriot et al 2004). Thus the current data confirms that the hydrated layer has lower reduced modulus and nanoindentation hardness values than the bulk glass but it cannot be determined whether there is a gradual variation of these properties through the layer or not.

Previous work (Tadjiev et al 2010) has shown that the hydration layer developed by immersion in water has a lower density than the bulk glass. Although the layer in this study was formed by a weathering rather than an immersion process, reduced density would be consistent with the reduced hardness and Young's modulus seen on hydration in this work. It can be considered therefore that the hydration process in water and under the accelerated weathering conditions used in this work can lead to a similar effect on the mechanical properties of the surface.

In the current study the weathering was carried out using an environmental chamber in the laboratory, only calcium and sodium carbonates were found on the surface of the air side. However, as discussed in the literature survey, sulphates can be also found if the glass is exposed to weathering in an urban environment, where contaminants may exist.

The ion exchange and formation of crystals in the surface of the float glass occurring primarily on the air side represent a problem for some industrial applications, as is the case of the coating application processes and for the performance of the coating itself (Meszaros et al. 2013). Functional coatings are applied to the glass to improve the thermal and optical performance. As a standard practice, sacrificial barriers of  $\text{SiO}_2$  or  $\text{Al}_2\text{O}_3$  are applied in several layers between the functional coatings and the substrate (glass) to inhibit the ion exchange of the sodium and calcium of the glass with the water vapour of the environment through the coating. There are coatings that can be applied in-line with the float furnace such as in the Chemical Vapour deposition

(CVD) technique. In this case, the naturally coated surface is the air side, because it is facing up in the CVD chamber, which is pristine and the corrosion does not exist yet. But there are other coating processes that are applied off-line (i.e. sputtering). In the latter, the glass is stored sometimes for days before the application of the coating and, in most cases, the surface requires a mechanical or chemical cleaning to remove the products of the corrosion if this is applied on the air side. Although the tin side would require less cleaning, it has been suggested that the higher density of silanol groups (SiOH) on the air side would promote a better adhesion of the coatings to the surface, on the other hand, the tin side is affected by the presence of tin which reduces the formation ability of OH groups (Takeda et al 1999).

In the automotive industry it is also important that the glass maintains its excellent optical properties during its life in service. The derived effects of the ion exchange of both sides of float glass can have implications in the glass ability to display vehicle information. Nowadays the use of the Head-up display technology in the vehicles is increasing. With these systems, information is displayed on the windscreen section in front of the driver in order to increase the safety of the driving.

The changes in the near surface mechanical properties are also expected to adversely affect the long term mechanical performance of weathered glass. The experiments of hertzian indentation with glass exposed to different periods of weathering carried out in this work (section 3.3.2) showed a better resistance to fracture of the air side with this type of contact. The minimum load required to start a cone crack on both sides decreased with longer exposure times of the specimens to weathering, and the difference between both sides was maintained. This difference of the load at which the cone crack started between both sides is attributed mainly to the higher density of microcracks in the surface of the tin side because of the natural contact of this surface with the annealing furnace rollers right after the glass ribbon exits the float chamber as depicted in Figures 2.1 and 2.2. Therefore, the probability of starting a cone crack is higher on this surface. This characteristic seems to prevail as the main factor in the fracture resistance of

the surface, even over the changes occurring in both surfaces with weathering.

As reviewed broadly by Freiman et al (2009), water in the environment enhances subcritical crack growth. But on the other hand, it has been suggested that leached sodium in combination with a high concentration of hydronium ions (weathered glass in high humidity environment) build-up compressive stresses in the surface that increase the wear resistance of the same (Bradley et al 2013).

The resistance to fracture of both surfaces has been studied using different testing techniques and primarily on pristine surfaces. Flexural tests carried out by Gulati et al (2000) and Krohn et al (2002) indicate that the strength of the air side is superior, while other studies indicate an improved resistance of the tin side under similar tests (Wereszczak et al 2006). In Hertzian indentation tests, some other papers indicate that there is no difference in the force required to initiate the ring crack between both surfaces (Muller and Green 2010). However, there seem to be other factors influencing the measurement of the strength of the surfaces of float glass. Tummala and Foster (1975) found that the response of the surface under a dynamic 3-point bending test was reversed by changing the loading rate of the experiment. At lower loading rates, the tin side was stronger than the air side and vice versa, probably because of the better resistance to stress corrosion of the tin side according to the authors.

On surfaces exposed to weathering, which would be the case of the glass after a period in service, the literature is rather limited and contradictory information is found. Experiments with sharp indenters in SLS glass by Varner et al (2007) showed a surface more prone to cracking in aged glass, but in a report by Hayashi et al (2002), it was found that the frequency of crack formation evaluated with Vickers indentation, decreased in the air side with exposure time to weathering, due principally to the decline of hardness according to the author, while the strength on the tin side remained unaffected under the same conditions.

It is clear that there are differences in the corrosion resistance between both sides of the float glass, but the resistance to fracture of the air and the tin side in the long term is less evident. The response of each side would depend on the characteristics of the contact, the surface stresses (Varner et al 1980), the condition of the surface and the degree of corrosion of the same.

## **4. Apparatus for high temperature indentation**

An instrumented apparatus was designed and built by the researcher as part of this project to study the mechanical properties of glass at elevated temperature. This apparatus is integrated into a universal testing machine and is capable of making micro and macro-indentations using either pyramidal indenters (sharp) or Hertzian type indenters (blunt).

This device can monitor and register the load-displacement curves of the micro-indentation test as well as indenter and specimen temperatures. Parameters such as dwell time, temperature, loading and unloading speed can be changed within certain limits determined by the testing machine used enabling experimentation with different sets of conditions.

Micro and macro-indentation of materials at elevated temperatures has been studied using adapted universal testing machines as in our case (Michel et al. 2004, Watanabe et al. 2004 and Shang et al. 2006) or with specially fabricated stand-alone systems (Cseh et al.1997, Farber et al. 1998, Dorner et al. 2003, Wilantewicz and Varner, 2008 and Bernard et al. 2010). Only recently, some equipment has been commercially available for this purpose (CSM Instruments Applications Bulletin 2003, Sawa et al. 2006, and [www.tribometrix.com](http://www.tribometrix.com) 2013).

### **4.1 Description of the apparatus**

The experimental apparatus (Figure 4.1) consists of a vertical split tube furnace mounted in a universal testing machine (Hounsfield Test Equipment Ltd, Surrey UK). The specimen is supported horizontally on a stage inside the furnace and the indenter tip is assembled in a steel rod fixed to the movable cross head of the machine. Both the stage and the indenter rod or column are made of stainless steel (BS EN 10088-2 1.4301 / 1.4307/ ASTM 304) and are water cooled using a system consisting of copper coils placed in the sections outside of the furnace.

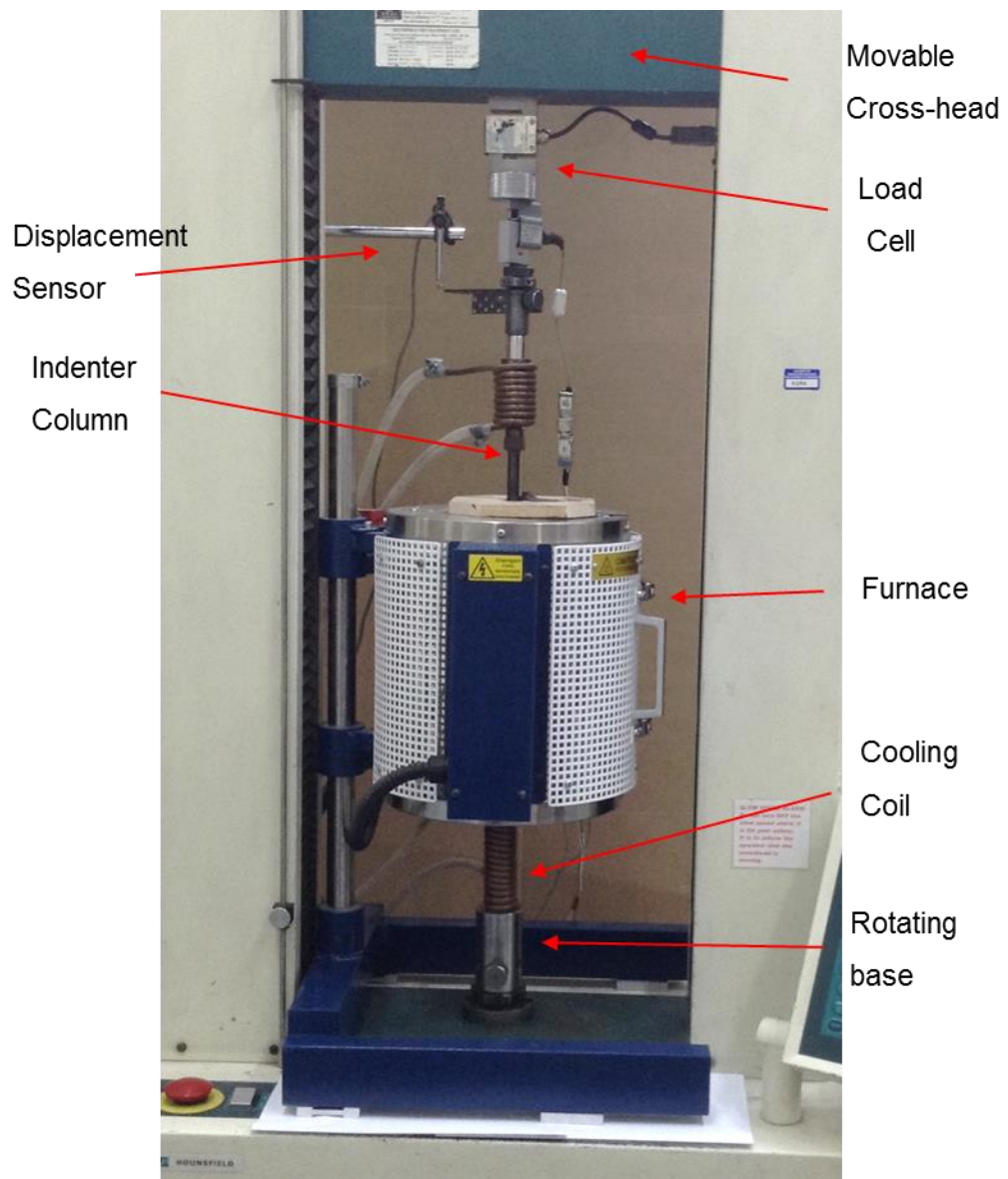


*Figure 4.1: Experimental apparatus for the indentation of glass at elevated temperatures.*

The vertical split tube furnace (Elite Thermal Systems Ltd, UK) was specially designed and built to fit inside the testing machine and has a maximum working temperature of 1050°C. However, in order to avoid damage to the sensors and to the testing machine, the maximum temperature at which the furnace can be used with the existing water cooling system is 650°C.

The furnace is operated with an automatic controller with the ability to program different heating, dwell and cooling ramps. The heating chamber length is 30 cm and the internal bore is 6 cm. The furnace ends are protected with specially fabricated seals made of refractory material to prevent the heating loss. The temperature variation found in the working range (520 to 560°C) did not exceed  $\pm 1^\circ\text{C}$ .

The stage that supports the specimen is a polished circular steel plate of 5 cm diameter and can be turned from outside the furnace (Figure 4.2). This feature along with an off-centred indenter column allows up to 6 indentations in the same specimen during the experiment.

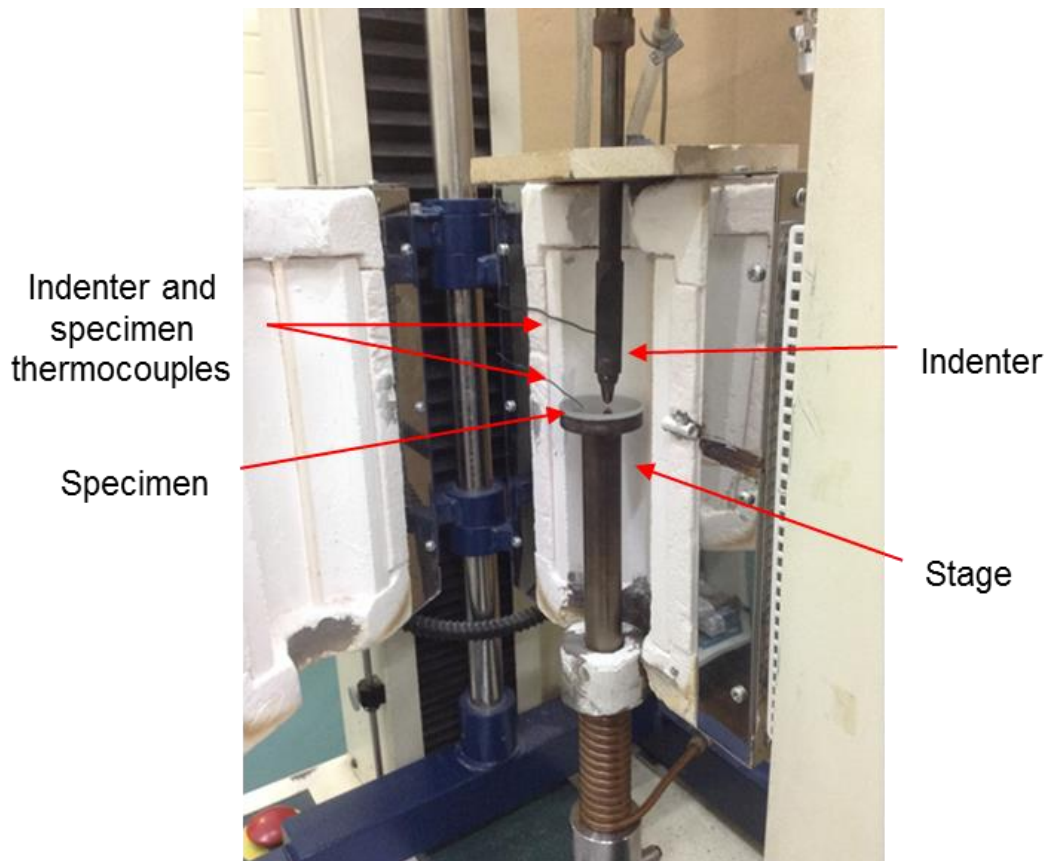


*Figure 4.2: Interior view of the furnace.*

Two indenter tips were acquired for the high temperature testing. One is a Vickers diamond tip which is a four sided pyramid with a face angle of  $68^\circ$  as

shown in Figure 4.3 a), and the other is a tungsten carbide Rockwell ball 6 mm in diameter, Figure 4.3 b).

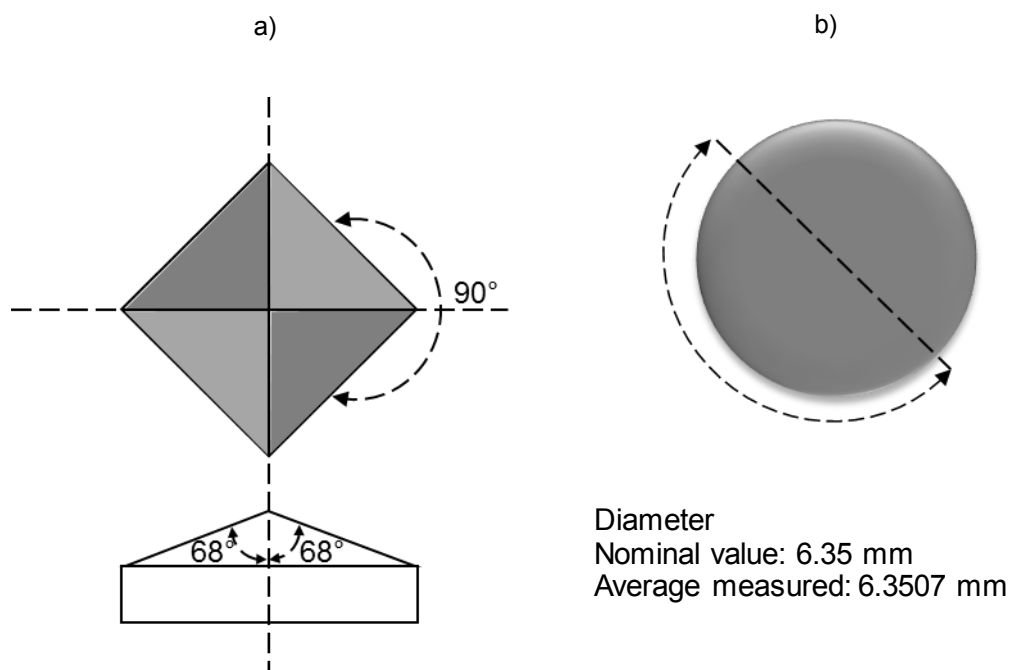


Figure 4.3: Indenter shapes and measurements a) Vickers, b) tungsten carbide ball

The indenter assembly is driven by the machine cross head and can be programmed to perform different types of movements. For the indentation testing, a routine was created according to the table below.

Table 4.1: Movements Routine for the indentation testing apparatus.

Action	Direction	Control parameter	Until
1. <b>Displacement (indentation)</b>		Displacement speed	Max. load
2. <b>Hold at max load (steady or creep)</b>		Max. load	Time
3. <b>Displacement (withdraw)</b>		Displacement speed	0 N Load

The load applied during the test is measured with a load cell (Hounsfield Test Equipment Ltd, Surrey UK) with a range of 0 to 1000 N which is installed in the indenter column in the section outside the furnace. A water cooling coil is placed before this instrument to remove heat transferred from the furnace through the indenter column.

The displacement is measured with a digital gauging probe (Mod. DP5, Solartron Metrology Ltd.) which has an accuracy of  $\pm 0.5 \mu\text{m}$  and a displacement range of 5 mm. This sensor is located parallel to the indenter column and measures the displacement of the crosshead against a fixed reference. Since it is not measuring the true displacement of the indenter, a system compliance study was conducted to account for the yield of the loading frame as described below in section 4.3.6.

The testing machine has the ability to register load and displacement during the testing, however, the data acquisition rate of the machine is low and it was found that especially at high speeds, the data recorded was not sufficient for the required analysis. For this reason it was decided to use a parallel data acquisition system (Mod. cDAQ.mx with analogue modules NI 9211 and 9237, National Instruments Corp. UK. Ltd) that registers the signals from a load cell mounted on the indenter column assembly and from the displacement sensor installed in the machine cross head. The temperature of the specimen and the indenter inside the furnace is also monitored with type K and N thermocouples and recorded using this same system. The data is monitored and logged on a PC using a data acquisition programme in Labview (National Instruments Corp. UK. Ltd) which is described in detail in the following section and in Appendix A.

## **4.2 Description of the Data Acquisition Program**

The Labview programming platform was used to create a graphical interface in a PC with the ability to read in real time and record the signals from the load, displacement and temperature sensors used in the indentation apparatus. Additional functions were programmed such as: the taring (due to the weight of the elements underneath the load cell) or zeroing of the

readings at the beginning of the experiment; the inclusion of time readings and the recording of the data into a spreadsheet.

Appendix A details the program code and shows a screenshot of the graphical interface with labels for the main controls and indicators.

### 4.3 Calibration and verification procedures

#### 4.3.1. Load cell

The load cell assembly readings were verified using three different weights. The weights were firstly measured using a calibrated scale available in the materials department at Sheffield University (Precisa Mod XT6200C-FR, Precisa Gravimetrics AG. Switzerland). Then, the load cell was loaded under compression using these weights and the readings were registered from the Hounsfield machine display and from the data acquisition system on the PC. The readings were compared and the results are shown in Table 4.2. The data from the Hounsfield machine display was taken purely for comparison since the values considered for the analysis are only those from the PC data acquisition system. Each set of data was taken ten times and the mean and confidence intervals (within 95%) calculated. It can be observed that there is a consistent difference of 1% between the weight values and the load readings from the DAQ. Therefore, the load data from the experiments was later adjusted for this difference.

*Table 4.2 Load cell verification.*

<i>Weight Blocks</i>	<i>Scale reading (N)</i>	<i>Hounsfield (N)</i>	<i>Data Acquisition system (N)</i>	<i>Difference (%) Scale-DAQ system</i>
		<i>Mean (95% C.I.)</i>	<i>Mean (95% C.I.)</i>	
<i>W1</i>	<b>9.81</b>	10 ( <i>not avail.</i> )	9.91 (9.92-9.90)	1.0%
<i>W2</i>	<b>49</b>	48.5 (48.7-48.3)	49.5 (49.53-49.46)	1.0%
<i>W3</i>	<b>168.33</b>	168.73 (169.2-168.3)	170.4 (170.7-170.1)	1.1%

### 4.3.2. Displacement Sensor

The performance of the displacement sensor was verified comparing its readings at different displacements with the machine display readings. The procedure is described below.

Once the two instruments were set to zero at a random position of the loading frame, the crosshead was moved at a fixed speed of 0.1 mm/min and stopped at different displacements as indicated in Table 4.3. In this case, the two readings were compared and the maximum difference found was 1  $\mu\text{m}$ , which in a normal experiment with displacements in the order of 50  $\mu\text{m}$  represents a maximum variation of 2%. As no systematic trend was discernible in this data it was decided not to adjust the data for this error. It is likely that this error is related to the thermal drift of the displacement sensor, which is evaluated in a different test described in Section 4.3.4.

*Table 4.3 Verification of displacement sensor by comparing with readings in the machine display. Values are in  $\mu\text{m}$ .*

<i>Displacement steps</i>	<i>Direction of movement</i>	<i>Machine Display reading</i>	<i>Displacement Sensor reading</i>	<i>Difference against Machine Display</i>
0	-----	0	0	0
D1	↓	26	25.4	-0.6
D2	↓	50	49.4	-0.6
D3	↓	77	77	0
D4	↓	102	102.5	+0.5
D5	↑	50	49.5	-0.5
D6	↑	0	1	1

### 4.3.3. Thermocouples

The system uses three thermocouples. One is integrated into the furnace to control its operation (type N), the second is in contact with the indenter column inside the heating chamber (type K) and a third one is in contact with the specimen (type N). The three thermocouples were verified using a high temperature thermocouple calibration furnace (Isotech Pegasus calibrator series 4853, Isothermal Technology Limited, Merseyside, England). It is expected in this test that the verified thermocouples would record a

difference of less than 2°C to consider them reliable according to the manufacturer's recommendation. The verification test results for the thermocouples are shown in Table 4.4. All of them showed less than the specified maximum variation allowed.

*Table 4.4 Verification of thermocouples used in the experimental apparatus.*

<i>Thermocouple</i>	<i>Thermocouple reading °C</i>	<i>Calibration Furnace °C</i>	<i>Difference °C</i>
<i>Furnace Control</i>	706.5	707.2	<b>0.7</b>
<i>Specimen</i>	716.8	717	<b>0.2</b>
<i>Indenter</i>	715.5	717	<b>1.5</b>

#### **4.3.4. Drift rate**

The drift caused by the expansion and contraction of the elements inside the furnace or in the displacement sensor might lead to a significant measurement error during the experiment.

Although sufficient time is allowed for the elements to reach thermal equilibrium before each test, it was decided to add a dwell time of 10 seconds at a fixed load of 5 N at the end of the unloading segment of each experiment (Figure 4.4). In the indentation experiments at high temperature, it is expected that the material stops flowing at this point of the unloading stage and the displacement readings are purely the drift of the sensor or the elements inside the furnace.

The drift measurement is carried out by plotting the displacement against time during this hold and a linear regression calculated. The data is adjusted with the drift rate, which typically did not exceed 0.05 µm/s.

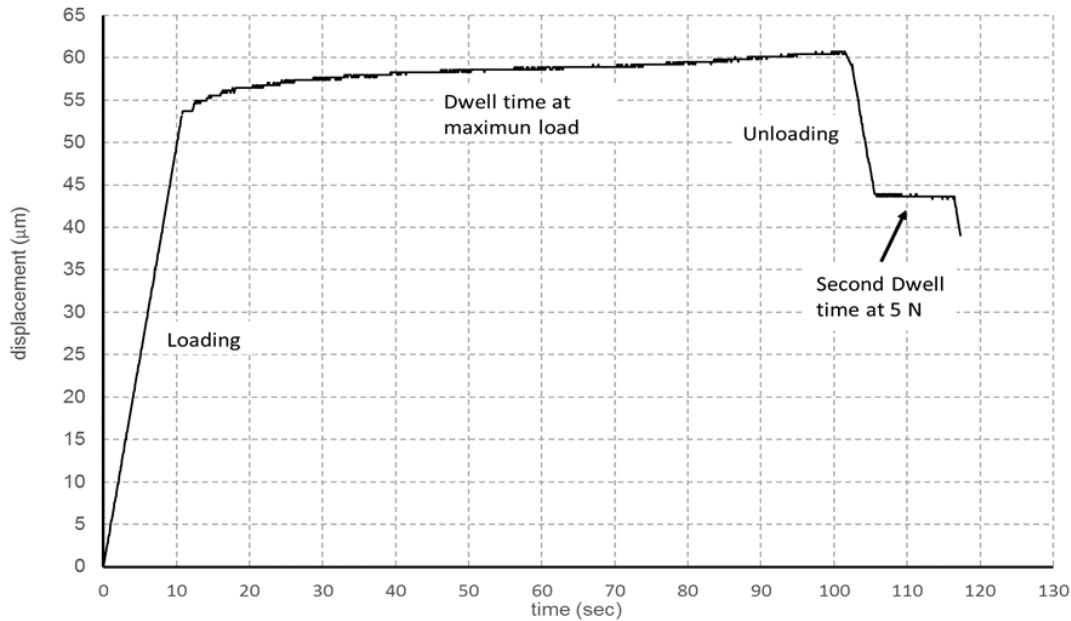


Figure 4.4: Displacement-Time curve of the indentation test at a maximum load of 50 N with a second dwell time at 5 N in the unloading stage.

#### 4.3.5. Tip Area Function

The calculation of the contact depth in indentation analysis relies on the geometry of the indenter as expressed via an area to depth relationship, as expressed in equation for the case of a perfect Vickers indenter.

However, manufacturing a perfect tip shape is not feasible and during use, there will be also some wear blunting the tip and affecting the area to depth relationship. Therefore, it is necessary to obtain a function that can account for the bluntness of the tip and can be used to correct the indentation data for this factor. This function is called the Tip Area Function (TAF).

In Section 3.2.2, the TAF was found by indenting a material of known elastic properties and the obtained function was used to correct the data. This is the preferred method in the case of nanoindentation since imaging the tip is difficult and time consuming. However, for the case of micro-indentation, the indenter size allows the use of optical techniques to measure the dimension of the tip in a more convenient way. In the case of the Vickers indenter used for the high temperature experiments, a 3D optical profilometer (Contour GT, Bruker Corporation, Coventry UK) was used to image and measure the indenter tip. For the case of the tungsten carbide sphere used

in the Hertzian experiments, the quality verification sheet supplied by the manufacturer was used as a reference since its size exceeded the limits of our equipment.

A three dimensional image of the Vickers indenter tip is shown in Figure 4.5. This image corroborates the existence of a certain degree of bluntness at the tip of the pyramid.

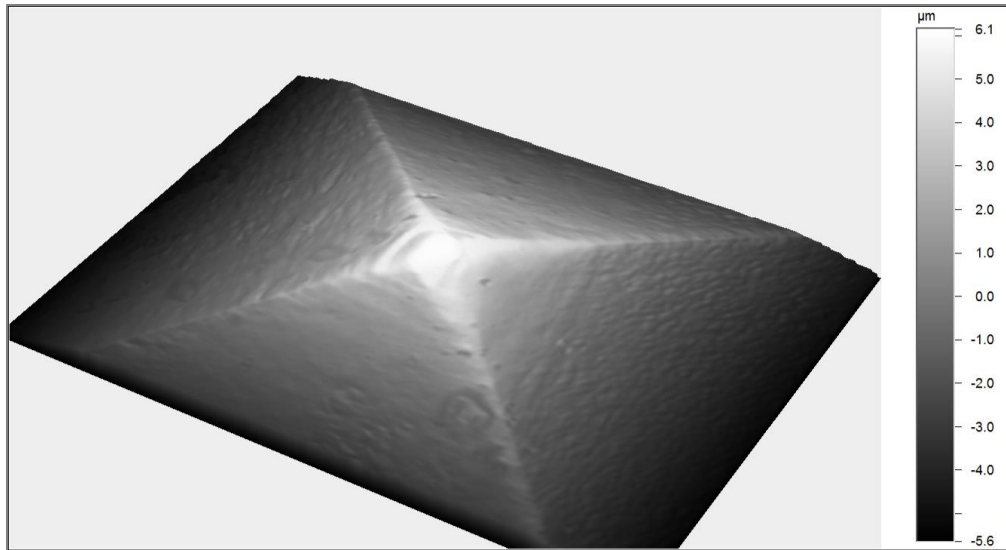


*Figure 4.5: Three dimensional image of Vickers indenter tip used in the High temperature experiments.*

Using the equipment software, the profile of the tip can be obtained within a scaled grid and used to measure the deviation from the ideal shape. Figure 4.6 shows the profile image and the distance from the actual tip to the theoretical location of the pyramid vertex.

The Tip Area Function calculated from the imaging and measurement of the indenter tip and used to obtain the corrected contact area  $A'$  resulted as follows:

$$A' = 24.504(h_c^2 + 2.78h + 1.9321) + 47.34 \quad 4.1$$

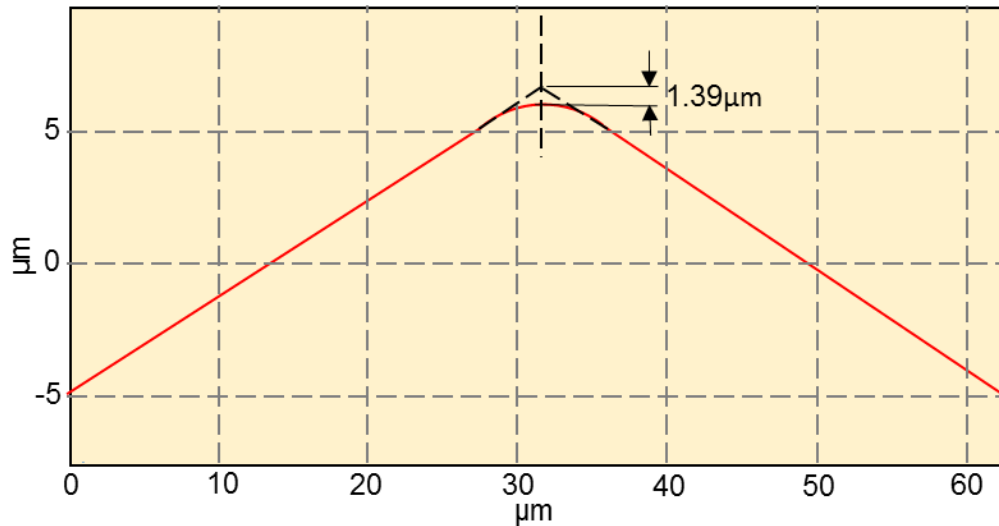


Figure 4.6: Profile of Vickers indenter tip obtained from the optical profilometer.

#### 4.3.6. Machine compliance

The analysis to obtain the mechanical properties from the load-displacement curves of the indentation experiments requires the use of the real displacement of the indenter tip while penetrating the specimen surface. However, due to the difficulty of finding a sensor that could withstand the working temperatures and that could be installed inside the furnace, it was decided to place the sensor on the moving cross-head of the universal testing machine. The downside of this arrangement is that during the application of load to the specimen, there is a reaction force taken by the cross-head of the compression machine and by the indenter column. This reaction is transformed into a deflection of these elements proportional to the load and registered by the displacement sensor during the test. It is necessary to measure this error and adjust the load-displacement curves in order to obtain a true value of the indentation depth.

The effect of this calibration is a shift of the load-displacement curve to the left as can be seen in Figure 4.7

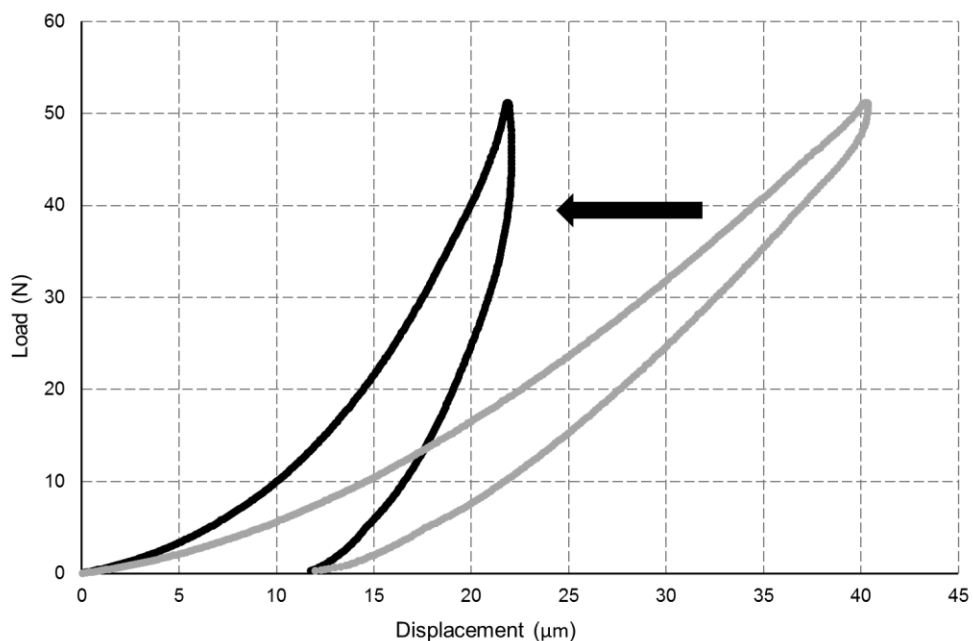


Figure 4.7: Load-displacement curve adjusted for machine compliance

The total compliance of the system during indentation is defined as the yield of the loading frame and the specimen compliance. The system can be modelled by two elastic springs as depicted in Figure 4.8 and expressed in Equation 4.2. From this model is possible to calculate the specimen compliance indenting a material of known elastic properties, such as fused silica, and subtract this value from the total compliance to obtain the yielding of the loading frame.

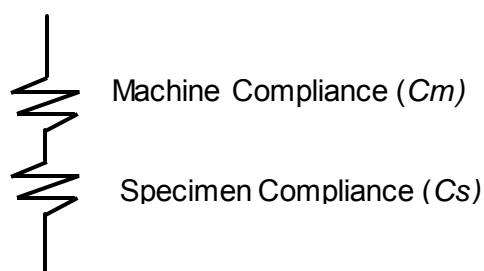


Figure 4.8: System compliance for the indentation test.

The total compliance is expressed as:

$$C_T = C_S + C_m \quad 4.2$$

There are different procedures that can be used to calculate the compliance factor that is required to adjust the indentation data. In the course of this study, experimentation with two methods were carried out with fused

silica and the results of both tested in our data of indentation of Soda Lime Silica glass at room temperature, from which the elastic modulus and hardness are also well known. These two procedures are described in the following subsections.

*Compliance measurement using Vickers indentation of fused silica.*

In this method, a fused silica specimen (50.8 mm dia. x 3.18 mm thick disk. Alfa Aesar, Ward Hill, MA USA) with an elastic modulus of 72 GPa and a Poisson's ratio of 0.17 was used for the loading frame compliance calibration. The Vickers diamond indenter used for the test has an elastic modulus of 1141 GPa and a Poisson's ratio of 0.07 (Tool No. 109667, Euro Products Ltd, Stourbridge, UK), giving a reduced modulus of 69.6 GPa for this combination of indenter and specimen.

Since the compliance of the loading frame is proportional to the load applied, a series of indentations at different peak loads were carried out in the load range available in the apparatus. In this case, 50, 100 and 200 N. The indentation was done in a sequence of maximum to minimum with at least three repetitions at each load.

The load-displacement curves were obtained for each experiment. Stiffness was firstly calculated fitting a second degree polynomial equation to the upper part of the unloading section and finding the derivative of this equation evaluated at the maximum load (Figure 4.9). The value calculated accounts in this case for the stiffness of the specimen and the machine ( $S_T$ ).

The unloading section on Figure 4.9 shows a "bulge" at the start of the unloading as can be observed. This effect could be attributed to the elastic recovery of the loading frame. For the analysis, the first part of the unloading section was discarded (50 to 43 N) in order to obtain a better fitting.

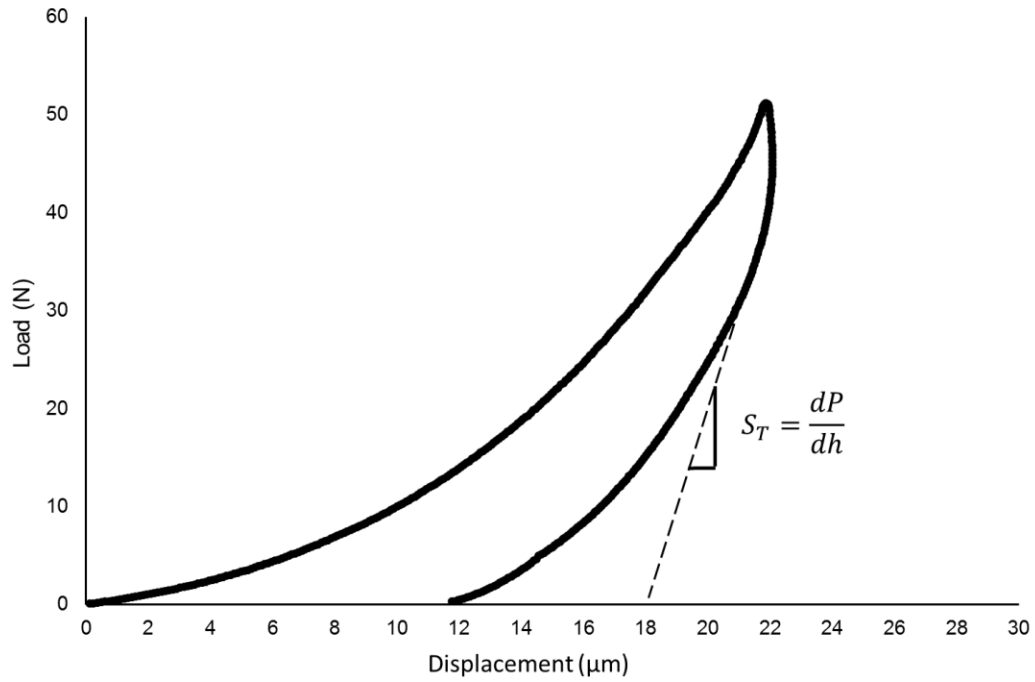


Figure 4.9: Total Stiffness ( $S_T$ ) for the specimen and the machine

The stiffness is the inverse of the compliance, therefore we can write the total compliance of the system  $C_T$  as:

$$C_T = \frac{1}{S_T} = \frac{dh}{dP} \quad 4.3$$

Or:

$$\frac{dh}{dP} = \frac{1}{S_S} + C_m \quad 4.4$$

where  $S_S$  is the specimen compliance.

Rewriting equation 2.21, the contact depth can now be calculated:

$$h_c = h_{\max} - \varepsilon \frac{P_{\max}}{S_T} \quad 4.5$$

where  $\varepsilon$  is a geometric factor depending of the indenter type; for the case of a Vickers indenter  $\varepsilon = 0.75$ .

Since the indentation is carried out in a material of known elastic properties, the total compliance can be now expressed in terms of the

stiffness of the specimen. Substituting equations 2.24 and in equation 4.4 we obtain:

$$\frac{dh}{dP} = \left[ \sqrt{\frac{\pi}{24.504}} \frac{1}{2E_r} \right] \frac{1}{h_c} + C_m \quad 4.6$$

Equation 4.6 can now be plotted (Figure 4.10) and the  $C_m$  factor obtained by fitting a linear equation to the data (Equation 4.7)

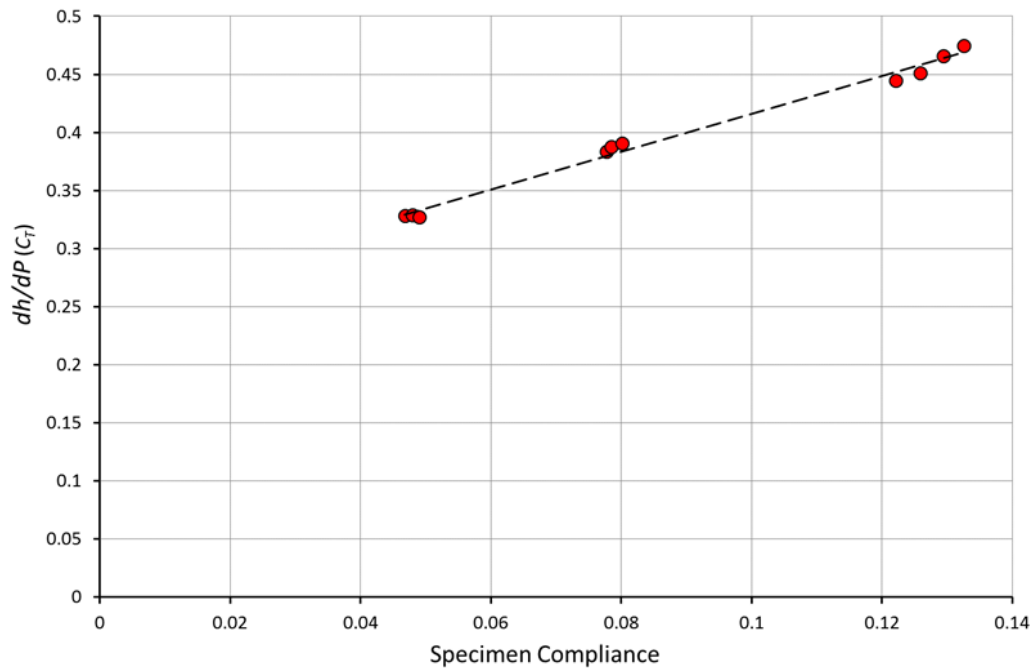


Figure 4.10: Machine compliance factor ( $C_m$ ) obtained with the Vickers indentation on Fused Silica

$$\frac{dh}{dP} = 1.63C_s + 0.2533, \quad R^2=0.9905 \quad 4.7$$

Machine Compliance Factor ( $C_m$ ) = 0.2533

The displacement data obtained from the indentation experiment is adjusted by the factor above according the following formula:

$$h_{adj} = h - (0.2533P) \quad 4.8$$

The indentation test carried out on fused silica to find the machine compliance factor was done at elevated temperatures as well in order to evaluate if the temperature had an effect in this correction factor. The

comparative results at 22, 520 and 560°C shown in Figure 4.11 indicate that there is not a statistically significant difference, since the calculated confidence intervals (within 95%) overlap.

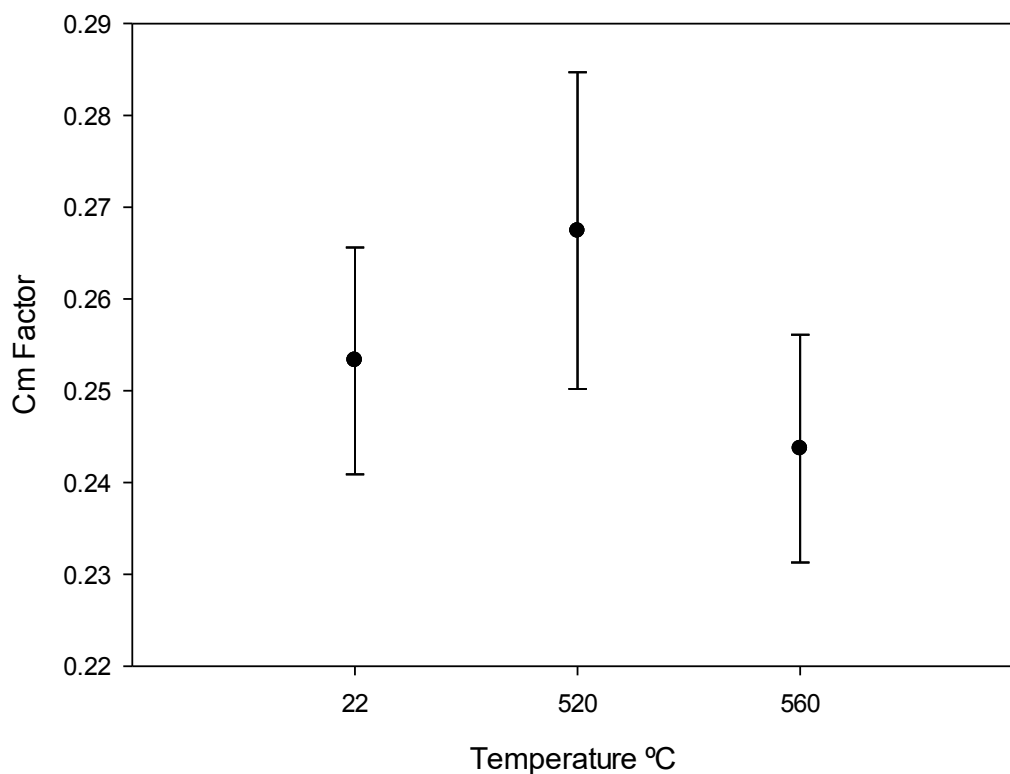


Figure 4.11: Machine compliance factor calculated with the indentation of Fused Silica at different temperatures. The bars indicate the 95% confidence intervals for the mean.

The differences in the elastic properties of the fused silica and the diamond indenter tip with temperature were taken into account in this analysis. Table 4.5 describes these values at the same temperatures of the tests (Szuecs et al. 1999, Rouxel 2007).

Table 4.5 Elastic properties with temperature of Fused Silica and Diamond tip indenter.

	22 °C		520°C		560°C	
	<i>E</i> (GPa)	<i>v</i>	<i>E</i> (GPa)	<i>v</i>	<i>E</i> (GPa)	<i>v</i>
<b>Fused Silica</b>	72	0.171	76.97	0.171	77.33	0.171
<b>Diamond Tip</b>	1141	0.07	1082	0.07	1078	0.07

*Compliance measurement using Hertzian indentation on fused silica*

A fused silica disk with the same characteristics mentioned previously was indented at room temperature using a tungsten carbide sphere of 6.35 mm diameter, elastic modulus of 676 GPa and Poisson's ratio of 0.26 (Tool No. 109595, Euro Products Ltd, Stourbridge, UK) resulting in a reduced modulus for the indenter and specimen of 67.3 GPa. The maximum indentation load used was 50 N and after every experiment the specimen was inspected to verify that no crack has been generated. Unlike the Vickers indentation, in this test the deformation is elastic during both the loading and unloading and therefore no permanent deformation is created if no cracking occurs.

The loading and unloading speed of the crosshead for this test was 0.1mm/min with a dwell time of 0.5 seconds at maximum load. The indentation experiment was repeated 10 times in the same location of the specimen surface and with the same parameters.

The output of the test is the measured displacement  $h_m$  and the load  $P$ . The penetration of the indenter in the surface or true displacement  $h$  is found rearranging equation 2.15 to the following form:

$$h = \left( \frac{3P}{4E_r R^{1/2}} \right)^{2/3} \quad 4.9$$

Therefore, the machine compliance  $C_m$  can be found by plotting the following expression and obtaining the equation that best fits the curve:

$$h_m - h = C_m P \quad 4.10$$

Figure 4.12 shows the loading and unloading curves obtained from one experiment. An important feature observed is that the curves in both directions are not identical indicating that the compliance behaviour is different for loading and unloading probably because the mechanical characteristics of the equipment.

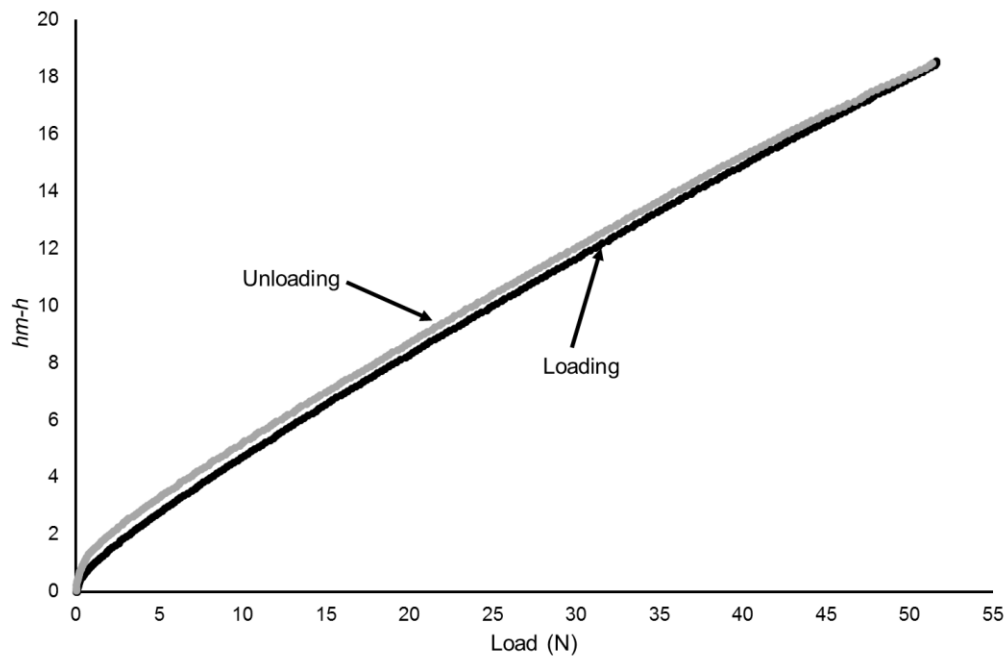


Figure 4.12: Loading and Unloading curve of Hertzian indentation on Fused Silica

Another important characteristic is that the relationship between the displacement and the load is nonlinear as can be readily seen. Because of this, different equations were fitted and the best result was obtained with a polynomial of the form:

$$C_m P = aP^2 + bP + c \quad 4.11$$

The data was fitted in the range of 5 to 47 N (Figure 4.13) and the residuals plotted in order to verify that the polynomial equation provides a good fit.

The beginning and the end of the unloading section (47 to 50 N and 0 to 5 respectively) were not considered in the fitting because it showed a curve completely different to the shape of the rest of the curvature. The investigation of the exact cause of the behaviour of the machine compliance at the beginning and end of the unloading was not pursued further, however, this same behaviour has been observed in compression testing machines in other studies (Kalidindi et al. 1997 and Ståhlberg et al. 2005), and is generally attributed to the initial settling of the fixtures and the sample or to the motion of the mechanism itself.

It was observed as well that the loading curve was different than the unloading, however an equation of the same form provided good fitting for both cases but different coefficients were obtained and used in the calibration of the experimental data.

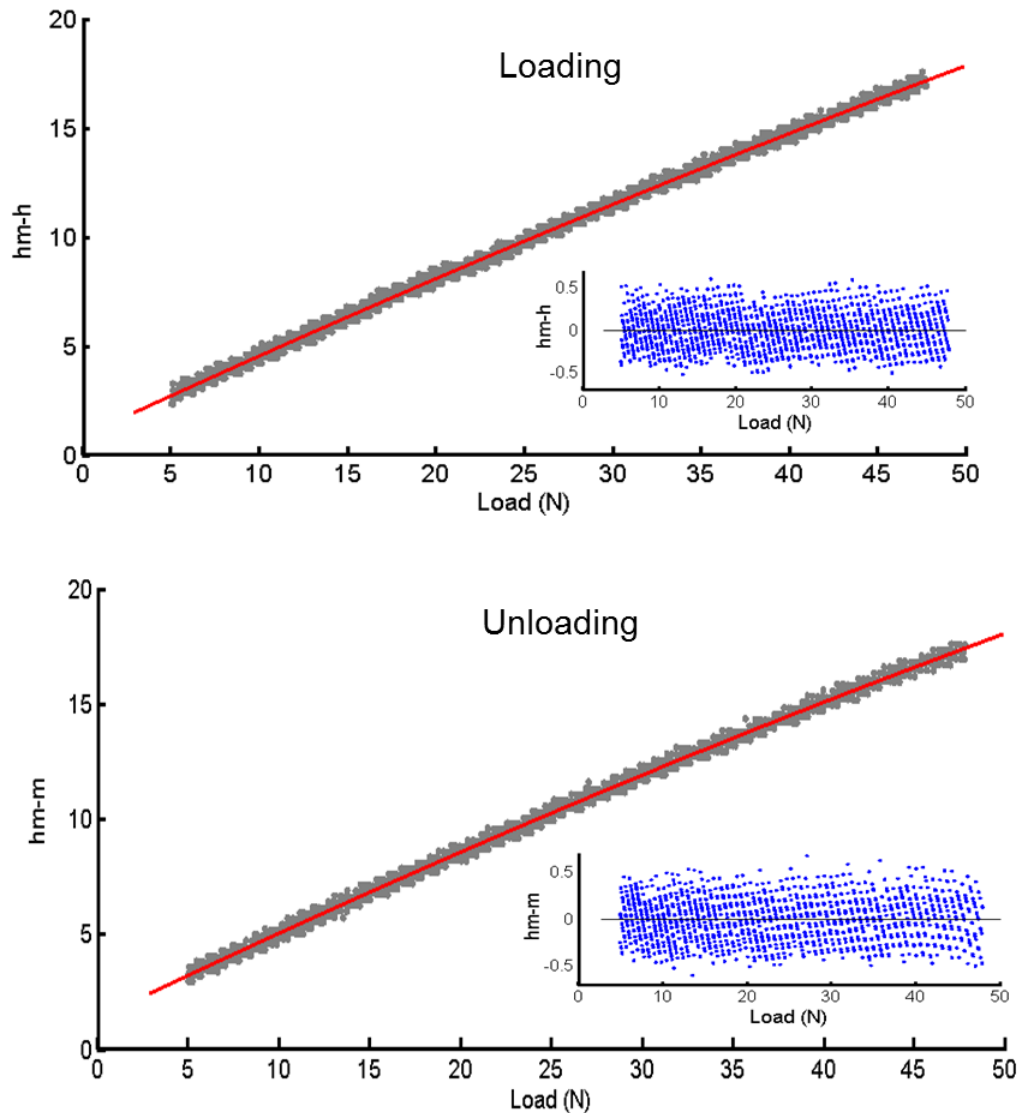


*Figure 4.13: Loading and unloading curves with second degree Polynomial Fitting. Residuals shown in the inset.*

The data in the calibration testing shows a periodic pattern which is more evident in the residuals plot. This pattern is due to the different acquisition rates of the displacement sensor and the load cell. In this case, the displacement sensor acquires the data at lower rate than the load cell, but the rate was deemed sufficient for the purposes of the test and the analysis, and does not affect the synchronization of the data.

In addition to the graphical examination of the fitting results for the quadratic functions, the coefficients and the numerical results were also obtained. Table 4.6 shows the goodness-of-fit statistics were it can be seen by examining the adjusted R-square and the sum of squares due to error (SSE) statistics that a good fit was obtained.

*Table 4.6 Numerical results of the quadratic fitting to loading and unloading curves.*

Function	Section	Coefficients			SSE	Adj.
		<i>a</i>	<i>b</i>	<i>c</i>		R-square
Quadratic	Loading	-0.0007	0.3763	0.8454	73.16	0.9971
	Unloading	-0.0009	0.3786	1.33	73.12	0.9969

#### 4.4 Conclusions

A laboratory apparatus was built to study the contact at elevated temperatures. The apparatus consisted of an integration of different systems capable to perform Vickers and Hertzian indentations up to a temperature of 560°C. The displacement was given by a mechanical testing machine that already existed in the laboratory which was capable to control displacement of the crosshead in both directions. The indenter column assembly and the specimen support were attached to the crosshead and the machine base respectively. A tube furnace was specially design and built to be integrated into the testing machine. This furnace had a controller capable to follow heating and cooling ramps and to maintain a steady temperature with a minimum variation for the desired period of time. A water cooling system consisting of copper coils was used to maintain the sections of the indenter column and specimen stage that were outside the furnace at a safe temperature. Displacement, load and temperature sensors were integrated into the apparatus and the test parameters were monitored and recorded using a data acquisition system from where the data was extracted and analysed afterwards.

All the sensors readings and the data acquisition system were carefully calibrated using external references. The size of the indenters used in this

micro and macro-indentation device allowed to use an optical profilometer to obtain the deviation of the indenter tip from the ideal shape and find the relation needed to adjust the data for this factor (Tip area function calibration).

The main challenge faced during the start-up of this apparatus was to obtain the accurate displacement reading needed to obtain the penetration of the indenter tip into the specimen surface. As any mechanical testing machine, there is some compliance of the loading frame that needs to be measured and compensated to obtain the real displacement. Standards methods described in the literature were initially used with poor results. These consisted in the Vickers indentation of a material of known elastic properties at different fixed loads from where the real displacement is determined. However, it was found that the Hertzian indentation in fused silica provided a better description of the compliance because it was possible to observe the yielding over the complete loading range while a pure elastic deformation was generated in the fused silica (if no cracking occurs) instead of the elastic-plastic deformation created by the Vickers indenter. The specimen displacement was subtracted from the total displacement and the compliance obtained. Two main features of the compliance in the machine were found. Firstly, the compliance had the form of a curve over the loading range instead of a line. And secondly, the compliance was different for the loading and the unloading stages. Equations that described both behaviours were obtained and used to adjust the displacement data of the experiments. Compliance tests were carried out also at elevated temperatures and it was found a negligible difference with the compliance test at room temperature, allowing the compliance test to be performed before each experiment run.

## 5. High temperature contact with the glass

### 5.1 Introduction

As a preamble to the investigation of the response of the glass to contact at room and high temperature, an industrial case of surface damage originated during the bending of automotive glass was studied. The analysis of this case led to a research in the laboratory to study the response of the surface to sharp and blunt indentation near and at the glass transition temperature.

The response of the Soda Lime Silica float glass surface to contact was investigated at 560, 540 and 520°C using the instrumented indentation apparatus described in Chapter 4. Dilatometry and Differential Thermal Analysis (DTA) were used to find the  $T_g$  of this glass.

A full factorial Design of Experiments (DoE) was carried out at 560°C with Vickers indentation to investigate the effect on the hardness of the variables: loading speed, unloading speed and the dwell time (details in section 5.4). The hardness was obtained by measuring the residual imprint on the surface with optical microscopy.

Both the tin and the air surfaces of the float glass were tested with Vickers indentation at different temperatures including room temperature, and the behaviour of the principal properties such as hardness, plain strain modulus and creep were studied. Hertzian indentation was studied only at 560°C. The characteristics of the residual imprint were also analysed using optical profilometry and microscopy.

In the final part of this chapter, the response of the surface was studied using viscoelastic models, and it was found that equations that represent Maxwell and Kelvin mechanical elements provide an adequate description of the response of the glass to contact when is in the viscoelastic state.

## 5.2 Case study of the contact at elevated temperatures in an industrial process

### 5.2.1. Background

The contact of the glass surface with the mould during the forming process of automotive windscreens is reviewed in this section. The morphology of the defects generated by the contact at elevated temperatures is analysed by means of optical microscopy, optical profilometry and SEM/EDX.

As described in section 2.3, during the bending and annealing process of the two panes of glass that make up the windscreen, the glass travels horizontally supported on a ring mould that makes contact with the surface of the glass just a few millimetres in from the edge of the pane (Figure 5.1). The mould is a stainless steel frame and the ring that makes contact with the glass is a profile of the same material of approximately 3mm thick. To prevent the adhesion of the glass to the steel mould during heating, the contact surface of the mould is frequently lubricated with a graphite base solution, applied manually with a brush.



*Figure 5.1: Photograph of the two panes of glass over the mould entering the bending furnace. (Courtesy of Vitro Automotriz S.A. de C.V.)*

The contact of the glass with the mould at high temperatures generates some marks on the surface that affects the aesthetics of the final product. In the past, the presence of this defect was not important for the car manufacturers since the windscreens used to have a rubber or plastic moulding installed on the periphery with a flare large enough to cover the mould marks. Nowadays, modern car windscreens do not use such moulding anymore and the glass edge is exposed. The moulding was removed from the new designs to provide a uniform surface between the glass and the car body, thereby improving the aesthetics from the car manufacturer's perspective.

The size and quantity of the mould marks in a windscreen varies depending on the process parameters and size of the part. Usually, windscreens that require more heat to bend because of the thickness, curvature or size are more prone to having mould marks. Although the size of the marks is on the scale of microns, they are noticeable especially with reflected light as can be observed in Figure 5.2. A solution that some glass manufacturers have adopted to eliminate the mould marks is the use of a stainless steel cloth that covers the metallic ring. However, this solution is expensive and requires continuous replacement of the cloth increasing the maintenance time of the mould and therefore the overall cost of production.



*Figure 5.2: Mould marks can be observed close to the edge of a finished windscreen (labelled with a red circle). The location of the marks correspond to the area that is in contact with the mould ring.*

### 5.2.2. Analysis techniques and results

Small sections from the edge of several windscreens with mould marks were obtained from an automotive glass manufacturer (Vitro Automotriz S.A. de C.V). Sections of 10 mm x 10 mm were cut around the defects and initially these were observed in the microscope at different magnifications and polarized light (Microscope Nikon Eclipse Mod. LV150, Japan). Different configurations and characteristics were observed in the specimens as can be seen in Figure 5.3. Some marks had the shape of a scratch or a pit, and some others had particles embedded in the surface. Most of the mould marks observed had a size between 50 and 100  $\mu\text{m}$  and a few of them exceeded 150  $\mu\text{m}$ . Some of the particles embedded in the surface were analysed further with the use of the optical profilometer and the SEM/EDX.

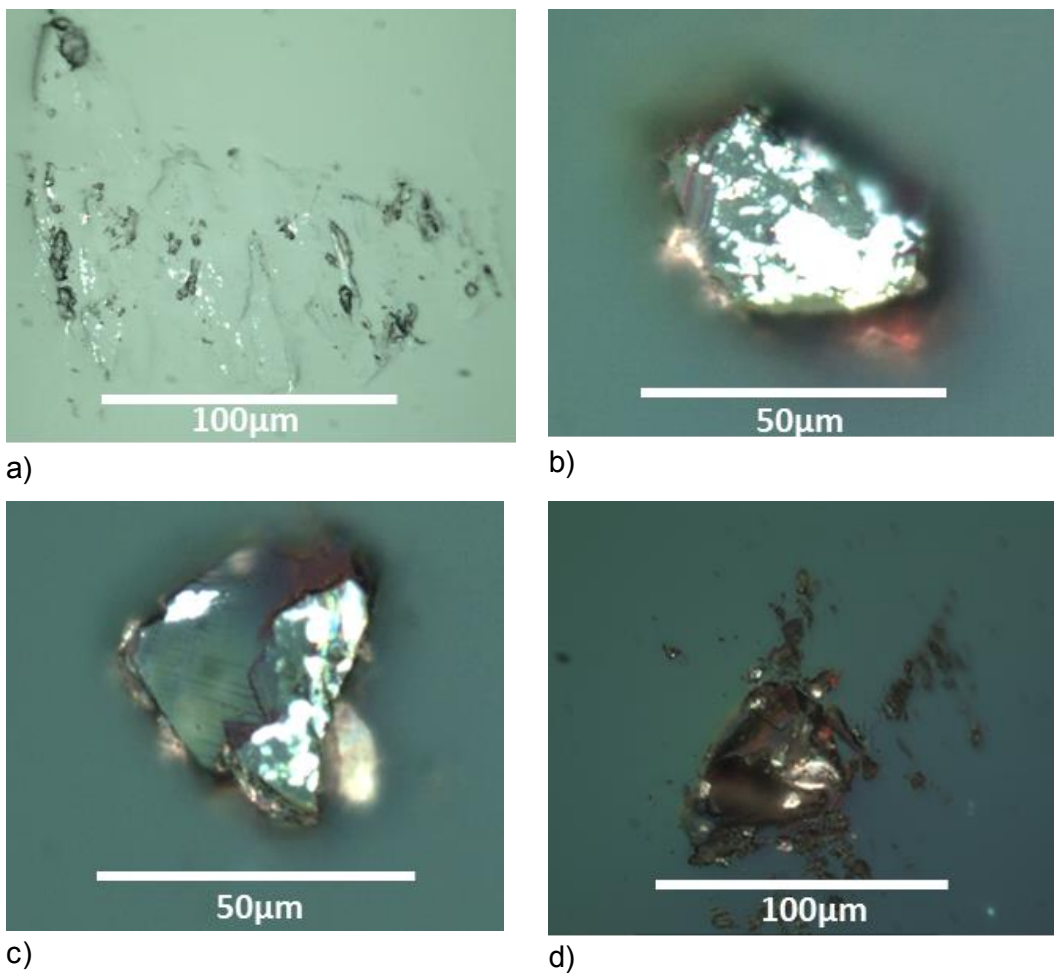


*Figure 5.3: Micrographs of mould marks observed in the optical microscope. Image a) shows residues of foreign elements along with scratch type marks. Images b) and c) show embedded particles with a glossy surface, and image d) shows an opaque embedded particle.*

A 3D image and the profile obtained with the optical profilometer (Figure 5.4) of the embedded particle shown in Figure 5.3b, revealed a circular area of approximately 300  $\mu\text{m}$  diameter in the form of a crater that extends around the particle.

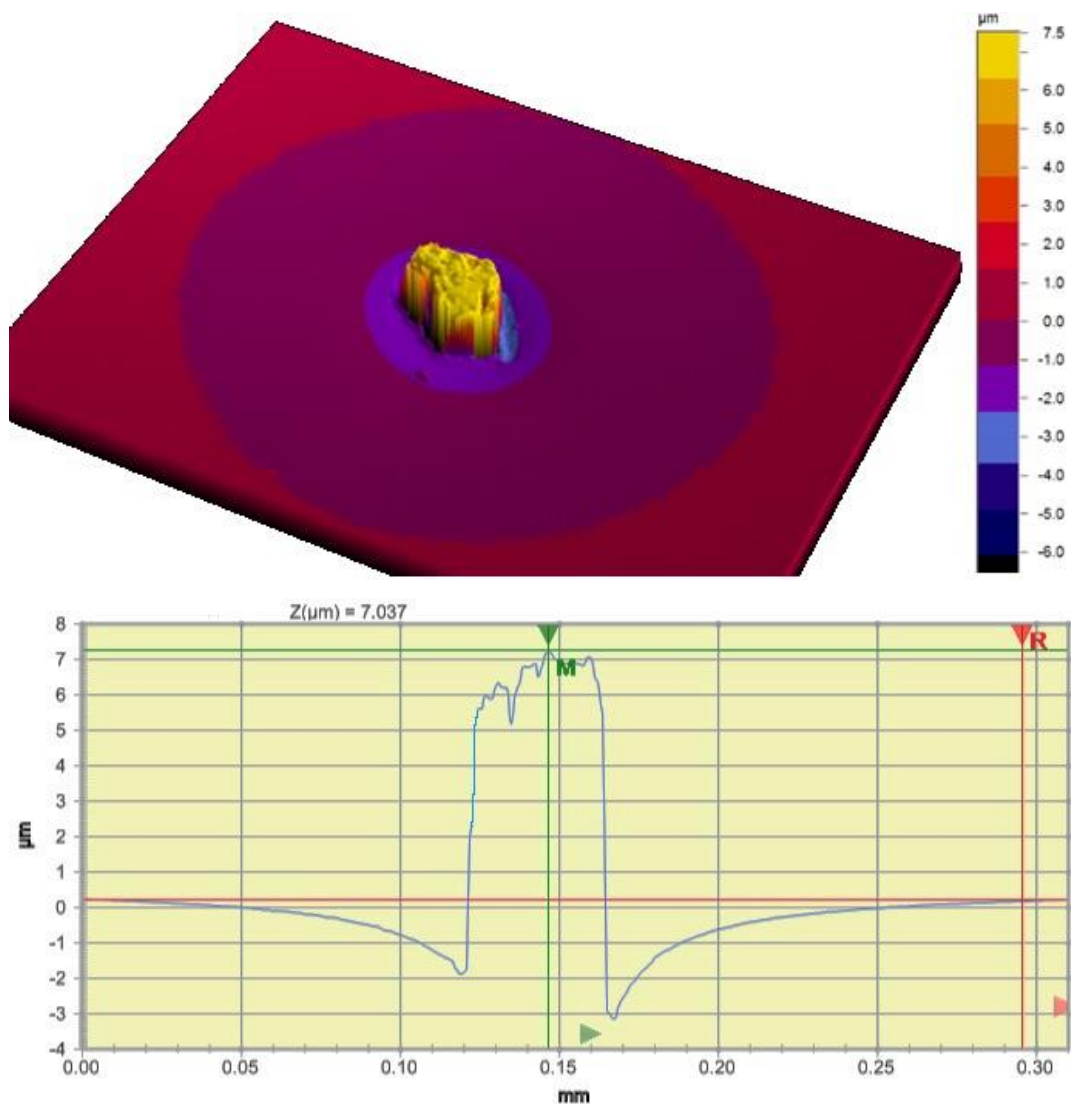


*Figure 5.4: Optical profilometry of an embedded particle in a glass specimen. The profile in the bottom image shows the height of the particle (distance marked between the red and green reference lines), the penetration depth and the profile of the affected area.*

In some specimens, a pit in the surface was observed and a circular deformed area was also exhibited. In the case of Figure 5.5, the pit seemed to be caused by the contact of a sharp particle as can be seen in the profile analysis shown in the same figure. The deformed circular area around the pit is in the form of a crater of approximately 150  $\mu\text{m}$  diameter. The depth of the pit is close to 8  $\mu\text{m}$  as can be seen in the optical profilometer image below.

The profile of the affected area was verified using contact profilometer to rule out the possibility of an erroneous reading from the optical profilometer due to the possible change in the refractive index around the area of the particle.

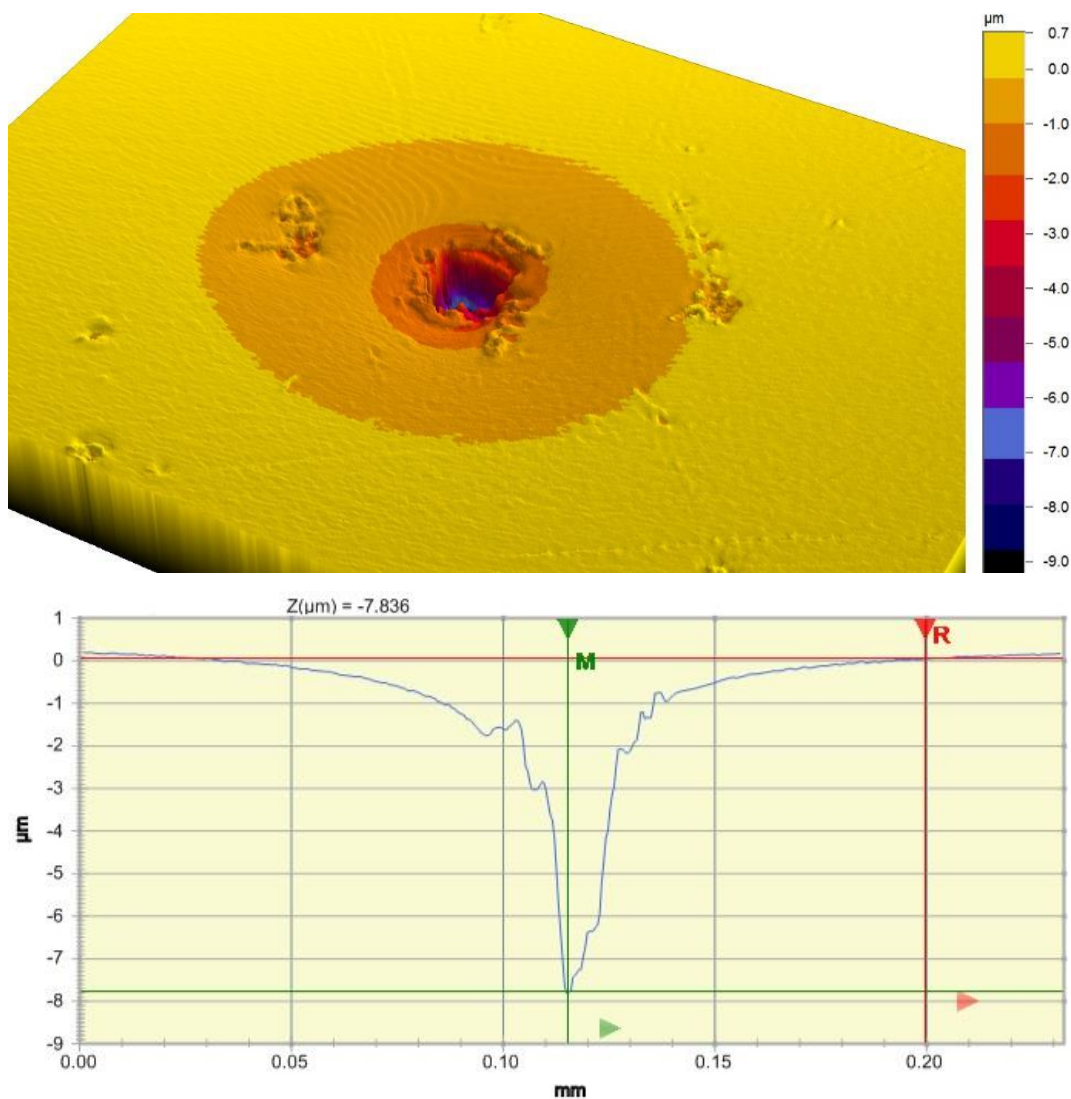


*Figure 5.5: Pit on the surface of a mould mark specimen. The red and green lines in the optical profilometer image are aids to measure the depth of the feature from the glass surface.*

The observations in the optical microscope also revealed a glossy surface in some of the particles embedded on the specimens. Some of the particles were analysed by means of SEM/EDX (JSM 6400, JEOL Ltd. Tokyo, Japan equipped with an X-ray detector Oxford Instruments, Oxfordshire, UK) to find their composition and possible origin. X-ray analysis of various focalized

points over the particles was undertaken using a beam energy of 20 keV, and a probe current of  $10^{-9}$  A.

The chemical analysis was targeted on three regions of the particle (Figure 5.6) using a point beam analysis. The first region was the glossy feature of the particle, the second was an apparent pristine surface on one side and the third region was the glass surface close to the particle.

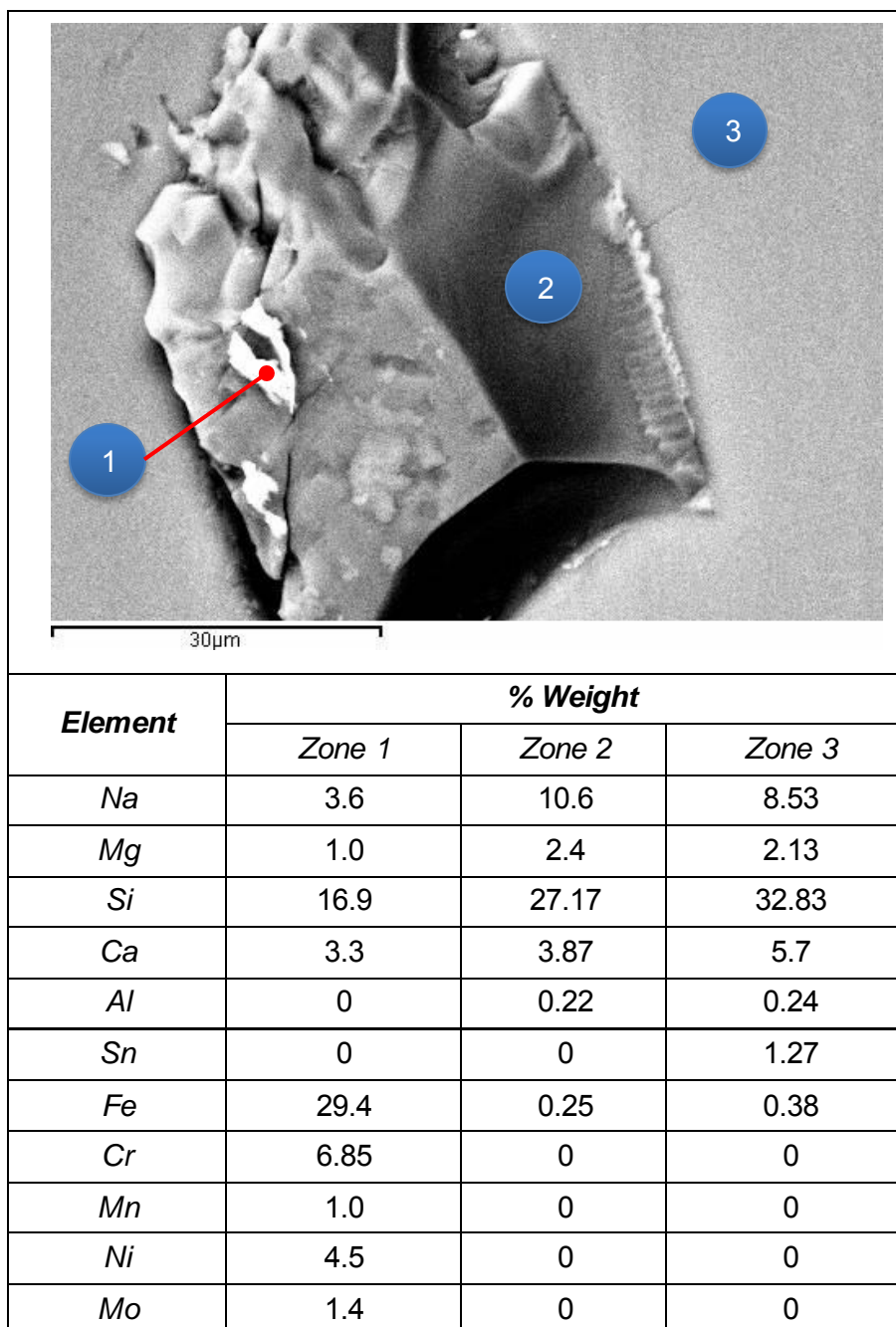


Figure 5.6: SEM image of the particle embedded in the glass surface and the principal chemical elements found in the 3 regions analysed by EDX identified with blue circles and labels.

Due to the interaction volume of the SEM beam and the size of the region analysed, it was not possible to obtain the exact composition of the features (Reed 2005). However, the analysis made it possible to obtain a broad idea of the main element present in each of the three regions. The table included in Figure 5.6 describes the main constituents obtained by the EDX analysis. It can be seen that in the small bright region labelled 1, the presence of metallic elements such as Fe, Cr, Ni, and Mo stand out. These elements correspond to the main constituents of the stainless steel used in the mould ring which is an AISI 316L steel that has a chemical composition in wt% of 16-18% Cr, 10-14% Ni, 2-3% Mo, 2.0% Mn, 0.75% Si, 0.045% P, 0.030% S, 0.03%C, and 0.1% others (British Stainless Steel Association 2014). Region 2 has a chemical composition similar to the one obtained for region 3 which is the glass substrate where the particle is embedded.

From the previous analysis it can be inferred that the particle is glass with some residues from the metallic mould. These residues were present as well in the other particles observed in the microscope (Figure 5.3). Two additional specimens were analysed in the SEM obtaining similar results

### **5.2.3. Discussion and Conclusions**

From the previous analysis it is clear that glass particles are one of the causes of the mould marks on the windscreens. Nevertheless, some other possibilities could be: the finishing of the mould ring, corrosion products from the mould on the surface, or particles of another origin.

In order to rule out the possibility that marks were also caused by the mould ring finishing or corrosion products, an experiment was conducted in the windscreen manufacturing facility. In this experiment, a testing mould was polished by mechanical and manual means until it reached a mirror-finish in the contact surface with the glass. The roughness of the surface was measured before and after polishing using a handheld roughness meter (SurfTest SJ-210, Mitutoyo Japan). The average roughness parameter ( $R_a$ ) in the contact surface was reduced from a value of 87 to 17 nm improving substantially the quality of the contact surface as can be observed in Figure 5.7. The mould was carefully inspected and sent to the production process.

All the parts processed with this mould were inspected for mould marks right after they came out of the furnace. The parts processed in the first two hours didn't exhibit any marks but eventually the marks started to appear, most of them located on the same area of the windscreens. The mould was inspected at the end of the production run and no apparent signs of attached particles were found, but the surface exhibited some signs of oxidation. The ring surface was contaminated with the residues of the anti-stick or release agent and was not possible to perform detailed inspection of the surface looking for attached particles on it.

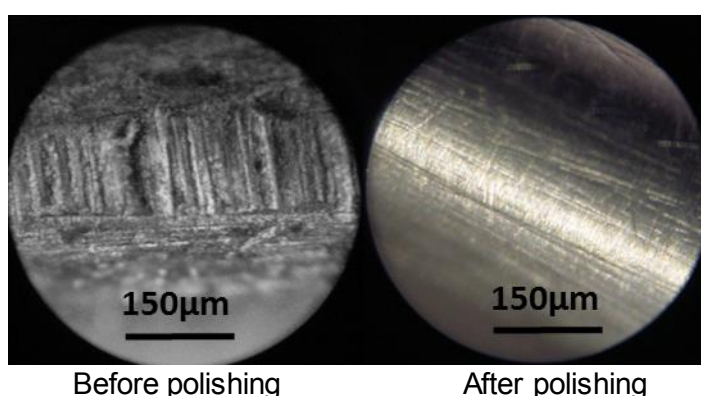


*Figure 5.7: Images of mould contact surface before and after polishing observed with optical microscope. Ra was reduced from 87 to 17nm.*

The experiment described above and the analysis of the particles indicates that it is possible that the majority of glass particles may adhere to the mould surface and cause the marks in the same location of the windscreens processed on it. Also, although the surface quality of the mould was improved, this was not the most important factor in generating the marks.

The adhesion of glass to metal is a subject that has been studied in the glassware moulding industry, as is in the case of the moulding and forming of precision optical lenses and in the glass-to-metal seals for the fabrication of electric bulbs. The adherence between glass and metal is promoted by the presence of an oxide layer which is formed rapidly on the metal surface by the effect of temperature. Presumably, these metal oxides will adhere to the glass because of the interaction of the atoms on the surface of both materials

which will try to expand their structure creating a chemical bond (Holland 1964, Donald 2009).

SLS glass can adhere to steel at temperatures as low as those close to its glass transition (560°C) enhanced by the pressure between the glass and the mould (Rieser et al. 2008). In addition, the glass might remain adhered to steel when it is cooled down to room temperature as has been demonstrated experimentally (Pech et al. 2004).

In the fabrication of lead-in electrodes for electric lamps, where good glass-to-metal seals are desired, Fe-Ni-Cr-Co alloys are used because the thermal expansion can be matched to that of the glass by adjusting the alloy composition but, more importantly, because these alloys generate a firm oxidation layer that adheres well to the metal base and to the glass surface (Hull and Burger 1934). It can be noticed that the elements of these alloys (except Co) are present in the stainless steel used in the mould ring and also traces were found in the chemical analysis of the embedded particle on the glass surface.

Stainless steel AISI 316L was selected among other stainless steel for moulds fabrication because it provides better overall corrosion resistance at high temperatures and does not generate precipitation of carbides, which are also undesirable because they can mark the glass surface. Further research would be necessary to investigate how strong is the adhesion of glass to this type of steel and how can be avoided or, if there are others materials that can substitute the AISI 316L in this application.

Another important finding in this study is that although the embedded particles found in the surface of the glass are of relatively small size to be detected by the naked eye, the effect is amplified by the deformed area (crater) around the mark caused by the viscous flow of the glass at high temperature. The typical size of this region is four to five times the size of the embedded particle. This feature makes noticeable the defect under normal quality inspections and possibly to the end users.

The surface of the glass at high temperature is more susceptible to damage by contact with the moulds, rollers or particles trapped between them. The use of experimental techniques such as instrumented indentation can help to measure the change in the response of the surface. The contact damage at forming temperatures is one of the many challenges in glass manufacturing and is a field insufficiently studied.

In subsequent sections, the surface damage in SLS glass is studied using Vickers and Hertzian indentation in a laboratory apparatus especially developed for this purpose.

### **5.3 Thermal analysis of Soda Lime Silica glass specimens.**

#### **5.3.1. Introduction**

The glass transition temperature of the Soda Lime Silica float glass specimens used in the high temperature indentation experiments was determined by means of Dilatometry and Differential Thermal Analysis (DTA). Standard procedures (ASTM E1545-11 and ASTM E1356, respectively) were used in the experiments and comparable results were obtained from both analyses.

#### **5.3.2. Dilatometry**

Dilatometry is an analytical tool where the linear expansion of a specimen is continuously measured with temperature. The dilatometer used was a push-rod type. In this device, the specimen is placed inside a fused silica tube that is enclosed in a cylindrical furnace. Two fused silica rods (probes) make contact with the specimen inside the tube on both sides. The end of one of the probes is in contact with a displacement sensor outside the furnace. The other probe is fixed outside the other end of the furnace. The expansion of the specimen displaces the movable probe and the total expansion is recorded as a function of time and temperature. The thermal expansion of the fused silica probes given its known thermal expansion coefficient is subtracted from the total displacement to obtain the specimen expansion.

### *Dilatometry experimental procedure*

A specimen of 35 mm x 5 mm x 2.3 mm of Soda Lime Silica float glass was cut from a larger slab. The edges were ground manually using 120, 400, 800 and 1200 grit size SiC papers followed by rotary polishing with 6 and 3  $\mu\text{m}$  diamond paste. The specimen was cleaned with isopropanol and lint-free towels. The dilatometer used was built in the Materials Characterization Laboratory of the University of Sheffield with operating characteristics that comply with the standard test procedure described in ASTM 1545-11. The furnace was pre-set to follow a  $5^\circ\text{C}/\text{min}$  heating from room temperature to  $610^\circ\text{C}$  where is expected to have passed the  $T_g$  for this type of glass. The device has a data acquisition system built with Labview (National Instruments Corp. UK. Ltd) and the data can be exported to a spreadsheet for further analysis.

### *Dilatometry Results*

The expansion obtained by the device is the sum of the expansion of the specimen and the fused silica probes. The expansion coefficient of the fused silica is  $5.5 \times 10^{-7} \text{ mm}/\text{mm } ^\circ\text{C}$  which is used to calculate and subtract the expansion of the probes from the total expansion. The expansion of the soda lime silica specimen is plotted in Figure 5.8, the procedure states that a regression line should be obtained from the low temperature thermal expansion curve. In this case, it was found that a better fit to the linear regression line was obtained in the temperature range of 200 to  $450^\circ\text{C}$ . Also it is required to obtain a regression line in the upper temperature section of the curve before the specimen undergoes major softening that changes the direction of the expansion curve. The regression line for this section was calculated in the range of  $560$  to  $580^\circ\text{C}$ . Both regression lines are extended and the intersection between them indicates the  $T_g$ , which for this type of glass the results was  $560^\circ\text{C}$  as can be seen indicated by an arrow in Figure 5.8. The linear expansion coefficient was calculated also from the experiments and the value obtained for the temperature range of 200 to  $450^\circ\text{C}$  was  $8.47 \times 10^{-6} \text{ mm}/\text{mm } ^\circ\text{C}$  which compares favourably with the value

reported in the literature for similar compositions of SLS float glass (LeBourhis 1998, NSG Bulletin 2013).

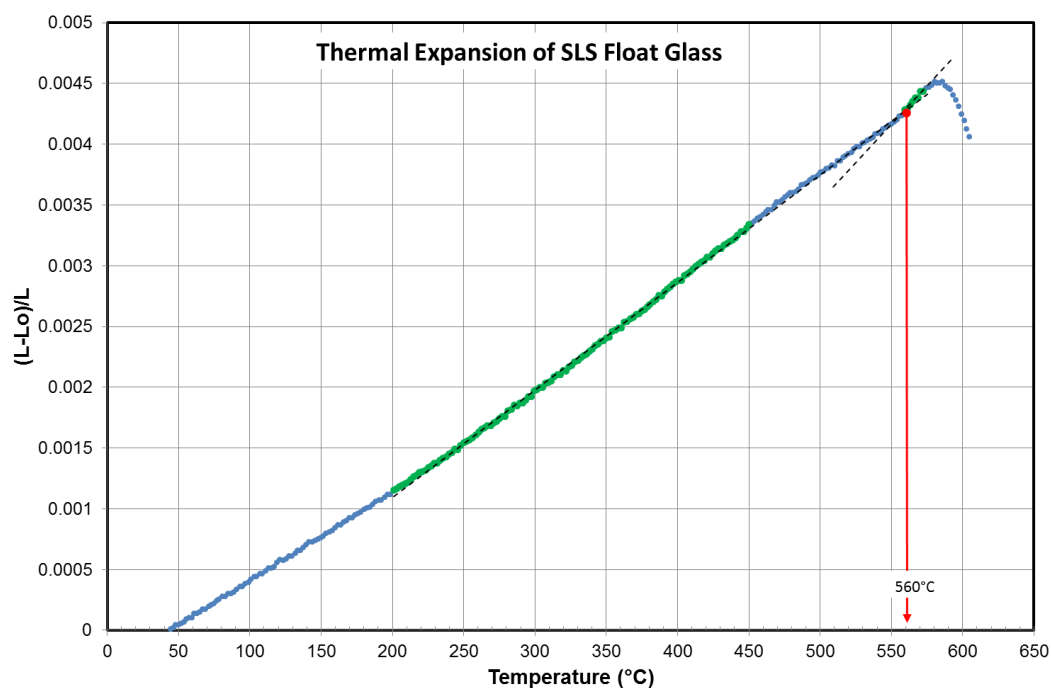


Figure 5.8: Dilatometry to determine  $T_g$  of SLS float glass used in the experiments of this work.  $T_g$  is the intersection of regression lines between low and high sections of the expansion curve.

### 5.3.3. Differential Thermal Analysis (DTA)

DTA is an analysis technique used to determine the temperature profile of the samples including endothermic or exothermic transitions, *i.e.* glass transition, crystallization, and melting temperatures. The apparatus used for DTA has two pans inside that are heated individually at the same heating rate. The sample is placed in one of them and the other is left empty or used with a reference material ( $\text{Al}_2\text{O}_3$  powder). During heating, if there is a thermal event in the specimen, there will be a difference in the temperatures of the sample and the reference because there is change in the heat capacity, or the latent heat that is produced is either lost or absorbed by the specimen. The output can be given as temperature difference ( $\Delta T$ ) or in heat flow (mW endo down) versus temperature ( $^{\circ}\text{C}$ ).

### *DTA experimental procedure*

A small amount of Soda Lime Silica float glass was ground using a mortar and a pestle until 25 mg mass of powder ( $< 75 \mu\text{m}$  size) was obtained. The apparatus used was a Thermo-gravimetric Analyser Pyrys1 TGA (Perkin Elmer Instruments, Norwalk CT, USA). The heating rate used was  $10^\circ\text{C}/\text{min}$  (ASTM E1356) with maximum temperature of  $1000^\circ\text{C}$  in air atmosphere.

### *DTA results.*

Although it is recommended to perform a heating and cooling cycle before obtaining the curve that is going to be analysed in order to remove the thermal history of the sample (ASTM E1356), it was decided to use the first heating curve in the  $T_g$  calculation by this technique since the specimens in the high temperature indentation experiments were used also in the “as received” condition. The results of the DTA in terms of heat flow versus temperature are plotted in Figure 5.9. The glass transition temperature in the data plot is indicated as an endothermic deflection or step in the curve before the material undergoes an incipient change in the absorbed heat due to transition to liquid state (Yamamoto 1965). It can be seen that the change that marks the  $T_g$  is not a single value of temperature but rather takes place over a temperature range. Therefore in the standard procedure (ASTM E1356) the  $T_g$  is calculated as the middle point between the extrapolated onset temperature and the extrapolated end temperature as it is shown in the inset of Figure 5.9.

The  $T_g$  value obtained by the DTA is  $565^\circ\text{C}$  which differs only slightly from that obtained with the method of dilatometry ( $560^\circ\text{C}$ ). An extensive search by Mazurin and Gankin (2008) into the published glass literature recognized differences in the  $T_g$  values obtained by both methods and proposed sample heating rates that attempt to produce consistent results. A heating rate of  $10^\circ\text{C}/\text{min}$  is proposed for DTA experiments and 3 to  $5^\circ\text{C}$  for dilatometry. These recommendations were used in the measurements and the differences found might be attributed to the experimental error which was not possible to assess with more readings due to the availability of the relevant equipment. The value of  $560^\circ\text{C}$  obtained by dilatometry was found to be

more close to the value of similar compositions used in the high temperature indentation work described in section 2.7.2.

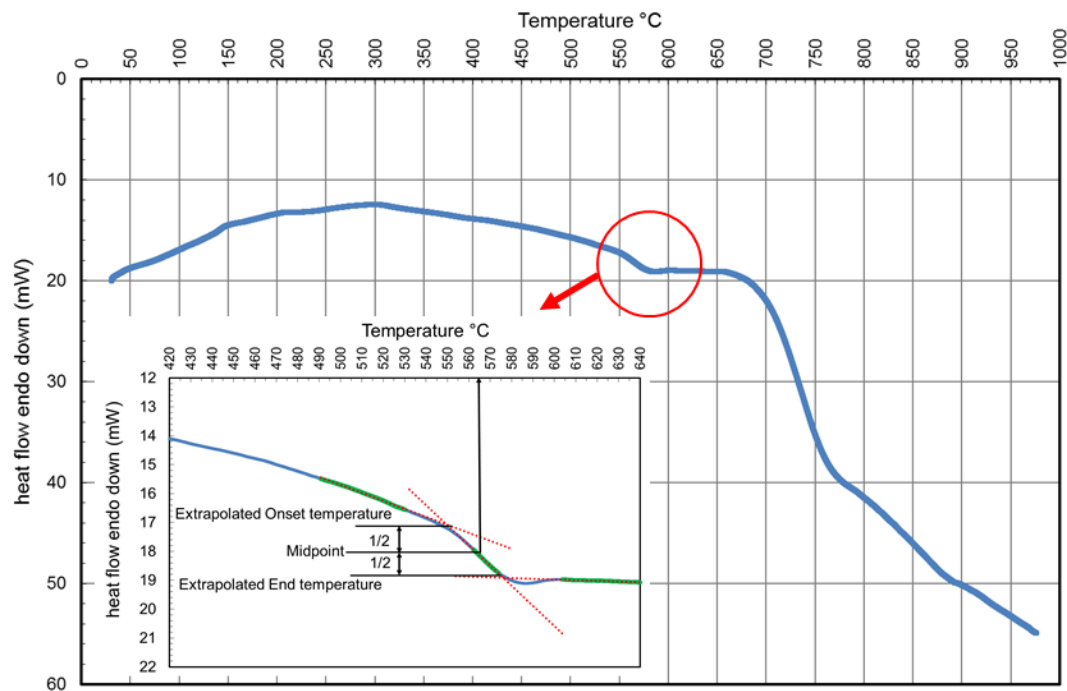


Figure 5.9: DTA of SLS float Glass.  $T_g$  of 565°C is obtained from the midpoint between the extrapolated onset temperature and the extrapolated end temperature as described in ASTM E1356 (inset).

## 5.4 Design of Experiments in high temperature indentation

### 5.4.1. Introduction

The indentation at high temperatures involves three main stages which are investigated in this section through a Design of Experiments. The first step during indentation is a loading ramp that starts with the contact of the indenter with the specimen surface and continues with the penetration of the indenter until the maximum load of the experiment is reached. The loading ramp can be at constant loading rate or constant speed rate. The second stage is hold or dwell time at the maximum load. In viscoelastic materials, the indenter will keep penetrating the surface during the set time trying to keep the load constant while the material is yielding underneath the indenter (creep). When the dwell time comes to an end, the unloading of the indenter begins (third stage) and, depending on the experiment conditions, it could be withdrawn at the same or a different speed to the loading speed.

### 5.4.2. Experimental procedure

The effect that the loading speed, dwell time and unloading speed has on the imprint size left by the indenter in the surface of a specimen of SLS float glass was investigated at a temperature of 560°C using a Vickers indenter and the apparatus described in Chapter 4. The glass specimens used were of the same composition and thickness of the one used in Chapter 3. In this case, all the experiments were carried out on the air side and a maximum load of 50 N. The DoE was a multilevel full factorial design with three replicates of each experiment. The levels of these three factors are described in Table 5.1. The response variable was the Vickers hardness obtained with equation 2.7 and the average size of the two diagonals of the imprint left by the indenter. The run order of the experiments was obtained using a statistical software (Minitab v16, Minitab Inc. 2014). Thirty six runs were specified in the design and the order of them was randomized. Seven specimens were used but all of them were cut from the same larger slab. The glass was used as received from the manufacturing plant and was only cleaned with isopropanol and lint-free towels after the air side was identified using a UV lamp.

*Table 5.1: Factors and Levels used in the DoE. Two levels were chosen for loading and unloading speeds and 3 for dwell time.*

<i>Factor</i>	<i>Levels</i>		
	<i>Min.</i>	<i>Centre Point</i>	<i>Max.</i>
<i>Loading Speed</i>	0.1 mm/min	---	1.0 mm/min
<i>Dwell time</i>	0 s	5 s	15 s
<i>Unloading Speed</i>	0.1 mm/min	---	1.0 mm/min

### 5.4.3. DoE Results

The results of the thirty six experiments were analysed using Minitab and the relevant statistics are shown in Table 5.2. The main statistic that describes and determines the statistical significance of the studied factors is the *p-value*. In hypothesis testing, *p-value* enables rejection or acceptance of the null hypothesis depending on the significance value set for the test (or  $\alpha$ -

level), typically 0.05. The  $p$ -value lies between 0 and 1 and if it is equal or less than the  $\alpha$ -level, the effect of the factor is statistically significant.

*Table 5.2:  $p$ -values for the studied factors and interaction between them. The  $R$ -Sq. of 97.89% indicates that the factors account for most of the variability of the experiment.*

Source	$p$ -value
Dwell time (DT)	0.000
Loading Speed (LS)	0.000
Unloading Speed (US)	0.004
<b>2-way Interactions</b>	
DT*LS	0.000
DT*US	0.005
LS*US	0.193

$R$ -Sq=97.89%

As can be observed in Table 5.2, the DoE results indicate that all the three factors are statistically significant as well as the interactions with the dwell time, but not the interaction between loading and unloading speed. Nevertheless, the graphical analysis of the effect of each factor can give a better idea of the importance of each one either when separate or when interacting with another factor.

The graphical output of the DoE includes the main effects plot shown in Figure 5.10. In this plot, the mean of the hardness is plotted against each factor's levels. The larger the difference of the response between levels, the more significant is this factor. The hardness decreases with the dwell time, while a slower loading speed also causes a lower hardness. Changing between a faster or slower unloading speed has almost negligible effect.

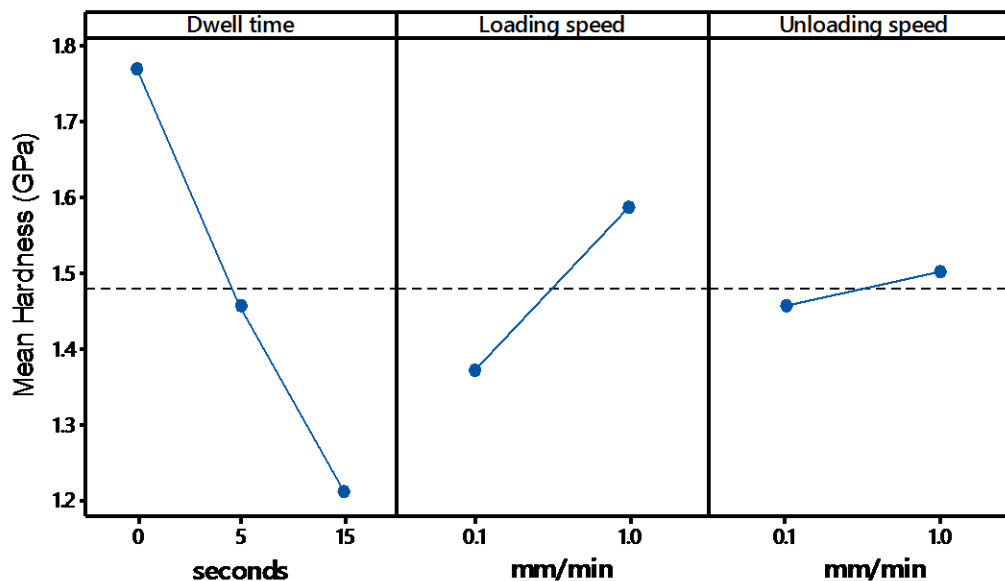


Figure 5.10: DoE Main effects plot. The mean of the hardness in GPa is plotted versus the levels of each factor. The Dwell time shows a larger effect in the hardness following by the Loading speed and a negligible effect of the unloading speed.

The interaction plot in Figure 5.11 helps to visualize the effect of combined factors. The two charts in the upper row of the plot indicate the interaction of the dwell time with the loading speed (top-centre) and with the unloading speed (top-right). It can be observed that with any dwell time, the loading speed has an effect on the measured hardness values. Slower loading speeds cause lower hardness, but with longer dwell times, the effect of the loading speed diminishes as can be observed by comparing the slopes of the three lines. The effect of the unloading speed is almost negligible, except with zero dwell time, where there is a little change in the hardness between the two speeds.

The interactions of the loading speed can be observed in the two charts in the mid row of the plot. There is a larger change in hardness between 0 and 15 s dwell time with the faster loading speed (centre-left). And there is almost a negligible relation with the unloading speed (centre-right).

The two charts in the bottom row of the plot describe the interactions of the unloading speed. The only observable effect of the unloading speed is with a dwell time of zero seconds (bottom-left).

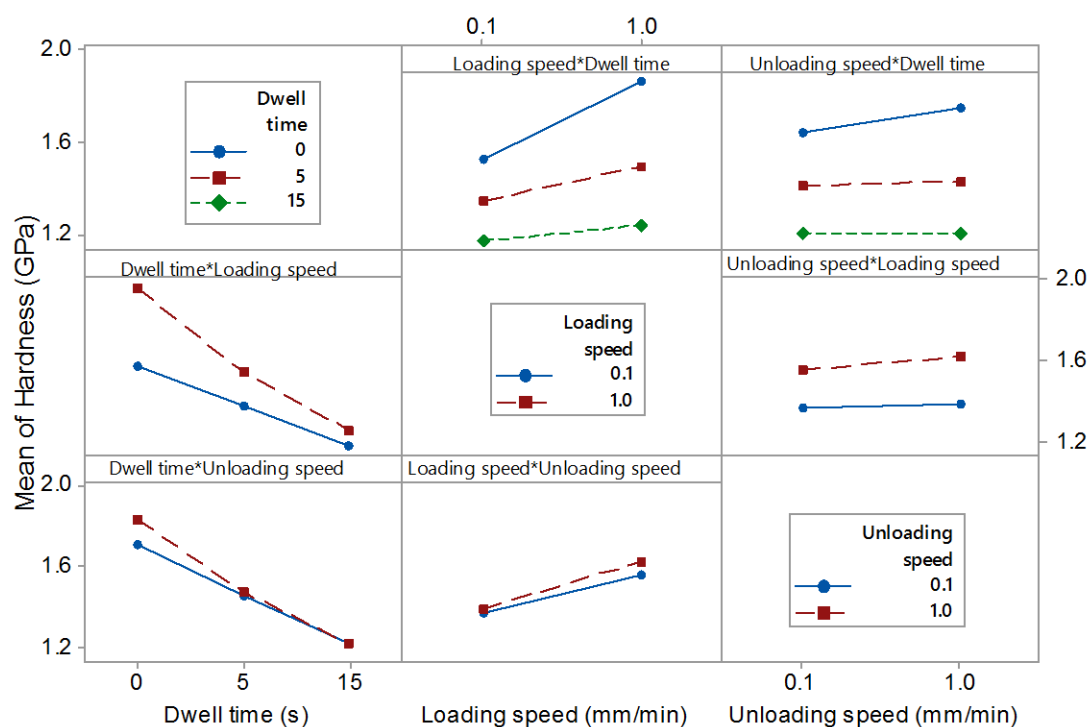


Figure 5.11: DoE Interaction Plot. The mean of the hardness (in GPa) can be read in the vertical axis of each chart. The factor and the levels are indicated in the horizontal axes.

The results of this DoE provide an insight into the influence of the stages of the indentation test on SLS float glass in the glass transition temperature. The three stages studied are not independent in the indentation experiment as they are sequential and the time that it takes to complete one stage has an influence on the next ones. This is because the glass is in the viscoelastic region and the material flows with time under the stress imposed by the penetration of the indenter.

The indentation with the lower loading speed of 0.1 mm/min takes 33.5 seconds to reach the maximum load of 50 N, this time is notably longer than the maximum dwell time of 15 s in these experiments, however during the loading, the indenter is penetrating progressively increasing the imprint size while the surrounding glass is flowing, but during the dwell time, the indenter keeps penetrating starting from a large imprint, and the fact that its effect is larger, means that the material creeps at a fast rate. In experiments with longer dwell times, is more likely that the effect of the dwell time diminishes once the material relaxes and the creep rate becomes lower. This can be observed in the change of slope of the hardness in the left chart of Figure

5.10. From 0 to 5 seconds the rate of change is larger than in going from 5 to 15 seconds.

In this study the unloading speed was not significant for the hardness because this was measured after the experiment finished and the glass was cold. But this could not be the case in an instrumented indentation test, were the material can be still flowing underneath the indenter and the shape of the unloading curve could be influenced by the unloading speed of the time of the previous stages as seen in viscoelastic materials such as polymers (Ngan and Tang 2002).

In conclusion, within the levels analysed, the dwell time will cause the largest change in measured hardness. Even though the change of loading speed levels is by a factor of 10 times, the change of few seconds in the dwell time is more important. The change in the unloading speed is not relevant when the hardness is assessed by imaging after the test.

## 5.5 Analysis methodology for instrumented indentation at room and high temperatures

### 5.5.1. Room temperature indentations

The load displacement data of the instrumented indentation experiments was analysed using the Oliver and Pharr method (Oliver and Pharr 1992) and the apparent hardness and elastic modulus were calculated. Although this analysis of instrumented indentation data has been explained in section 2.6.3, it is worthwhile to describe how the procedure was followed and how the equations were used.

The first step was to calculate the contact stiffness  $S$  from the unloading section of the load-displacement curve. As mentioned before, stiffness (equation 2.19) is the derivative of an equation that fits the unloading data evaluated at the maximum load  $P_{max}$ .

$$S = \frac{dP}{dh} \tag{5.1}$$

It was found that a second degree polynomial (equation 5.2) provided a good fitting of the upper part of the unloading curve, in this case, the best fit being found in the curve range from 47 to 35 N.

$$P = ah^2 + bh + c \quad 5.2$$

Once the stiffness was obtained, the contact depth  $h_c$  was calculated using equation 2.21 rearranged to the following form:

$$h_c = h_{\max} - \varepsilon \frac{P_{\max}}{dP/dh} \quad 5.3$$

Contact area  $A$  was calculated using equation , and then the reduced modulus  $E_r'$  and apparent hardness  $H'$  were calculated using equations 2.24 and 2.27 respectively.

The adjustment for the tip shape was applied in this part of the analysis using the expression 4.1 to obtain the corrected contact area  $A'$ . The reduced modulus and hardness were calculated again with the corrected contact area using the following expressions:

$$E_r' = E_r' \sqrt{\frac{A}{A'}} \quad 5.4$$

$$H = H' \left( \frac{A}{A'} \right) \quad 5.5$$

### 5.5.2. High temperature Vickers and Hertzian indentation

The viscoelasticity that the glass exhibits near the  $T_g$  requires a different analytical approach to be able to calculate the mechanical properties since the Oliver and Pharr method only works well with materials that exhibit elastic- plastic behaviour. The load-displacement curves of viscoelastic materials obtained by indentation generally present a bulge or “nose” in the unloading section affecting the calculation of the stiffness and therefore the rest of the properties.

Viscoelastic effects during indentation experiments has been observed in the nanoindentation of polymers and biomaterials where for some of them room temperature is close to their  $T_g$  so that they exhibit a strong viscoelastic

effect. (Ngan and Tang 2002, Odegard et al. 2005, Lu et al 2010, Fulcher et al 2010).

A common practice in the nanoindentation of viscoelastic materials has been the addition of a dwell or holding time at the maximum load with the purpose of allow the relaxation of the material and reduce the creep at the unloading stage.

In the reported studies on polymers it was found that although the “nose” had disappeared from the curve following such a dwell at load, the viscoelastic effects could still cause errors when calculating the elastic modulus. Two main corrections have to be applied to the contact equations to account for the viscoelasticity. First of all, the change in displacement due to creep during the dwell time ( $h_{creep}$ ) has to be subtracted from equation 5.3 obtaining the following expression (Geng et al, 2008):

$$h_c = (h_{max} - h_{creep}) - \varepsilon \frac{P_{max}}{S_e} \quad 5.6$$

And, secondly, the apparent stiffness  $S$  calculated from equations 5.1 and 5.2 can be broken down into elastic and creep terms to obtain the elastic contact stiffness  $S_e$ . Feng and Ngan (2002) proposed the following equation:

$$\frac{1}{S} = \frac{1}{S_e} + \frac{\dot{h}_v}{|\dot{P}|} \quad 5.7$$

where  $\dot{P}$  is the unloading rate and  $\dot{h}_v$  is the creep rate at the end of the dwell time.

After obtaining the contact depth  $h_c$  of the elastic contact, it is possible to calculate the contact area  $A_c$  and subsequently the hardness, which in this case as with the elastic-plastic contact at room temperature, will be the *apparent* hardness because it will differ from the Vickers hardness that is obtained from the measurement of the residual imprint on the surface. In the apparent hardness, the measured contact area includes the elastic deformation at maximum load. However, obtaining this parameter by the instrumented method, makes possible to observe the response of the surface

under different test conditions. Moreover, it is also known that the size of the imprint left by the indenter in the high temperature experiments can be influenced by the testing temperature or by the cooling/annealing time after the test is completed (Shang et al, 2006).

The plain strain modulus  $E'$  can be calculated with equation 2.24 and the relation in equation 5.8. This term will account for the elastic properties of the indenter and the specimen.

$$E' = \frac{E_r}{1 - \nu^2} \quad 5.8$$

Where  $\nu$  is the Poisson's ratio of the specimen, and according to Rouxel (2007), this property remains practically constant from room temperature up to  $T_g$ .

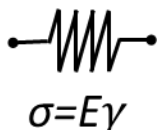
The dwell time at maximum load in the instrumented indentation experiments at high temperature allows also investigation of the response of the material to a constant stress, called creep. As can be observed in the load-displacement charts of the experiments near and at  $T_g$ , in the results section, the indenter undergoes a displacement while trying to keep the load constant. Important information is extracted from the creep experiments such as the instantaneous and the delayed elastic response as well as the flow in terms of time, which to some extent enables us to model the response of the surface to mechanical contact and forming processes.

Viscoelastic behaviour is generally investigated using mechanical models (Scherer 1986, Oyen and Cook 2003 and Fischer-Cripps 2004). The elements of these models are usually springs and dashpots that can be combined in different configurations to represent better the behaviour under certain circumstances.

The characteristics of the spring (Figure 5.12a) in the model is that they will compress or stretch (strain  $\gamma$ ) instantaneously under stress  $\sigma$  and will recover when this is removed obeying Hooke's law  $\sigma = E\gamma$  where  $E$  is the elastic modulus.

The dashpot (Figure 5.12b) is a plunger moving inside a cup with a liquid of a given viscosity  $\eta$  where the strain rate  $\dot{\gamma}$  will increase with the stress or with a decrease of viscosity and will not recover when the stress is removed. This element is represented by the expression  $\sigma = \eta \dot{\gamma}$ .

a)



b)

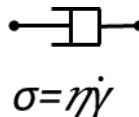
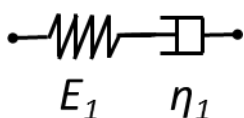


Figure 5.12: Basic mechanical elements used to represent viscoelastic behaviour. a) Spring where the stress is proportional to the strain and the elastic modulus and b) Dashpot, where the stress is proportional to the strain rate and the viscosity (Scherer 1986).

The Maxwell element (Figure 5.13a) is a combination of a spring with an elastic modulus  $E_1$  and a dashpot of viscosity  $\eta_1$  in series. With this configuration, both elements will experience the same stress but the strains will be different as the strain response of the spring is instantaneous and the dashpots responses with time. The Kelvin element (Figure 5.13b) is the spring and the dashpot arranged in parallel, in this model, the strain is the same but the stress is different.

a)



b)

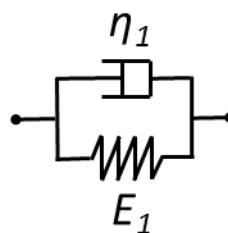


Figure 5.13: a) Maxwell element, spring and dashpot are arranged in series. b) Kelvin element, spring and dashpot are arranged in parallel.

More complex arrangements of the elements described previously are required to model the creep of real materials. According to the theory of viscoelasticity, the creep component has three elements that can be identified in a typical curve (Figure 5.14): an instantaneous elastic strain at the beginning of the curve, secondly, a reversible delayed elastic strain where the creep rate is very high, and finally irreversible strain by viscous flow where the creep rate reaches a constant slope (Scherer 1986). A

combination of a Maxwell and a Kelvin (Figure 5.15) element is used to model the behaviour of creep.

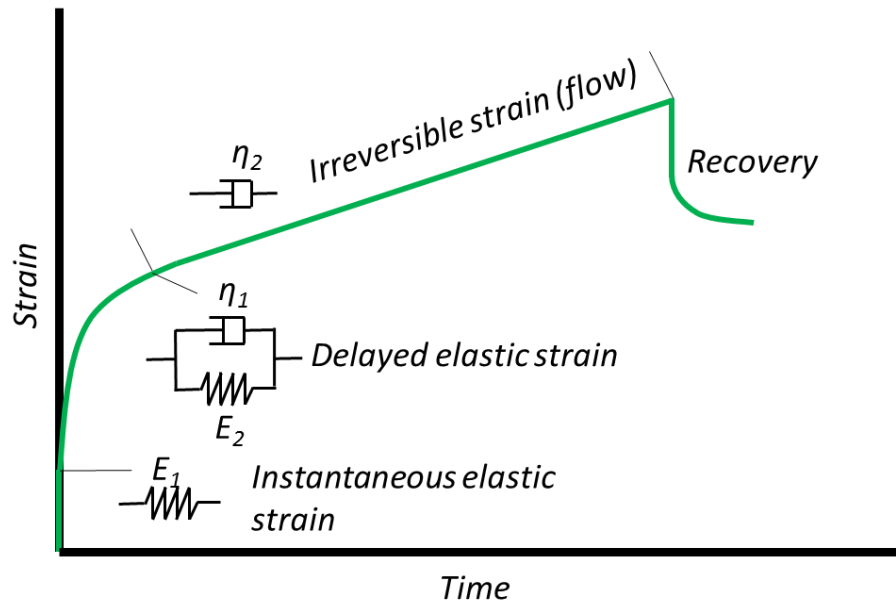


Figure 5.14: Stages describing creep of viscoelastic materials

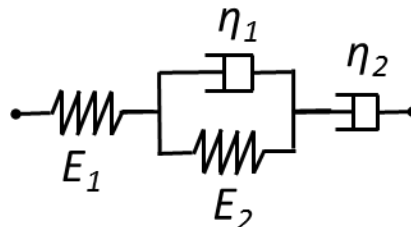


Figure 5.15: Four element model, Maxwell + Kelvin

The analysis of indentation in viscoelastic materials is based on the substitution of the elastic solution with viscoelastic operators (Lee and Radok 1960). The assumptions considered for the analysis are that the shear modulus  $G$  is time-dependent, the bulk modulus is time-independent and the material has a Newtonian behaviour (linear viscoelasticity).

Oxide glasses are generally considered to have linear viscoelastic behaviour (Scherer 1986). This means that viscosity does not change with

stress and the instantaneous and delayed elastic responses are linearly proportional to the stress applied. It might be thought that indentation, especially with sharp indenters, can induce very high stresses. However, at elevated temperatures in the viscoelastic region, a low stress deformation is more likely to occur as is evidenced by the large area around the imprint affected by the viscous flow of the material (Bernard et al 2010).

As mentioned previously, analytical solutions for elastic contact of indenters are used as a starting point for the viscoelastic analysis. Equations 5.9 and 5.10 describe the displacement  $h$  for Hertzian and pyramidal indenters respectively in an elastic medium (Johnson 1985):

$$h^{3/2} = \frac{3}{4\sqrt{R}} P \frac{(1-\nu^2)}{E} = \frac{3}{8\sqrt{R}} \left[ \frac{P}{2G} \right] \quad 5.9$$

where  $P$  is the load,  $R$  is the indenter radius.

$$h^2 = \frac{2\gamma^2}{\pi \tan \varphi} P \frac{(1-\nu^2)}{E} = \frac{\gamma^2}{\pi \tan \varphi} \left[ \frac{P}{2G} \right] \quad 5.10$$

in which  $\varphi$  is the indenter equivalent cone angle ( $70.3^\circ$  for Vickers) and  $\gamma$  is a constant that relates the contact displacement with the total displacement. In both equations, the shear modulus  $G$  is being substituted for the plain strain modulus  $E' = E/(1-\nu^2)$  assuming  $\nu=0.5$  such that  $E' = 4G$ .

In the previous equations,  $[P/2G]$  can be replaced by the memory integral of the creep compliance function  $J(t)$ , which will give:

$$\frac{P}{2G} = \int_0^t J(t-u) \frac{dP}{du} du \quad 5.11$$

where  $u$  is the dummy variable for integration of time  $t$ . The creep compliance function  $J(t)$  is a basic characteristic of the material that expresses the time course of the response during a step unit load.

For an instantaneously applied load  $P_0$ , the solution of the previous integral is:

$$\frac{P}{2G} = P_0 J(t) \quad 5.12$$

Nevertheless, in the indentation experiments there is a loading ramp before reaching the maximum load  $P$ , for this case, the integral in 5.11 will be (Oyen 2006):

$$\frac{P}{2G} = k \int_0^t J(t-u) \frac{dP}{du} du \quad 5.13$$

where  $k$  is the loading rate  $dP/dt$ .

The solution for the loading ramp integral is based on the viscoelastic model for a spring in series with a Kelvin element (spring and dashpot in parallel). Therefore the creep function takes the form of:

$$J(t) = C_0 - \sum_{j=1}^n C_j \exp\left(\frac{-t}{\tau_j}\right) \quad 5.14$$

where  $C_0$  and  $C_j$  are compliance constants,  $\tau_j$  is the retardation time is equal to the product of the compliance of the spring  $C_j$  and the viscosity of the dashpot  $\eta_j$  that is in parallel with the spring ( $\tau_j = \eta_j C_j$ ) (Menčík et al 2009, 2011).

The solution for a constant rate loading would be:

$$\frac{P}{2G} = C_0 kt - \sum C_j k \tau_j \left[ 1 - \exp\left(\frac{-t}{\tau_j}\right) \right], \quad 0 \leq t \leq t_R \quad 5.15$$

The time that takes for the load to increase from 0 to  $P_{\max}$  is  $t_R$ . If the load is kept constant after the load ramp for a period of time to allow creep (dwell time), the integral that describes that condition ( $t_R$  to  $t_R + t_{dwell}$ ) is:

$$\frac{P}{2G} = k \int_0^{t_R} J(t-u) \frac{dP}{du} du \quad 5.16$$

which can be solved using expression 5.13 to obtain:

$$\frac{P}{2G} = C_0 kt_R - \sum C_j k \tau_j \exp\left(\frac{-t}{\tau_j}\right) \left[ \exp\left(\frac{t_R}{\tau_j}\right) - 1 \right], \quad t \geq t_R \quad 5.17$$

Equation 5.17 can be substituted and rearranged in equations 5.9 and 5.10 to obtain the displacement of the indenter (Hertzian or Vickers) for the viscoelastic condition. However, is pertinent to review a couple of corrections that need to be included to improve the accuracy of the model. The first

correction is related to the time that is taken to reach the  $P_{max}$ . In the viscoelastic analysis of indentation it is desirable to have a fast loading ramp to minimize the viscoelastic effects during that time, however this is not always possible. Oyen (2005) introduced a ramp correction factor that accounts for the difference between step loading and ramp loading which is applied to the exponential terms in equation 5.17

$$\rho_j = \left( \frac{\tau_j}{t_R} \right) \left[ \exp \left( \frac{t_R}{\tau_j} \right) - 1 \right] \quad 5.18$$

One additional element that is necessary to add to the viscoelastic model is the term for the irreversible plastic deformation that is expected in the glass near the glass transition temperature caused by the viscous flow (second dashpot in Figure 5.14). This deformation is time-dependent and is characterized by the viscosity  $\eta_v$  of the dashpot in the Maxwell element. The creep compliance function of this dashpot is:

$$J(t) = C_v t \quad 5.19$$

where the constant  $C_v$  is related to the dynamic viscosity as  $C_v = 1/\eta_v$ .

For the ramp period at constant loading rate for a time  $t_R$ , the response function for the dashpot is:

$$C_v \left( t - \frac{t_R}{2} \right) \quad 5.20$$

in which the term  $t_R/2$  indicates the fact that the indenter penetration during the loading ramp for the period  $t_R$  corresponds to the average load  $P/2$ .

Time-independent deformation occurs also by effect of the concentrated load and is called instantaneous. It is contained in the compliance constant  $C_0$  along with the instantaneous elastic response  $E_0$ .

The equations for Hertzian and Vickers indenters for creep derived from the viscoelastic model (equation 5.17) considering the corrections for the loading ramp and for the time-dependent deformation are (Menčík et al 2009, 2011):

For a Hertzian indenter:

$$h^{3/2}(t) = \frac{3}{8\sqrt{R}} P \left[ B + C_v t - \sum D_j \exp\left(\frac{-t}{\tau_j}\right) \right] \quad 5.21$$

And for a Vickers indenter:

$$h^2(t) = \frac{\pi}{4 \tan 70.3^\circ} P \left[ B + C_v t - \sum D_j \exp\left(\frac{-t}{\tau_j}\right) \right] \quad 5.22$$

where B is a constant that groups the constants that do not depend on time:

$$B = C_0 - C_v \frac{t_R}{2} + \sum C_j \quad 5.23$$

and

$$D_j = C_j \rho_j \quad 5.24$$

Now that the equations for the viscoelastic analysis are derived, the following procedure was used to determine the principal constants:

1. Calculation of the regression constants  $B, C_v, D_j$  and  $\tau_j$  by fitting equations 5.21 or 5.22 to the creep data.
2. Calculate the ramp correction factor  $\rho_j$  with the duration of the loading ramp  $t_R$  and the retardation times  $\tau_j$ . Then find the constants  $C_j$  using equation 5.24
3. Determine  $C_0$  from equation 5.23

## 5.6 Experiments at high and room temperature

### 5.6.1. Sample preparation

Soda Lime Silica float glass specimens 3.27 mm thick and of the same composition described in Chapter 3 were cut to 40 mm x 40 mm squares from a larger slab. The edges were ground manually using silicon carbide papers with 240 to 800 grit sizes. Tin and air sides were carefully identified using the UV lamp and a chamfer was made in one corner of the specimen on the tin surface to leave a permanent identification mark. The surfaces were finally cleaned with isopropanol and lint-free towels.

### **5.6.2. Experimental procedure room temperature indentation**

The specimens were indented with the Vickers diamond tip at the room temperature of  $22 \pm 1^\circ\text{C}$  using the same apparatus and set up as used for the high temperature experiments. The maximum load used was 50 N with a loading and unloading speed of 0.1 mm/min and no dwell time. The separation between indents was at least 5 mm to allow enough room between them for crack propagation. At least ten indentations were carried out on both tin and air sides of two different specimens obtained from the same larger slab.

Optical surface profilometry (3D Optical Profilometer Contour GT, Bruker Corp.) was used to inspect the imprints of the room and high temperature indentations. This analytical technique allowed us to obtain a profile of the indentation where size and depth can be measured. A 3-Dimensional image was also obtained to help visualize the characteristics of the residual mark on the surface. Optical microscopy (Nikon Eclipse LV150, Japan) along with the imaging and measuring software was also used to measure the residual imprint diagonals required to calculate the Vickers Hardness  $H_V$  using the equation 2.7.

### **5.6.3. Experimental procedure high temperature indentation.**

The design of the testing apparatus allows the furnace to be opened, so that the specimen can be placed on the stage along with the thermocouples. With the furnace still in the open position, the indenter is moved towards the specimen surface using the manual displacement control of the testing machine to a distance of 15  $\mu\text{m}$  which is calibrated using feeler gauge. Depending on the experiment temperature, an additional gap has to be set between the specimen surface and the indenter tip to allow for the thermal expansion of the indenter column and the stage during the heating cycle. In the case of a testing temperature of  $520^\circ\text{C}$ , this gap was calculated from the known thermal expansion coefficients and subsequently adjusted to 2.3 mm. For the testing temperature of  $540^\circ\text{C}$ , the gap set was 2.4 mm, and 2.6 mm for  $560^\circ\text{C}$ .

Before closing the furnace, a thermocouple was placed in contact with the glass surface and a second one was placed in contact with the indenter column. These two readings provided an indication of when thermal equilibrium was reached and also allowed monitoring of the temperature during the test.

The furnace was set to follow an automated ramp for heating and cooling cycles as depicted in Figure 5.16. The hold time at the testing temperature can be adjusted depending on the experiment duration.

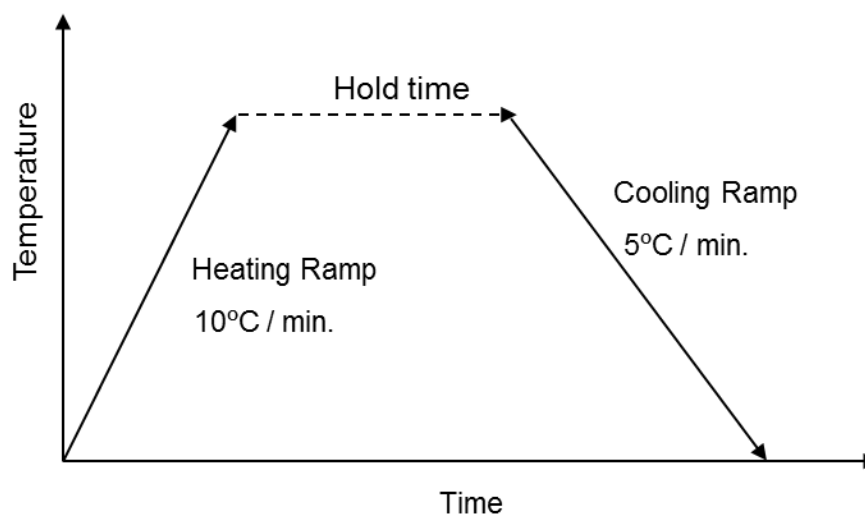


*Figure 5.16: Furnace cycle for indentation experiments*

Once the maximum testing temperature was reached, a hold time of one hour was allowed before the start of the testing for the specimen, indenter and furnace chamber to reach thermal equilibrium. Otherwise, thermal expansion during the test would lead to an error of the true displacement of the indenter.

The indenter movement followed an automated cycle programmed in the control software of the testing machine. Before each experiment, the parameters were set and the test initiated. At the same time, the data acquisition system started logging the displacement, load, time and temperature readings that were exported subsequently to a spreadsheet for analysis.

For the experiments reported in this section, the testing conditions are described in Table 5.3. At least ten indentations were made for each set of conditions.

After each indentation, the platform was unlocked from its base and rotated to the next position so that a new indentation could be made in the same specimen. All six indentations in the same specimen were done at the same temperature. However, other parameters such as dwell time, load, or speed could be changed between indentations.

*Table 5.3 Experimental parameters for Vickers indentation at high temperatures.*

<b>Parameters</b>	<b>Values</b>
Maximum Load (N)	• 50
Loading speed (mm/min)	• 0.1
Unloading speed (mm/min)	• 0.1
	• 0
	• 30
Dwell time (sec)	• 60
	• 90
	• 120
	• 150
	• 22
Temperature (°C)	• 520
	• 560

A maximum load of 50 N was selected for all of the experiments, since this allowed a penetration depth that minimized the measurement error of the displacement sensor. It was found experimentally that in this apparatus, the loading and unloading speed of 0.1 mm/min permitted enough data to be acquired and recorded by the data acquisition system which has a limitation of 16 readings per second. To investigate the viscoelastic regime, a fast loading and unloading speed is desirable to minimize the viscous effects during the loading and unloading ramp as we will discuss in section 5.6.4. Creep behaviour was studied with different dwell times at maximum load in intervals of 30 s until 150 s. Four experimental temperatures were selected: room temperature to investigate the elastic-plastic contact; and 520, 540 and 560°C to study in the viscous-elastic-plastic regime near and at the glass transition temperature. It was not possible with our current set up to

investigate at higher temperatures since there was a tendency of the indenter to adhere to the specimen affecting the curves during the unloading section.

#### 5.6.4. Results

##### *Vickers indentation at room temperature*

Figure 5.17 depicts an example of a curve of a Vickers indentation experiment at room temperature which has been already adjusted for machine compliance. The data points in the curve show some noise originated from the slight mismatch between the data acquisition rate of the displacement sensor and the load cell. However, the good amount of data points obtained allows the analysis of the curve and makes the effect of this noise negligible.

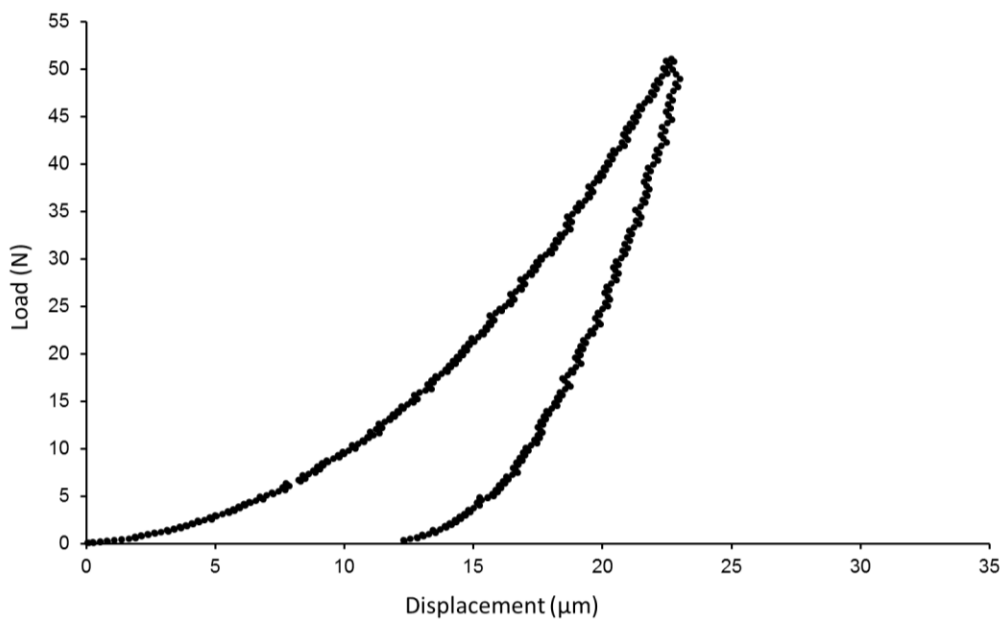


Figure 5.17: Load-Displacement curve of an indentation experiment in SLS glass

Table 5.4 shows the reduced modulus and apparent hardness calculated from the experiments for the tin and air sides of SLS float glass. The values are expressed in terms of the mean of the 10 experiments  $\pm 1$  standard error. The results are in agreement with those published in the literature for this type of glass which are between 5.4 and 6.6 GPa for hardness (as mentioned in section 2.6.2) and 71.3 GPa for the reduced modulus. The latter is obtained using equation 2.2, considering elastic moduli of 1141 GPa and 72

GPa and Poisson ratios of 0.07 and 0.23 for the diamond indenter and the specimen respectively.

*Table 5.4: Reduced modulus and hardness of SLS glass obtained by instrumented macro-indentation. Values are expressed as the mean  $\pm$  1 standard error.*

Surface	Reduced modulus (GPa)	Apparent hardness (GPa)
Tin side	73.1 $\pm$ 0.9	5.48 $\pm$ 0.03
Air side	69.0 $\pm$ 2.9	5.20 $\pm$ 0.2

A 3D image of one of the indents is shown in Figure 5.18. Radial cracks can be observed as expected and sub-surface lateral cracks may have propagated without detaching yet material around the indentation. The colour scale provides evidence of shear flow in the form of pile-up around the imprint.

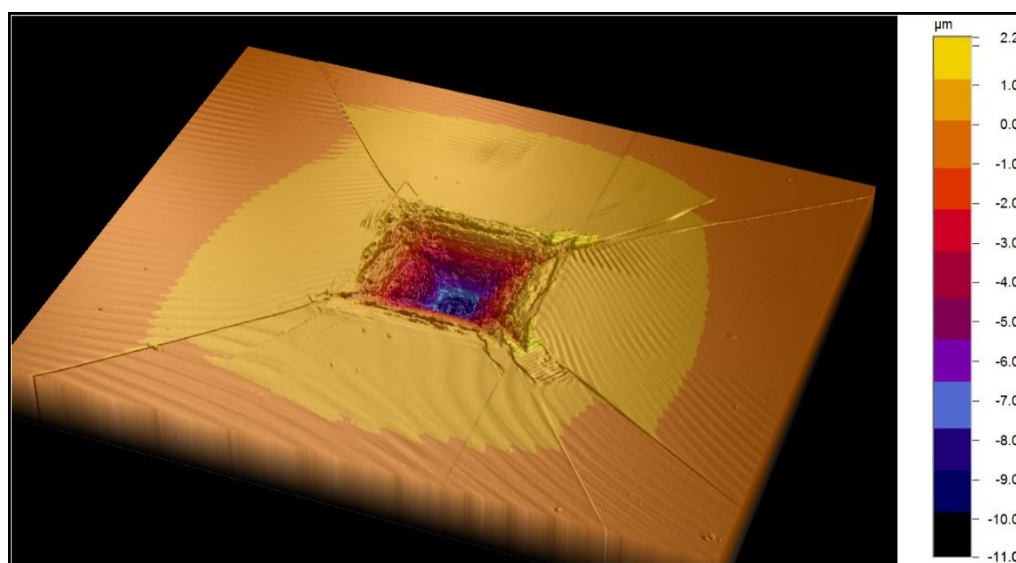


*Figure 5.18: 3D image of a Vickers indentation at room temperature in SLS glass*

A surface profile across two parallel sides of the indentation was obtained, to reveal the size and extension of the pile-up (Figure 5.19), for the maximum load of 50 N, the pile-up reaches an average height of 1  $\mu$ m and extends over 75  $\mu$ m from the edge of the imprint. Previous papers that have reported the deformation mechanisms under Vickers indentation in Soda Lime Silica glass have indicated that both pile-up and densification under the indentation at room temperature are present. Pile-up has been reported to be load

independent where the ratio of pile-up area in relation to indentation area is about 2.2 (Chiang et al, 1982). On the other hand, densification ratio increases with load as reported by Yoshida et al (2007).

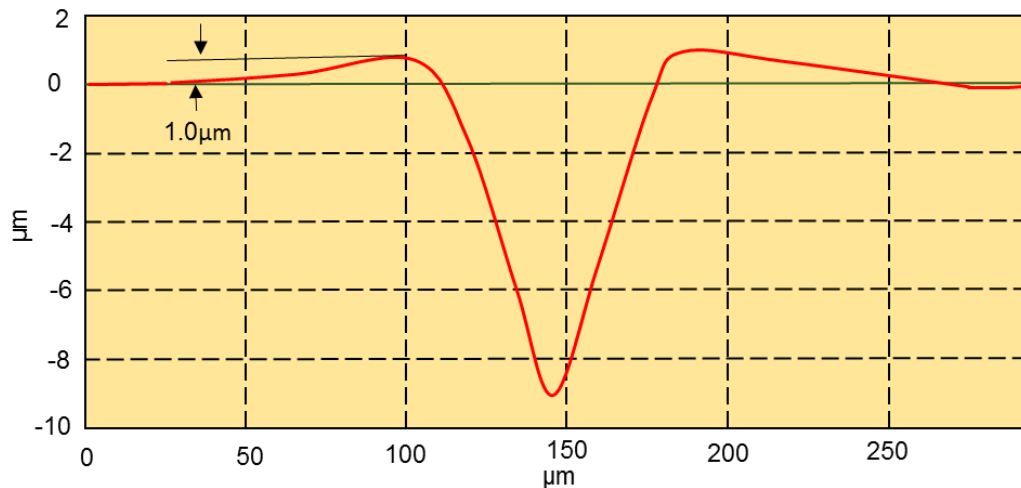


Figure 5.19: Profile of a Vickers indentation at room temperature

#### *Indentation experiments at elevated temperatures*

In the last section, room temperature indentation curves were obtained and it was observed a purely elastic behaviour during the unloading stage, where, at the drop of the load, an immediate reduction in the displacement occurred. Nevertheless, in the high temperature indentation experiments, a different behaviour was observed while using the same testing parameters of the experiments at room temperature as can be observed in Figure 5.20.

The first observation from this chart is that with the increasing temperature, it takes more time and displacement for the indenter to reach the maximum load. The second remark and most important is that at the beginning of the unloading stage, there still seems to be some downward displacement of the indenter for a short period of time creating a bulge or “nose” in the upper part of the curve.

These effects observed in the indentation at elevated temperatures are caused because the viscous state starts to dominate as the temperature increases in the material. The creep of the material underneath the indenter makes difficult to build-up the force during loading and causes the indenter to

keep displacing downwards at the onset of the unloading despite the fact that the load has started to reduce, generating the “nose”.

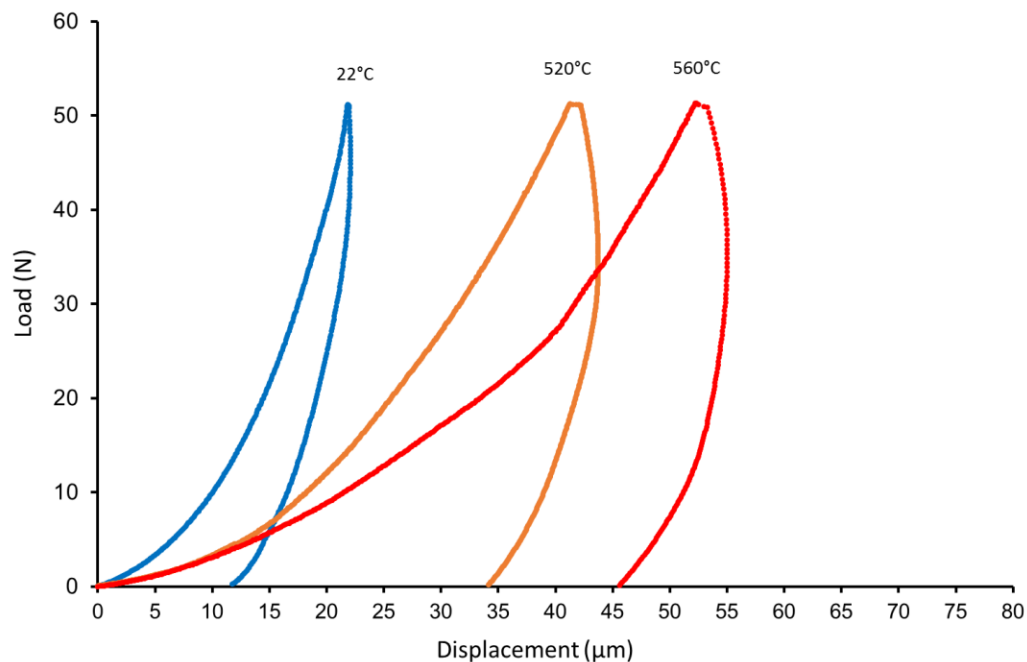


*Figure 5.20: Effect of the testing temperature in the load-displacement curve of a Vickers indentation.*

Adding a dwell time in the testing routine has an effect on the shape of the unloading curve. Figure 5.21 shows the upper part of the curves of three experiments at 560°C with different dwell times at maximum load. It can be observed how effectively the nose is reduced or even eliminated with longer dwell times.

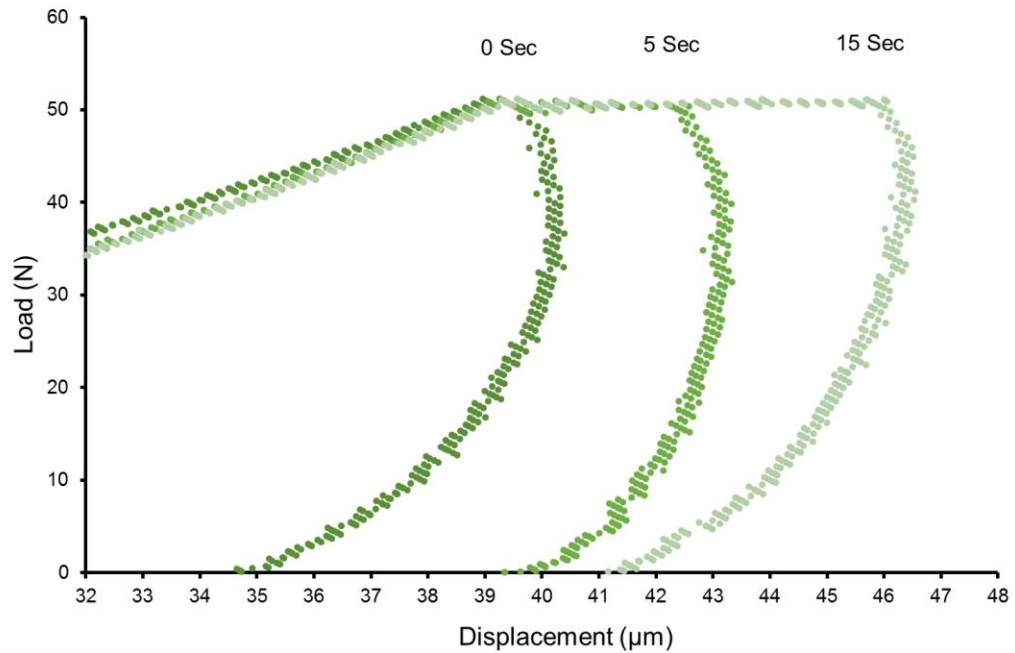


Figure 5.21: Effect of Dwell time in the shape of the unloading section of the curve.

#### *Apparent hardness and plain strain modulus*

In Figure 5.22 the apparent hardness is plotted against dwell time at 560°C for the tin and air side. At this temperature there was a significant creep at the dwell time and in congruence we observe a tendency of the hardness to decrease with time. As in the experiments at room temperature, we observe also a slight difference in hardness between both sides of the float glass, with the tin side being harder.

The hardness at 560°C was also measured by imaging the diagonal of the residual imprint and the results are plotted in Figure 5.23. The hardness of the tin side is higher than the air side but overall the hardness values are smaller than those obtained by the analysis of the curves. This difference obeys not only to the elastic deformation at the maximum load, but also to the pile-up and sink-in effects in the imprints.

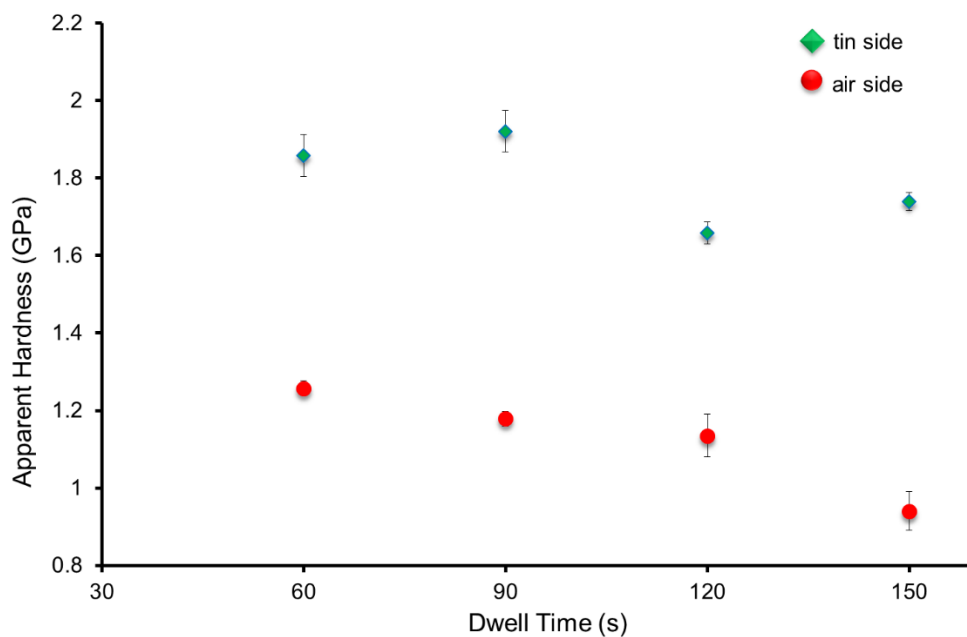


Figure 5.22: Apparent Vickers hardness as a function of dwell time for SLS at 560°C on tin and air sides. Error bars are  $\pm 1$  std. error from the mean.

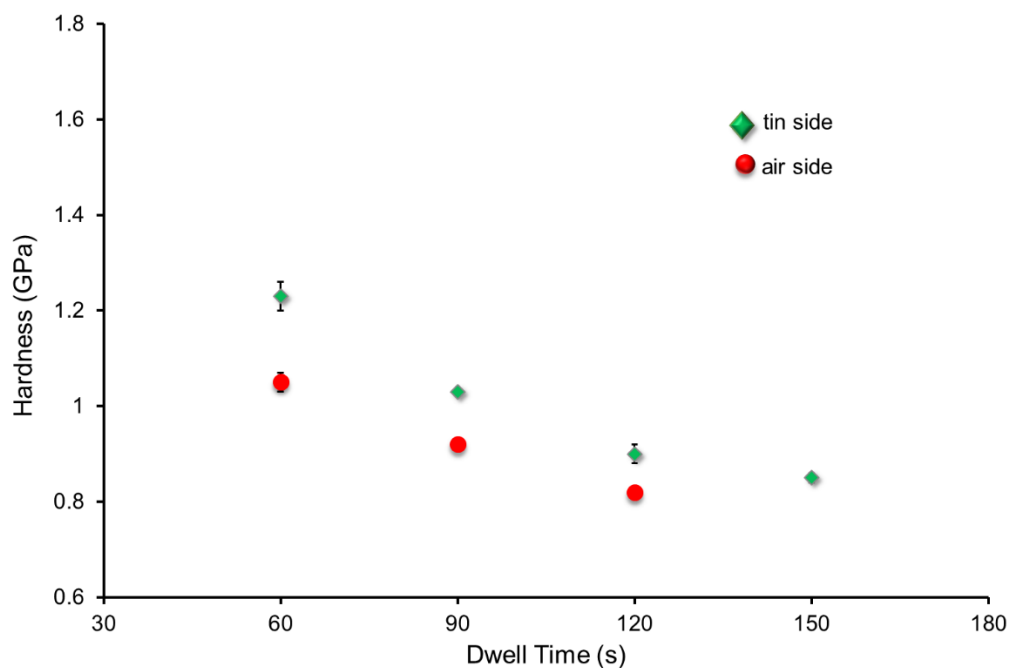
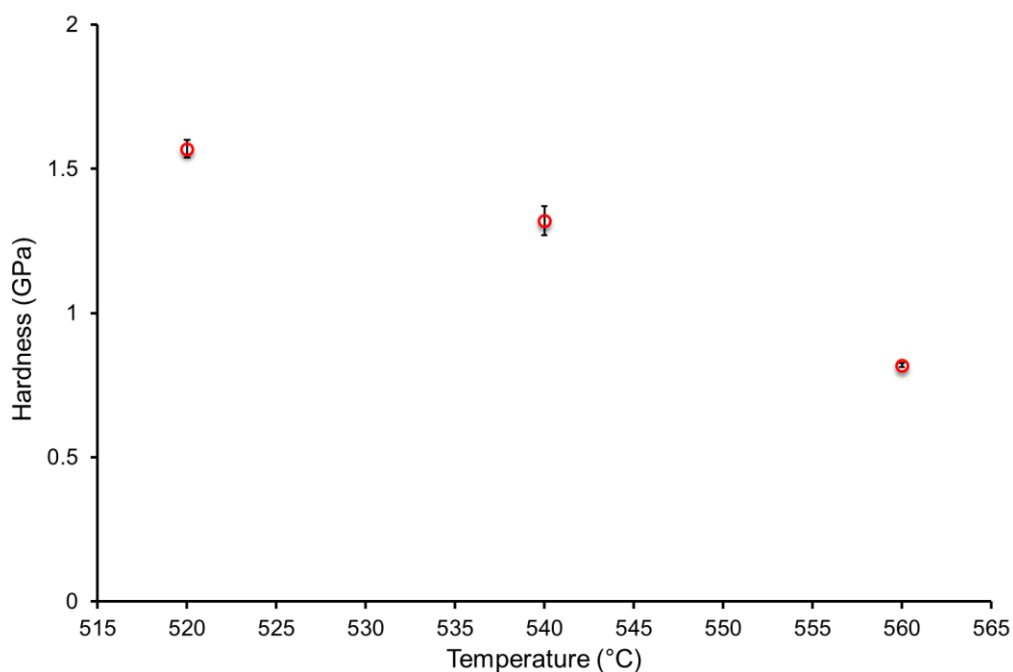


Figure 5.23: Vickers hardness as a function of dwell time for 560°C obtained by imaging of the residual imprint. Error bars are  $\pm 1$  std. error in the mean.

In Figure 5.24 the hardness is plotted as a function of temperature. It can be observed how the hardness decreases as the viscoelastic effect becomes more relevant with temperature. In this case, the data plotted in the chart was

obtained from experiments with 120 s of dwell time at maximum load, which favours even greater penetration of the indenter due to the extensive time allowed for creep.

A clearer image of the effect of temperature and dwell time in the hardness can be observed in Figure 5.25 where the hardness as a function of dwell time is plotted for each one of temperatures studied. It can be inferred from the chart how the rate of change of hardness maintains a linear relation with the dwell time but not with temperature especially when approaching  $T_g$ .



*Figure 5.24: Vickers hardness obtained by imaging the air side as a function of temperature. Dwell time of these experiments was 120s. Error bars are  $\pm 1$  std. error in the mean.*

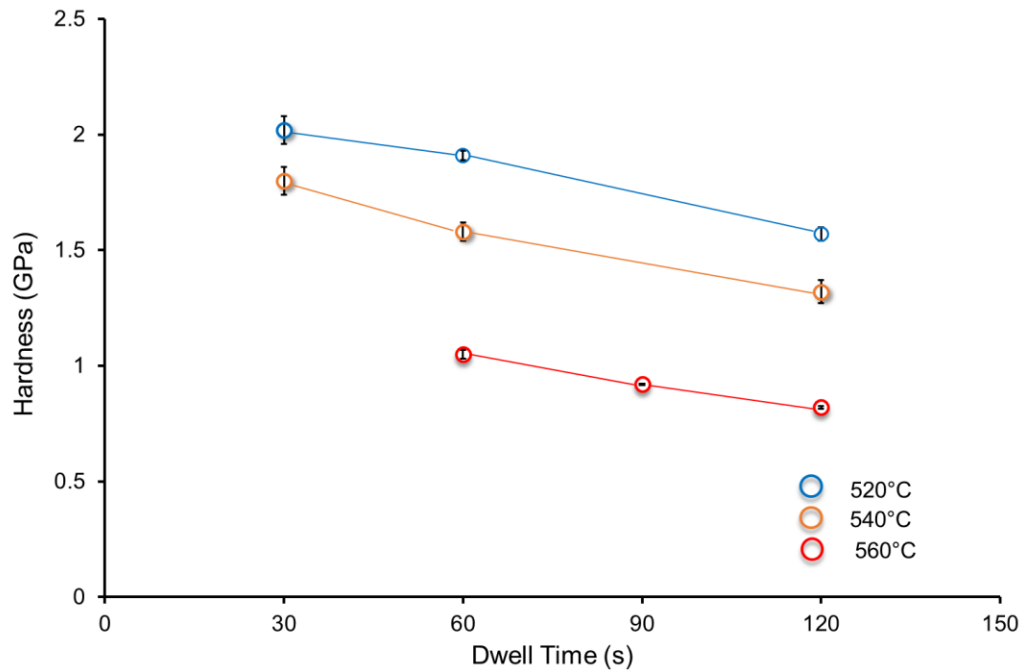


Figure 5.25: Air side hardness as a function of dwell time for the three experimental temperatures. Error bars are  $\pm 1$  std. error in the mean.

Plain strain modulus is plotted as a function of dwell time for both tin and air sides at 560°C in Figure 5.26. It can be observed from this figure how the plain strain modulus approaches a value of 65 GPa with longest dwell times. Measurements of the elastic constants for SLS float glass as a function of temperature by optic and acoustic methods have been performed previously. Duffrène et al (1998) and Rouxel (2007) reported values of 62 GPa and 0.22 for elastic modulus and Poisson's ratio respectively in the temperature range of 550 to 600°C from which we can obtain a plain strain value of 65.1 GPa using equation 5.8.

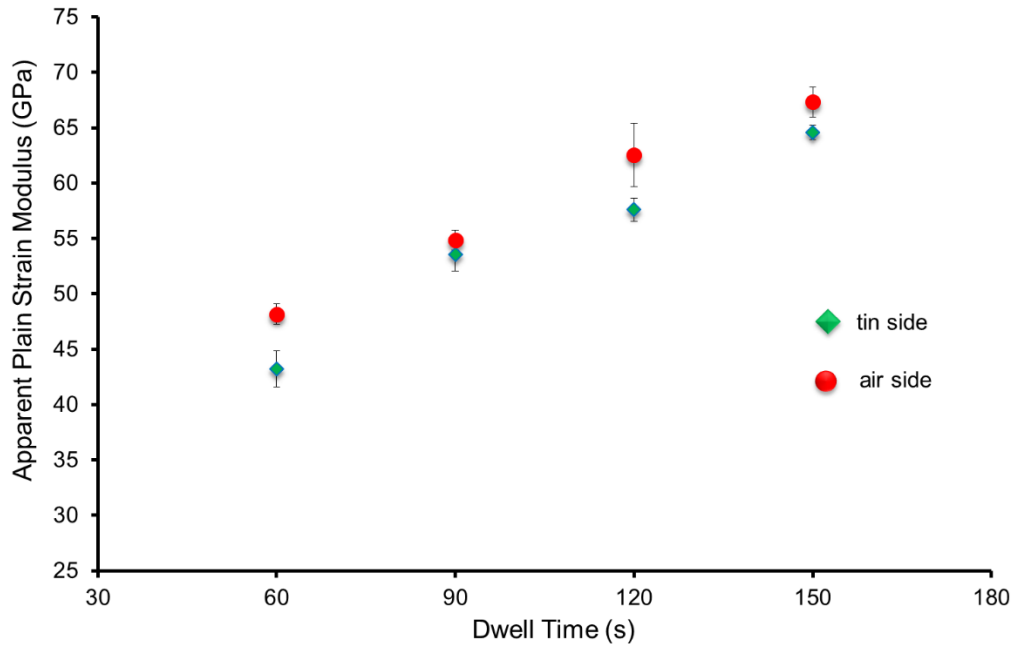


Figure 5.26: Measured apparent plain strain modulus as function of dwell time at 560°C for tin and air sides.

Similar behaviour is observed at the testing temperatures of 520 and 540°C as can be seen in Figure 5.27, although a shorter dwell time is required to eliminate the viscous effect and reach the expected modulus value which, for these temperatures, is close to 70 GPa.

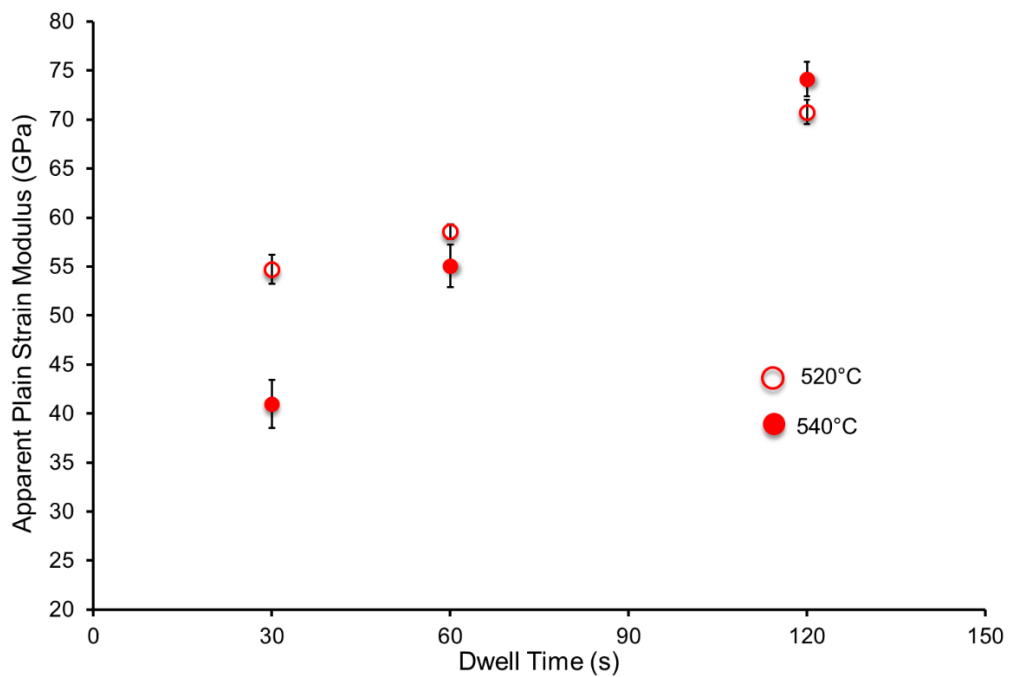


Figure 5.27: Apparent plain strain modulus as a function of dwell time for 520 and 540°C

Optical profilometry of the imprints of indentations at high temperatures reveals a distinctive behaviour between the indents at different temperatures. While the imprints at 520°C (Figure 5.28) still retain a clear footprint of the pyramidal indenter (similar to the indentations at room temperature), the imprint made at  $T_g$  (560°C) shows a shape that more closely resembles that produced by a conical indenter (Figure 5.29). It is important to remark that some indentations made at 560°C with a short dwell time (i.e. 30 s) still preserve the shape of the pyramidal indenter in the imprint, however, with larger dwell times (120 s) as in the case of the Figure 5.29, the material had enough time to flow and resettle around the indenter smoothing the sharp corners of the remained shape due to the lower viscosity.

#### *Analysis of the imprints*

Another interesting feature between the imprints in Figure 5.28 and Figure 5.29 is the pile-up around the indentation. Whilst at 520°C it can be observed that the pile-up formed next to the parallel sides of the square indent, in the 560°C indentations, the pile-up is more defined in a circumferential zone which encircles the indent.

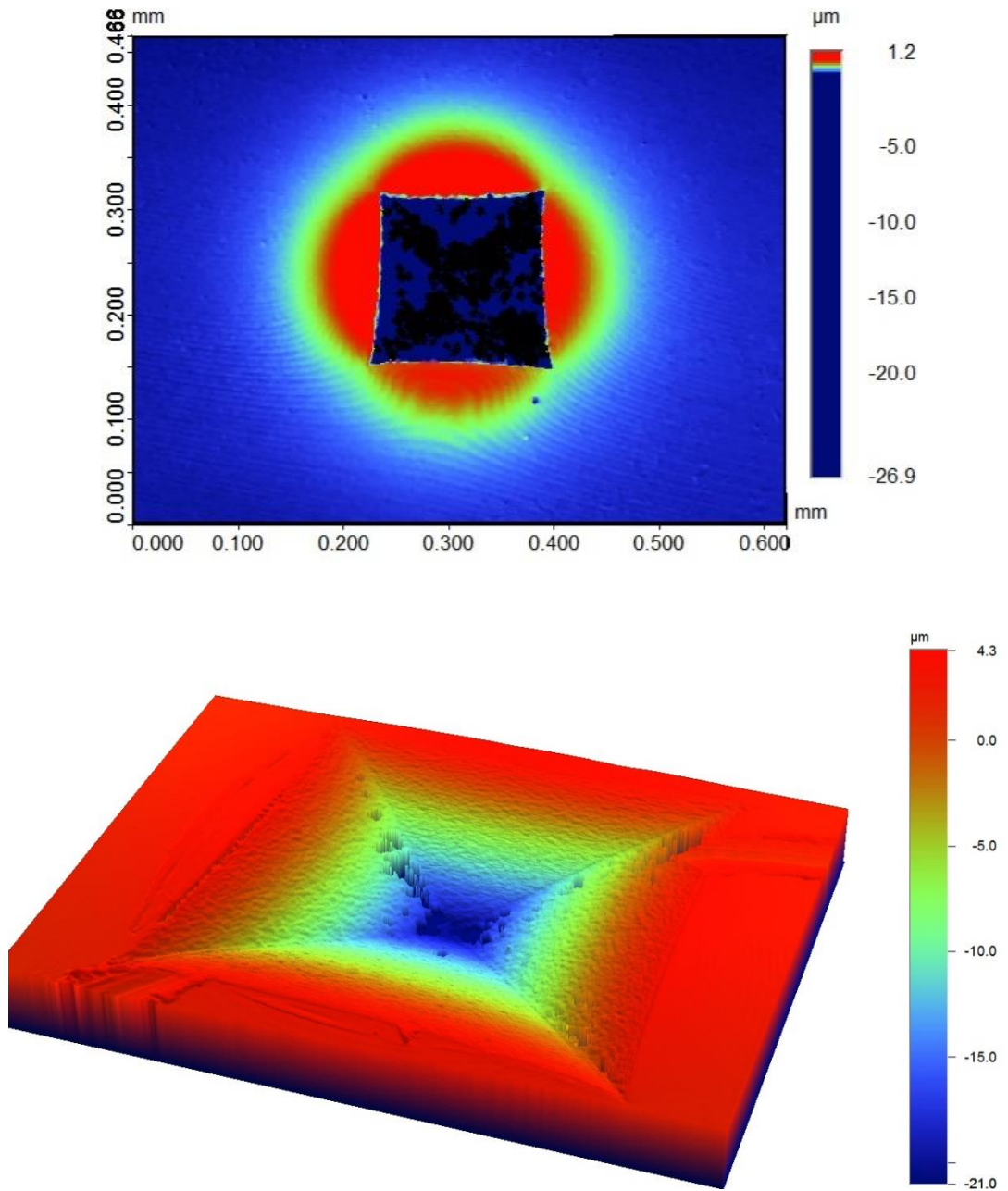


Figure 5.28: Optical profilometry of an indentation imprint at 520°C and 120 s. dwell time

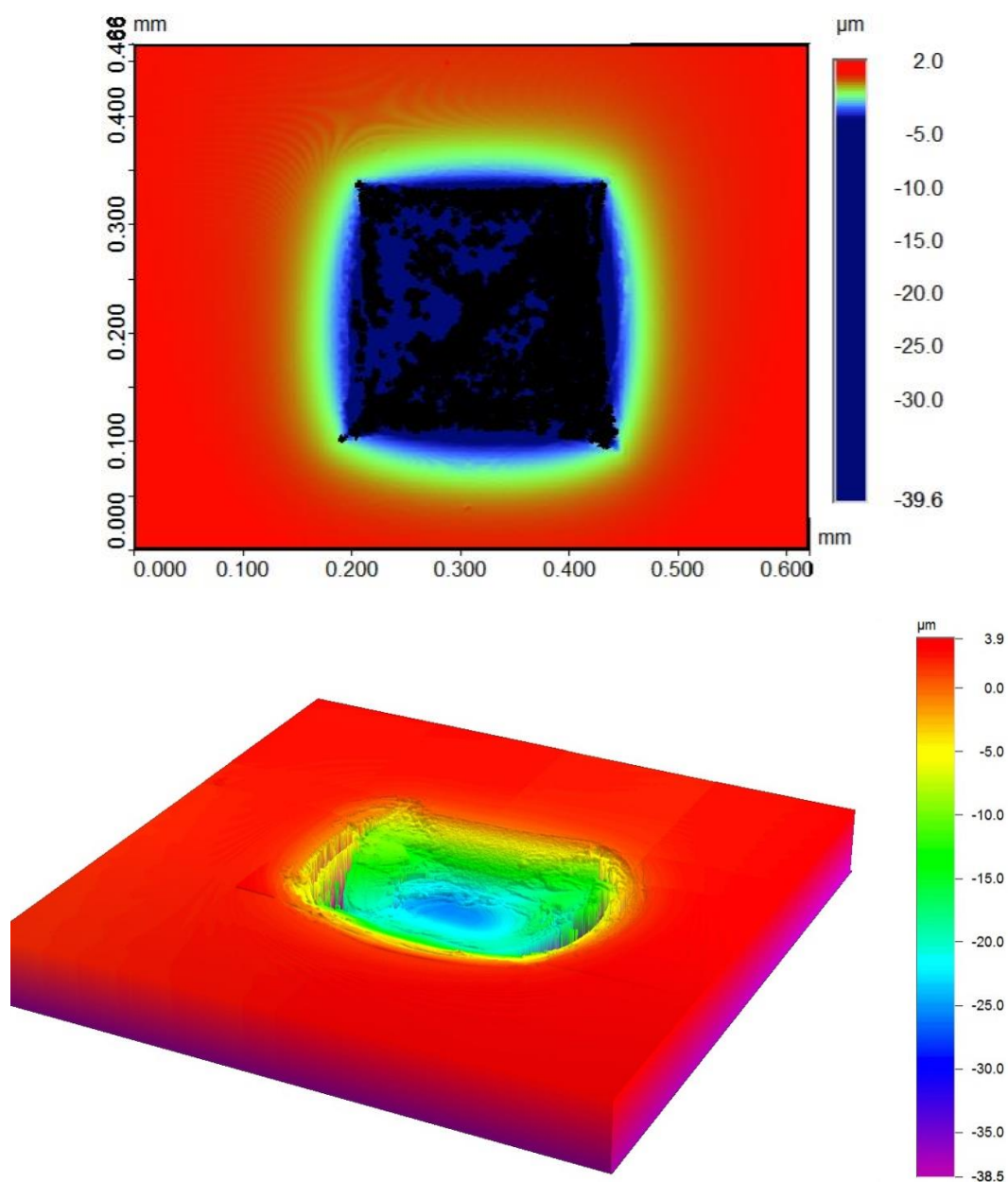


Figure 5.29: Optical profilometry of an indentation imprint at 560°C and 120 sec dwell time

The profile of the surface across the imprints crossing two of the parallel sides of the indentations at the four temperatures investigated is shown in Figure 5.30. The volume displaced in the form of pile-up at each temperature can be observed. This volume increases not only in height but, more extensively in length as the temperature approaches  $T_g$ .

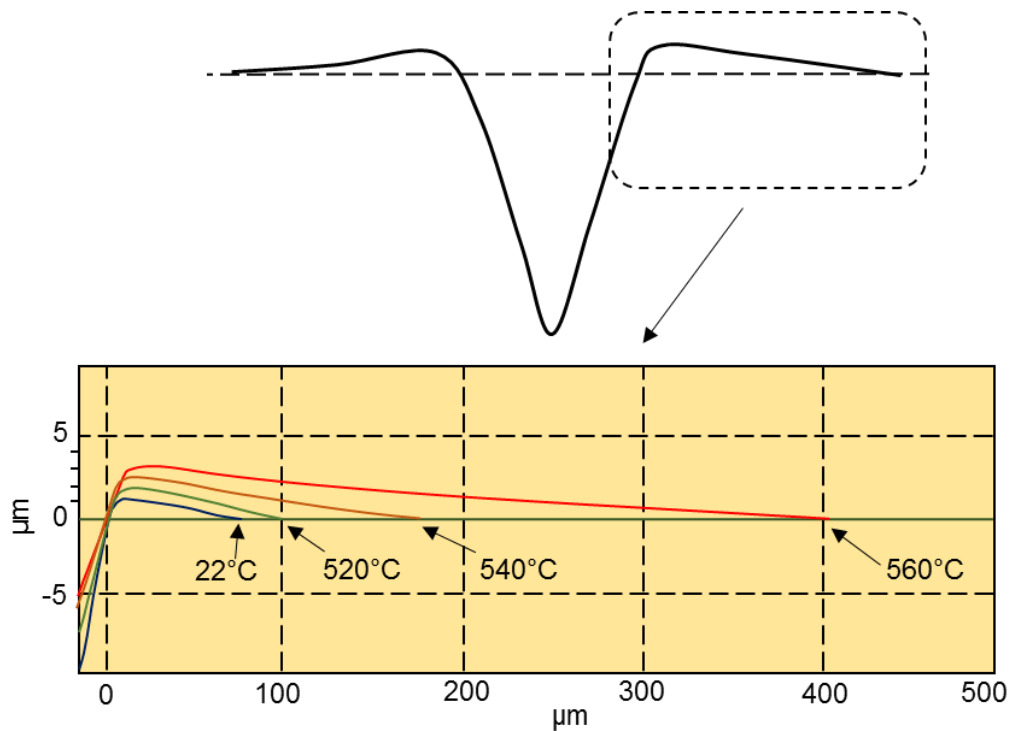
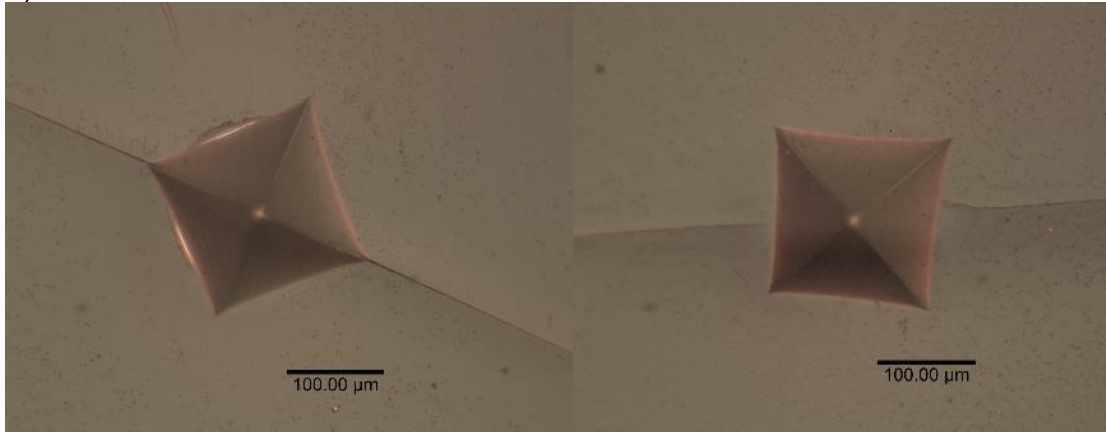


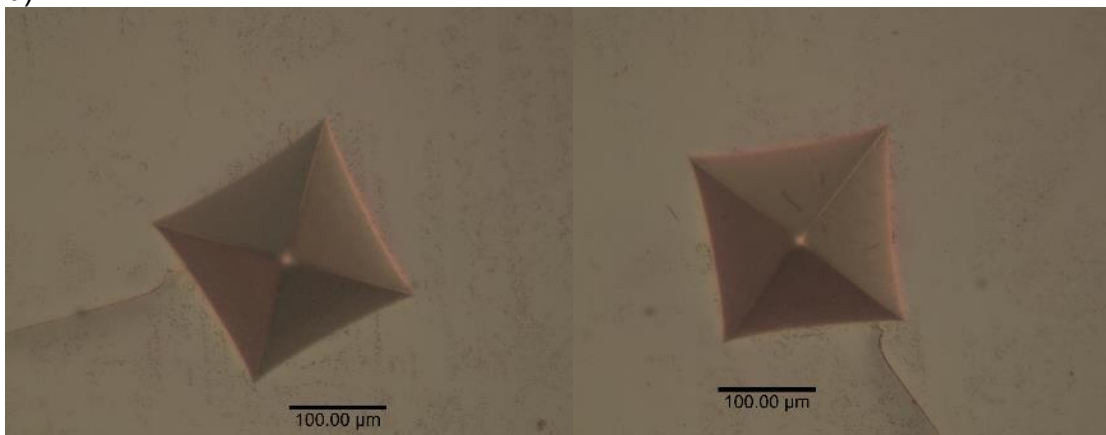
Figure 5.30: Profilometry of the cross-section of indentations at 22, 520, 540 and 560°C showing the pile-up extent

Examining the indentation imprints under the optical microscope (Nikon Eclipse Mod.LV150, Japan), it can be observed from Figure 5.31 that in most of the indents at 520°C, a pair of radial cracks appear in the direction of the diagonals and sometimes start adjacent to the sides of the indentation, but still in radial direction to the centre of this. Lateral cracks were observed also in a couple of the ten indents of this experiment. Once again, it is important to mention that the cracking behaviour observed from the surface (radial cracking) does not necessarily reflect what might be happening in the sub-surface (median cracking). At 540°C the incidence of cracking is less and usually only one crack was found. No cracks were detected in the indentations at 560°C. This same pattern of crack formation with temperature on SLS glass has been reported previously (Kese et al, 2008) indicating how the increasing viscoelastic behaviour with temperature prevents the generation of cracks.

a)



b)



c)

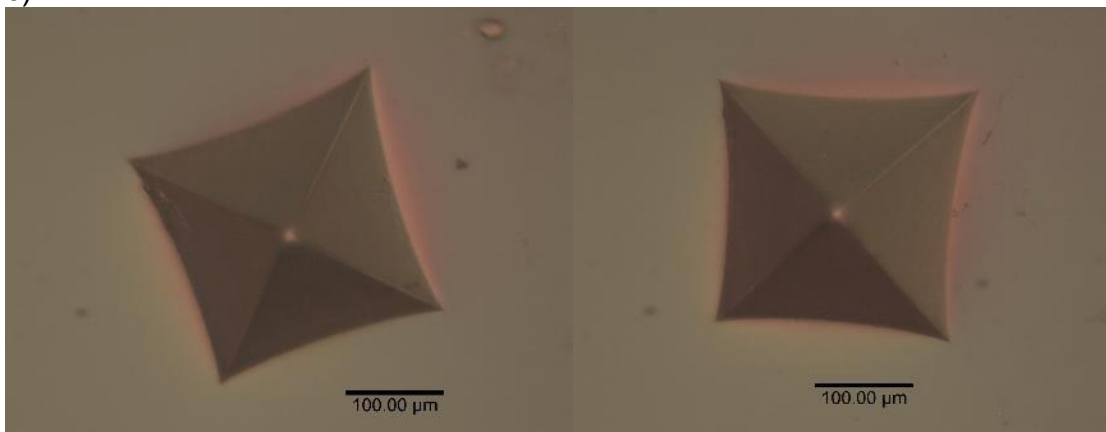


Figure 5.31: Micrographs of indentations at a) 520°C, b) 540°C and c) 560°C with a dwell time of 60 s.

#### *Analysis of creep curves*

The viscoelastic model represented by equations 5.21 and 5.22 was fitted to the creep data of indentation tests that were carried out under different experimental parameters. A computer program (Matlab v2013, Matworks Inc)

was used to perform the fitting and the constants and main statistical parameters were obtained for each set of data by applying a non-linear regression with the least-squares fitting method. The software was set to perform the iterations using the Levenberg-Marquardt algorithm (Mathworks Documentation 2013) which requires entering starting estimated values of the parameters in order to arrive at a solution which is reached when negligible improvement to the fitting occurs (convergence).

The quality of the fitting was evaluated graphically observing the residuals plot and assessing the Goodness-of-fit statistics. In the residuals plot, the value of “ $h$ ” is replaced by the distance of each data value to the fitting curve. A random scatter of these values (positives and negatives) is an indication that the model provides a good fit. Large clusters of data either negative or positive mean that the model does not fit the data well.

The software calculates the Root Mean Square Error (RMSE), which measures the difference between the predicted and the observed values. The R-square is also calculated and is the square of the correlation between the data values and the fitted curve. A value close to one indicates that the model explains better the variation of the data about the mean. The adjusted R-square is also a statistic that is an indicator of the fit quality and is particularly helpful to compare the ability of two nested models to fit the data. A nested model means that the equation is basically the same for both, but one model has more parameters than the other.

The creep data of Vickers indentation experiments obtained at 520°C and 120s dwell time was fitted using three viscoelastic models as described below:

- Maxwell + 1 Kelvin Element
- Maxwell + 2 Kelvin Elements
- Maxwell + 3 Kelvin Elements

Such models are respectively expressed in the following equations obtained by adding the Kelvin elements to equation 5.22:

$$h^2(t) = \frac{\pi}{4 \tan 70.3^\circ} P \left[ B + C_v t - D_1 \exp\left(\frac{-t}{\tau_1}\right) \right] \quad 5.25$$

$$h^2(t) = \frac{\pi}{4 \tan 70.3^\circ} P \left[ B + C_v t - D_1 \exp\left(\frac{-t}{\tau_1}\right) - D_2 \exp\left(\frac{-t}{\tau_2}\right) \right] \quad 5.26$$

$$h^2(t) = \frac{\pi}{4 \tan 70.3^\circ} P \left[ B + C_v t - D_1 \exp\left(\frac{-t}{\tau_1}\right) - D_2 \exp\left(\frac{-t}{\tau_2}\right) - D_3 \exp\left(\frac{-t}{\tau_3}\right) \right] \quad 5.27$$

Increasing the Kelvin elements increases the number of constants required for the model. All three models provide a good fit as indicated by the R-sqr in Table 5.5. The difference in the fitting quality between the Maxwell + 1 Kelvin element and Maxwell +2 and 3 elements is negligible.

*Table 5.5: Fitting results (scaled h Vs. time) for Maxwell + 1, 2 and 3 Kelvin elements of a Vickers indentation test at 520°C and 120s dwell time*

<b>Model</b>	<b>R-sqr</b>
Maxwell + 1 Kelvin	0.9751
Maxwell + 2 Kelvin	0.9752
Maxwell + 3 Kelvin	0.9752

The simplest (fewest constants) model that provides the best fit is the Maxwell + 1 Kelvin element model. The constants calculated for this model according to equations 5.22 and 5.23 are shown in Table 5.6. The fitting was also evaluated graphically by plotting the  $h^2$  versus time as depicted in Figure 5.32. The residuals plot in the inset of the figure confirms that there is an acceptable fit to the data.

*Table 5.6: Fitting constants for Maxwell +1 Kelvin elements according to equations 5.22 and 5.23. Vickers indentation test at 520°C and 120s dwell time*

<b>Model</b>	<b>C<sub>0</sub></b>	<b>C<sub>1</sub></b>	<b>C<sub>v</sub></b>	<b>τ<sub>1</sub>(s)</b>
Maxwell+1 Kelvin	0.335	0.211	0.01	22.3

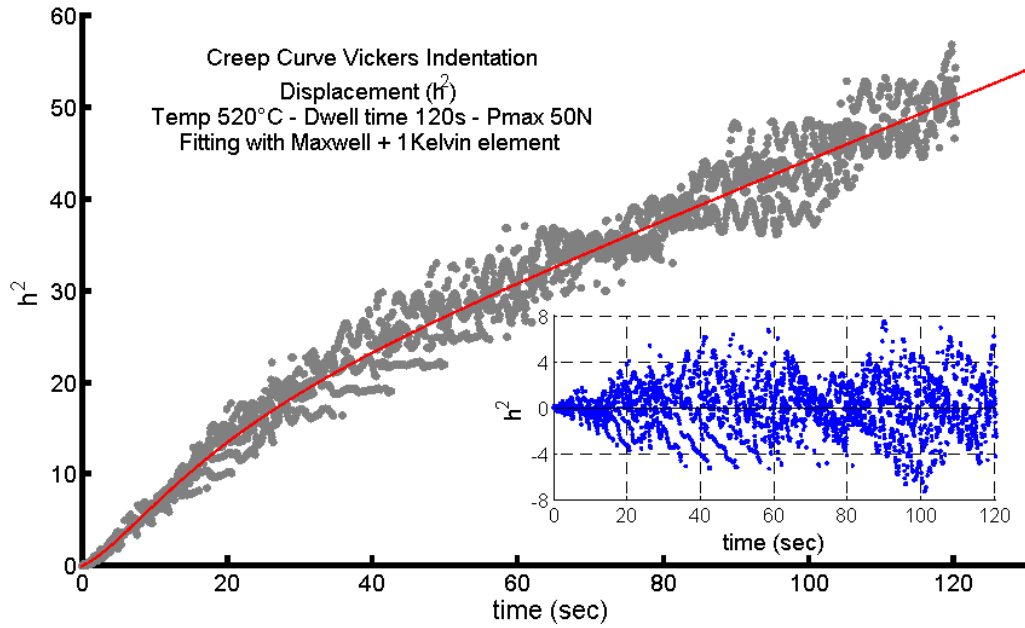


Figure 5.32: Creep data for Vickers indentation at 520°C. The red line is the fitting curve of the Maxwell + 1 Kelvin element model and the residuals are displayed in the inset.

The model was then plotted using the constants and transforming  $h^2$  to  $h$ . The fitting curve obtained is plotted along with the creep data in Figure 5.33. It can be observed that the model approximates very well the creep data.

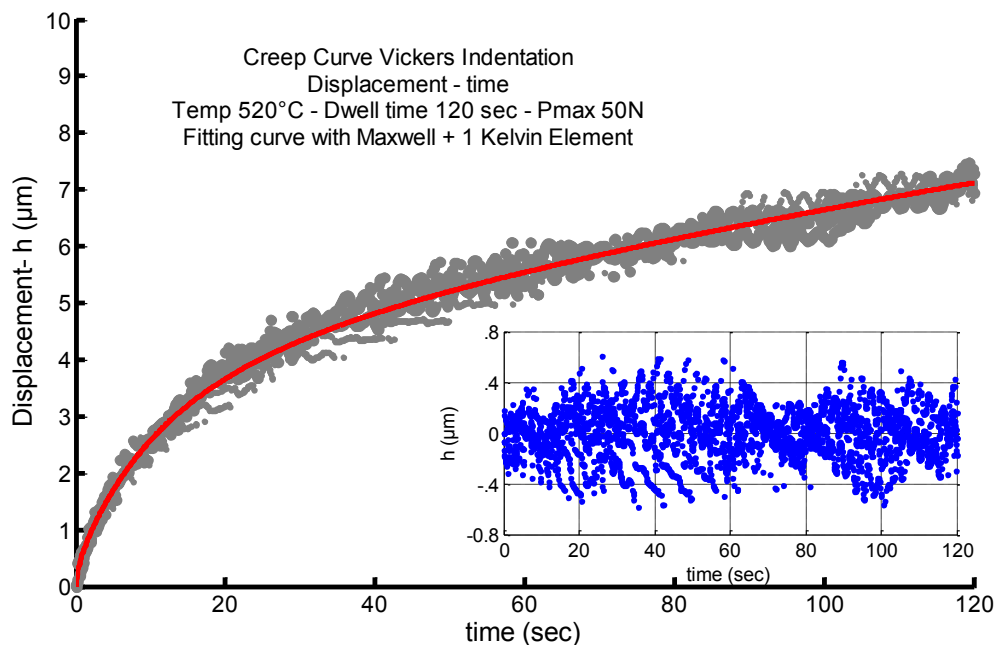


Figure 5.33: Creep curve of Vickers indentation at 520°C and 120s dwell time. The red line is the fitting curve and the residuals plot in the inset indicate good agreement.

In the indentation at different temperatures it was observed that the creep rate changes accordingly as can be seen in the Figure 5.34. At the lowest testing temperature of 520°C, the creep rate is high in the first 20 seconds and then starts to decrease until reaches a plateau with a minimum displacement during the rest of the test, which means that the viscous flow is decreasing after certain period of time. At 540°C the creep rate is higher than the creep rate at 520°C for the same period of time, and it takes more time to start decreasing. At 560°C the creep rate is considerably higher than at the lower temperatures and the indenter continues displacing at a fast rate during the rest of the dwell time of 120 seconds.

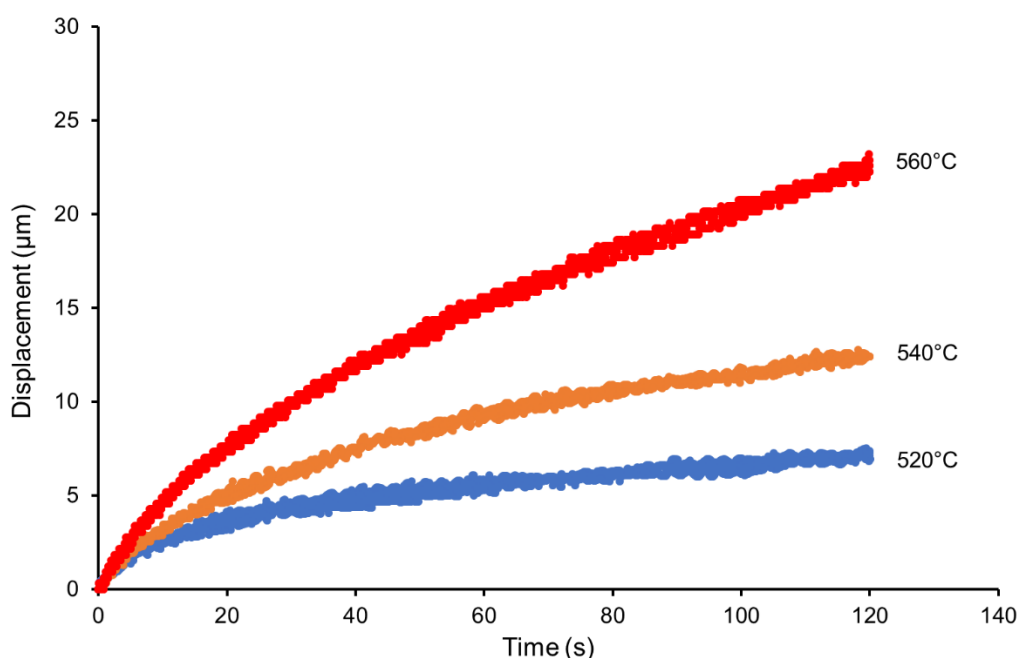


Figure 5.34: Indentation creep as a function of temperature for SLS glass. Higher creep rates are observed as the temperature of the test increases.

The Maxwell + 1 Kelvin element model was used to fit the indentation creep data at the 520, 540 and 560°C. The fitting constants were obtained and are shown in Table 5.7. It is interesting to observe the change with temperature of the constant  $C_0$ , which is the time-independent part of the compliance function expressed in equation 5.14. This constant is related to the inverse of the instantaneous reduced elastic modulus  $1/E_{r,0}$ , considering an indenter with ideal stiffness (Menčík et al 2011).

$$C_0 = \frac{(1 - \nu^2)}{E_0} \quad 5.28$$

The value of this constant increases with temperature indicating that the viscous behaviour is becoming dominant over the elastic.

*Table 5.7: Fitting constants of the Maxwell + 1 Kelvin elements model for indentation creep data at 520, 540 and 560°C, with a dwell time of 120s and a loading rate of 1.6N/s.*

<b>Temp.</b>	<b>C<sub>0</sub></b>	<b>C<sub>1</sub></b>	<b>C<sub>v</sub></b>	<b>τ<sub>1</sub></b>
520°C	0.335	0.211	0.01	22.34
540°C	0.635	2.32	0.025	28.18
560°C	1.356	-0.888	0.148	30

Due to the nature of the indentation test, the loading speed has also an influence in the shape of the creep curve since during the loading stage there will be some creep too. It can be observed in Figure 5.35 how with the faster loading speed of 5 N/s, the creep rate in the first seconds is larger than with the slower speed of 1.6 N/s. In the latter, part of the creep has already happened during the loading.

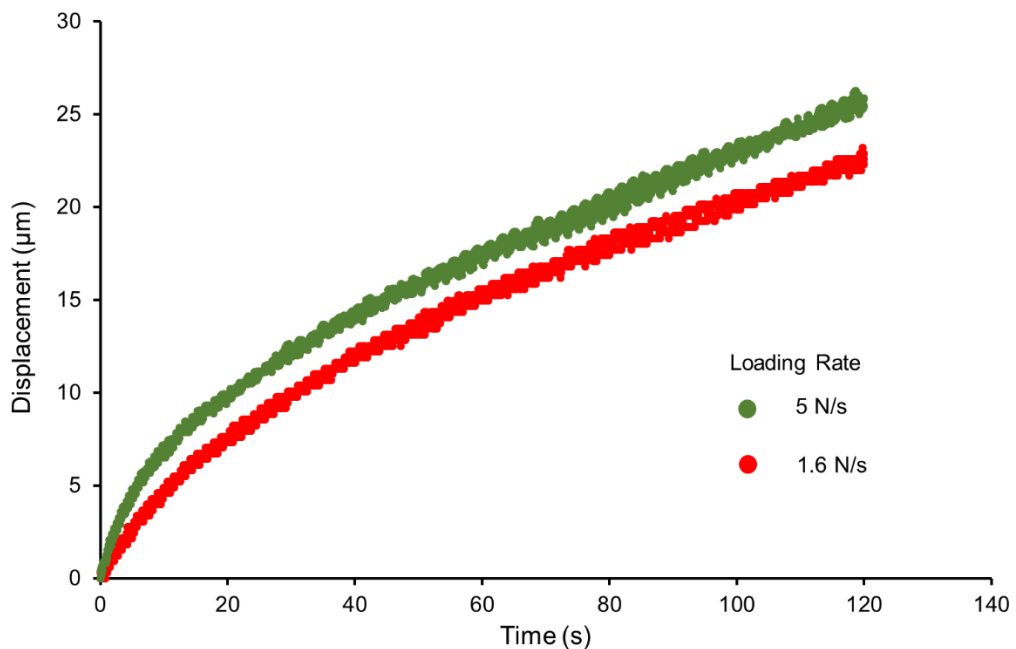


*Figure 5.35: Creep curves of a Vickers indentation experiment with two different loading rates at 560°C and a constant load of 50 N for a dwell time of 120 seconds.*

Therefore the instantaneous elastic response is also affected by the loading rate as can be seen by observing the constant  $C_0$  in the Table 5.8. The relaxation time  $\tau_1$  is also longer for the faster loading rate.

Table 5.8: Effect of loading speed on fitting constants of Vickers indentation. Model Maxwell + 1 Kelvin element at 560°C, 120s dwell time.

Loading rate (N/s)	$C_0$	$C_1$	$C_v$	$\tau_1$
1.6	1.356	-0.888	0.148	30
5.0	.726	-1.81	0.192	40.1

Because of the nature of the creep curve, a longer experimental duration enables a model to be obtained that better describes the viscoelastic behaviour. If the creep test is too short, the model will not completely describe the viscoelastic behaviour. The viscoelastic model using a Maxwell + 1 Kelvin element was obtained with experiments at different dwell times for the experiments at 560 and 520°C. In the experiment at 560°C shown in Figure 5.36, the prediction curves obtained at 30 and 60 s deviate from the data while the prediction curves calculated with longer test durations provide a better fit.

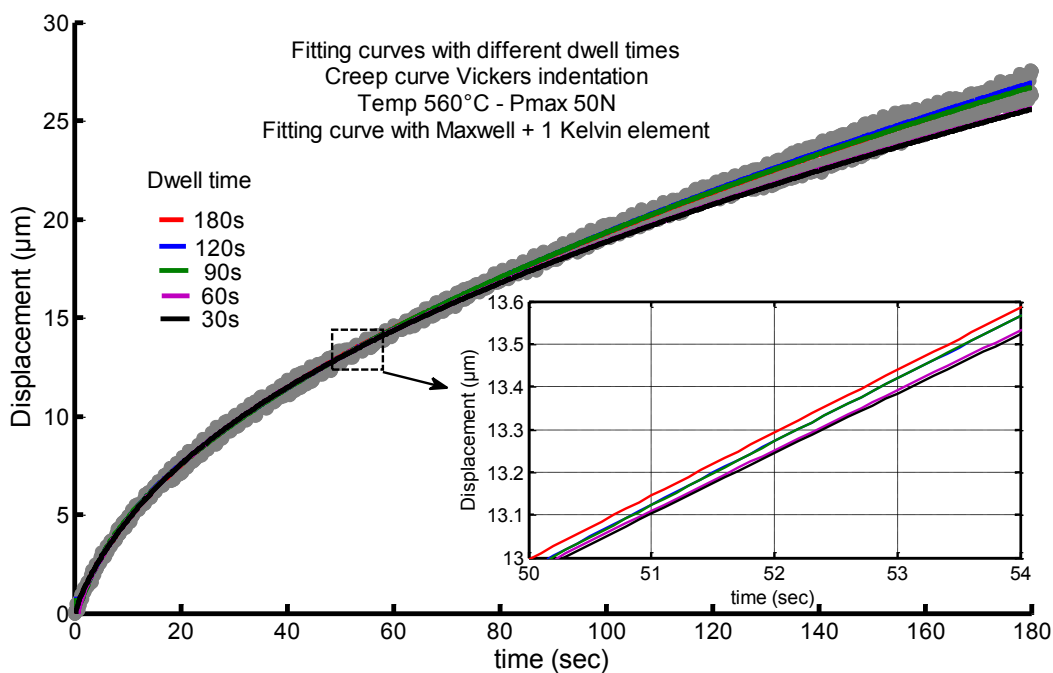


Figure 5.36: Vickers indentation creep curve at 560°C. Fitting curves were obtained with different dwell times. The models calculated after 90s fit better the data than the models obtained at shorter times.

In the case of the test at 520°C in Figure 5.37, the prediction curve calculated with shorter times can provide accurate fitting. It can be observed that at 60 s it is possible to obtain a good approximation to the experimental data, indicating that the relaxation took place over a shorter time interval.

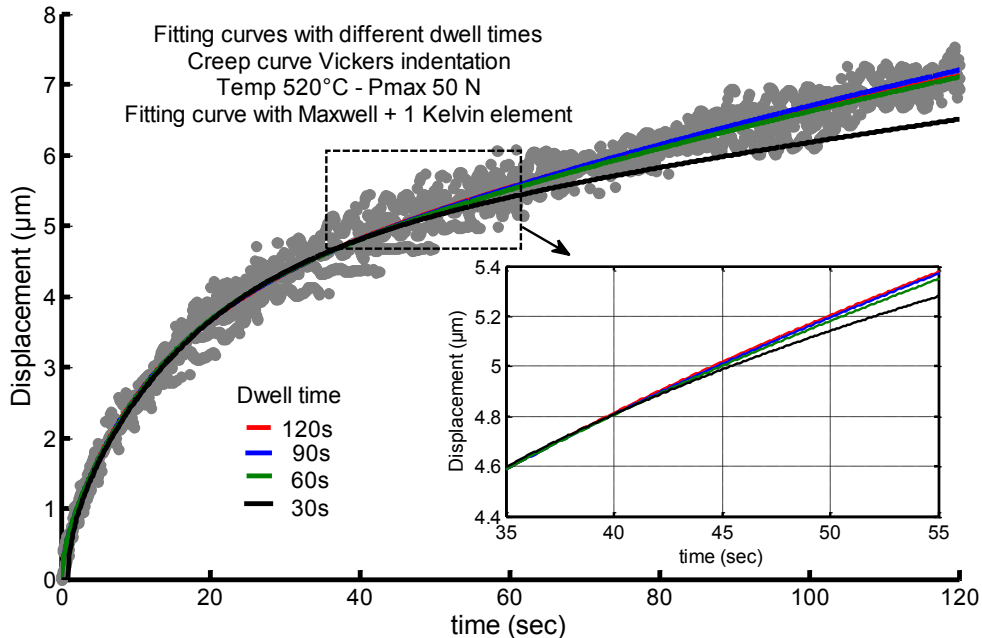


Figure 5.37: Vickers indentation creep curve at 520°C. Fitting curves were obtained at different dwell times. The models calculated with 60, 90 and 120 s fit better the data than the fitting curve calculated with 30s.

The creep curves obtained with a Hertzian indenter using the model below (equation 5.29) were significantly different from the curves obtained with Vickers indenter at the same temperature.

$$h^{3/2}(t) = \frac{3}{8\sqrt{R}} P \left[ B + C_v t - D_1 \exp\left(\frac{-t}{\tau_1}\right) \right] \quad 5.29$$

Table 5.9: Fitting constants using the Maxwell + 1 Kelvin element in Hertzian indentation experiments at 560°C and 150s according to equation 5.21.

Temp (°C)	C <sub>0</sub>	C <sub>1</sub>	C <sub>v</sub>	τ <sub>1</sub>
560	1.614	-2.01	0.509	12.33

It was observed also in the Hertzian experiment that although the same indenter speed was used, the loading rate increased significantly. In other words, it was easier with this type of indenter to reach the maximum load

than with the sharp indenter. Probably because of the larger contact area and therefore lower pressure exerted on the surface.

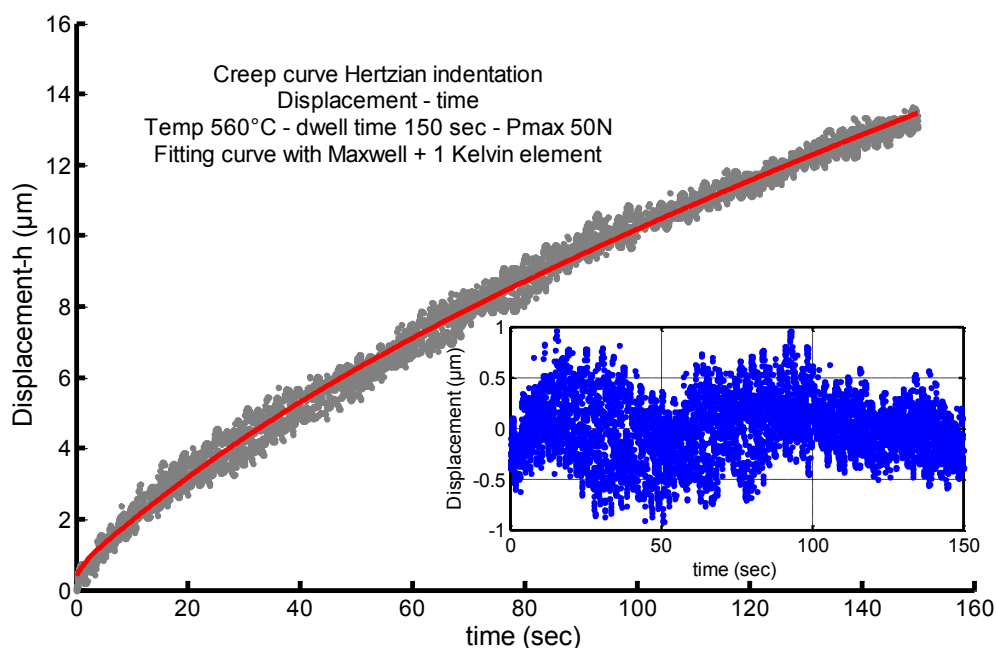


Figure 5.38: Creep curve of Hertzian indentation at 560°C and 150s dwell time. The fitting curve was obtained with a Maxwell + 1 Kelvin element model. Residuals of the fitting are shown in the inset.

Different values of the constants have been found in the indentation experiments when one of the testing conditions changes and even in the same experiment when the fitting is carried out using different intervals of time. The constants obtained in each experiment represent only the mathematical values that apply for that experiment with certain conditions and are not really a physical constant of the material.

## 5.7 Discussion.

Two types of experiment were carried out using the indentation apparatus at elevated temperatures. First, the analysis of the influence of the indentation test parameters on the size of the imprint left by the indenter and therefore on the Vickers hardness value. Second, the study of the surface response to contact using two different approaches, a modified Oliver and Pharr equation, and the use of rheological models in a creep experiment.

Most of the high temperature indentation experiments published in the literature were carried out at low loads, usually lower than 10 N. In the case of this work, it was decided to do the study at larger loads in order to create a damage of similar dimensions of those found in the manufacturing of automotive glass.

Those previous studies showed also a large scattering in the results of the Vickers hardness values (especially near  $T_g$ ), and as discussed in section 2.7.2, the possible cause was the different testing parameters used in the experiments. Therefore it was convenient to investigate the influence of such parameters on the Vickers hardness value by means of a Design of Experiment (DoE) approach. Load and temperature were kept fixed while different levels of loading speed, dwell time and unloading speed were used. The experiments were conducted on the air side only to be consistent with most of the published studies.

The hardness values obtained in this study were comparable to those of Kese et al (2008), Watanabe et al (2001) and Shang et al (2006) as can be seen in the following table.

Table 5.10 Comparative table of Vickers hardness at 560°C.

<i>Authors</i>	<i>Loading rate (mm/min)</i>	<i>Dwell time (sec)</i>	<i>Max. load (N)</i>	<i>Hv@Tg (GPa)</i>	<i>Atmosphere</i>	<i>Float side</i>
Le Bourhis and Metayer 2000	10	30	4.9	3.7	Argon	Air
Watanabe et al 2001	N/S	15	0.49	1.65	Vacuum	N/S
Le Bourhis and Rouxel 2003	10	30	4.9	3.7	Argon	Air
Shang et al 2006	N/S	30	.196	2.0	Ambient	Tin
Kese et al 2008	0.1	0	49	1.7	Ambient	Air
Wilantewicz and Varner 2008	0.012	0	9.8	3.4	Ambient	Air
<i>This Work</i>	<i>0.1</i>	<i>0</i>	<i>50</i>	<i>1.6</i>	<i>Ambient</i>	<i>Air</i>
	<i>0.1</i>	<i>15</i>	<i>50</i>	<i>1.2</i>	<i>Ambient</i>	<i>Air</i>
	<i>1.0</i>	<i>0</i>	<i>50</i>	<i>1.8</i>	<i>Ambient</i>	<i>Air</i>
	<i>1.0</i>	<i>15</i>	<i>50</i>	<i>1.3</i>	<i>Ambient</i>	<i>Air</i>

It can be observed how our results are comparable with the work of the authors that used similar dwell times and slow loading speeds. Higher Vickers values were obtained by Le Bourhis and Metayer (2000) and Le Bourhis and Rouxel (2003) who used very high loading speeds. It can be seen also that the maximum loads differ significantly between the works of the different authors, but this factor seems to have little influence in the results. Our results are also different from Wilantewicz and Varner (2008), who used a very slow loading speed and the Vickers hardness that they obtained was one of the highest in the comparative table. Unfortunately in our experiments we could not use slower loading speeds than 0.1 mm/min because it was noticed that the long period taken to reach the maximum load introduced considerable noise in the data due to fluctuations in internal and external temperatures, and therefore, undesired thermal expansions in the indenter column and in the sensors.

With the DoE it was possible to observe that the hardness decreased with increased dwell time and slower loading speed, as shown in Figure 5.10. The glass is in the viscoelastic state at  $T_g$  and the response of the surface to the mechanical load imposed during the test is time-dependent. The constant stress imposed during the dwell time initially produces an instantaneous elastic strain and a delayed elastic strain as explained in section 5.5.2, and also an irreversible flow of material that increases with time and that will define the size of the imprint.

Part of the irreversible flow occurs also during the loading stage; this is the reason why, even with zero dwell time, a slower loading speed produces lower hardness. Nevertheless, the interaction plot in Figure 5.11 shows how the effect of the loading speed becomes more irrelevant with increased dwell times.

Traditionally the Oliver and Pharr approach is used to obtain the hardness and the elastic modulus in elastic-plastic materials, where pure elastic recovery is assumed in the unloading section of the load-displacement curve. However, as discussed before, this is not the case in viscoelastic materials such as polymers or SLS glass at a temperature near  $T_g$ . It was observed in the experiments at high temperature that the slope of the unloading curve increased in comparison with the experiments at room temperature, and in some cases the calculated stiffness became negative. This is because there was some displacement of the indenter due to creep greater in magnitude than the elastic recovery. In fact, the creep rate was large enough at the beginning of the unloading stage to create the effect of a nose or bulge in the curve. This effect was diminished in the analysis using a modified Oliver and Pharr equation and adding a dwell time before withdrawing the indenter, and it was noticed that with longer dwell times the creep rate was lower and therefore it was possible to obtain more sensible values of plain strain modulus compared to those obtained by other means at the same temperature.

In the experiments at room and high temperature, the Vickers hardness of the tin side was slightly larger than the air side, calculated either by the

analysis of the load-displacement curve (apparent hardness), or by imaging the residual imprint. This is consistent with a manufacturing practice in the flat and automotive glass industry where the tin side is preferred to be in contact with the tempering furnace rollers and bending moulds since it offers more resistance to scratches and marks.

The indentation experiments at different temperatures showed how the viscoelastic effect was present not only at the glass transition temperature but also at temperatures as low as 520°C, where it was observed that the properties kept changing with time. It was out of the scope of this work to study the behaviour in all the temperature range down to room temperature, but it can be deduced from the charts in Figure 2.15, that the viscoelastic effect might become predominant after 400°C where a change in the slope of the curves can be observed and where there is more disagreement in the reported hardness values due to the different test parameters. This trend is also evident in the behaviour of the elastic modulus with temperature in Figure 2.14, where this property decreases gradually until reaches  $T_g$ , and then a step change occurs.

Indentation experiments carried out at a fixed load and temperature allowed us to visualize the effect that contact time has on the extent of damage on the surface of the glass (hardness). An analogy of sharp contact at elevated temperatures for short periods of time in the glass manufacturing is when the glass is heated in a continuous roller furnace before bending and tempering. In this case, glass particles coming from broken glass become attached to the rollers causing indentation when the glass passes over them (generally called roller marks). Cleaning the rollers immediately after the issue is detected is not always feasible because of the production schedule. This activity would require shut down and cooling down of the furnace losing production time. Decreasing the temperature to avoid the roller marks is a solution that is difficult to attain because temperature affects the forming and tempering of the product but in most cases, this action is taken in the meantime that the problem is solved. Some manufactures inject SO<sub>2</sub> to the rollers in order to form a lubricant barrier between these and the glass, but this also has a drawback since in the long term it damages the surface of the

ceramic rollers. Experiments are being carried out at industrial level changing the furnace parameters to increase the speed of the glass and reduce the contact time. Preliminary results show smaller rollers marks that sometimes fall into the acceptable quality criteria which helps to improve the furnace output.

In the Vickers indentations at 560°C no cracks were found after the inspection with the microscope, this is consistent with the specimens of windscreen glass analysed in the first part of this chapter where no cracks around the embedded particles were detected either. It is considered that the viscous flow of the glass near  $T_g$  reduces the stress generated by the shape of the indenter and therefore the crack driving force.

The analytical approach for indentation of viscoelastic materials proposed by Feng and Ngan (2002) seems to be insufficient to describe the response of the glass to contact in the viscoelastic region. The properties keep changing with time as seen in Figure 5.22 and Figure 5.26, and defining a single value of hardness or plain strain modulus would not be appropriate.

It was possible to fit the data of the indentation creep experiments using combinations of Maxwell and Kelvin elements in a mechanical model. Only one Kelvin element was required to obtain a good fitting with longer dwell times in the experiment. As it was expected, the constants obtained in the fitting changed with the temperature, but also with other factors such as the type of the indenter and the loading rate.

The three stages that represent the viscoelastic behaviour of the glass (Figure 5.14) are embodied in the mechanical models used to fit the indentation data, and it is necessary to consider the model as a whole, since each constant separately does not have a physical meaning or can be converted into a mechanical property. For example, it is not possible to calculate the value of the instantaneous elastic modulus since in this type of experiment the load is not applied instantaneously; however, in other experimental methods such as Brillouin scattering (which is a dynamic method at very high frequencies) a better approximation to the real values of the elastic constants can be obtained (Duffrène et al 1998).

Nevertheless, the model obtained for indentation describes adequately the contact response of the glass in the viscoelastic state, and it is possible to observe some trends in the constants, when the experimental conditions change. For example the constant  $C_0$ , which represents the instantaneous elastic behaviour, decreases with temperature and with slower loading rates.

The indentation creep experiments and its representation with Maxwell and Kelvin elements offer the opportunity to model the contact of the glass with surfaces that might have sharp or blunt particles attached during the forming at high temperature, as long as the experimental parameters approach to the real conditions. For example, in the contact of a furnace roller with a glass particle attached, the glass that passes over during the tempering process will be in contact with the particle for a few seconds only at a constant load and temperature. But in the case of a flat glass that is resting in a mould that would be press-formed, as in the case of windscreen or backlight forming, trapped particles between the die and the glass will be pressed against the surface for longer times.

## **6. Conclusions and suggested further work**

### **6.1 Introduction**

This research was set to experiment with the mechanical contact in soda lime silica float glass and the effects that has on its surfaces with unique characteristics.

The experimentation was carried out under testing conditions that are present in the storage and manufacturing of automotive glazing. Instrumented indentation at nano and macro levels was used as a tool from which the mechanical properties were extracted and their behaviour analysed.

The two main research subjects, contact on weathered surfaces and the contact at elevated temperatures, contribute and complement the existing knowledge in the scientific field on this type of glass. The experimentation in the lab with testing conditions similar to those found in the industry made possible to obtain results that help in the understanding of what is occurring in the manufacturing process and provide a scientific basis that can be used in technology development.

The conclusions are presented in the next section following the same order as were presented in the main text body of this thesis. Firstly, the main findings regarding the evolution of the mechanical properties of the surface of SLS float glass when is exposed to weathering. Secondly, the design, build and calibration of the laboratory apparatus used to perform the instrumented indentation at elevated temperatures. And lastly, final remarks are made regarding the instrumented indentation at temperatures near and at the glass transition temperature where mechanical models are used to analyse the creep behaviour and properties of the glass.

### **6.2 Hydration and mechanical properties**

The chemical characteristics of the soda lime silica float glass surfaces have been studied widely and there are many published works in the

literature. The effect of weathering on both surfaces of this type of glass has been also covered in several research papers. However, the study of the effect of the corrosion caused by the weathering in the mechanical properties is quite limited. The research carried out in this work provides evidence of the change of the mechanical properties with exposure time to weathering. Both surfaces react differently with the hydrogen in the atmosphere. The air side is more chemical and mechanically affected than the tin side.

The mechanical properties on the near surface of the air and tin sides of soda lime silica glass exposed to 95% of relative humidity and 40°C in a weathering chamber evolve at different rates as the exposure period increases. The nanohardness and reduced modulus of the air side decreases as the exposure time increases at a given contact depth. On the other hand, there is little change in elastic modulus and nanohardness in the tin side with the same exposure conditions. It is indicative that the tin that is present in this surface inhibits significantly the corrosion process.

Additional evidence of the different reaction of both glass surfaces was obtained with the use of SEM and EDX. Formation of crystallites were observed in the surface in more extent on the air side. The chemical analysis showed that were either calcium or sodium rich. On the tin side this crystallites were also formed but in a lesser degree and in the longer exposure times.

### **6.3 Apparatus for high temperature indentation**

An apparatus was developed in the laboratory in order to investigate the response of the SLS float glass to contact at high temperature. This apparatus was capable to perform blunt and sharp indentations in glass specimens at a temperature up to 560°C. Currently there are only a few devices commercially available to do this type of study. To design and build this device for the study represented a challenge and required a long process of adjustments and calibrations before it was able to provide reproducible and reliable data.

All necessary calibrations were carried out and it was found that the standard procedures to calculate the machine compliance were not sufficient to describe the mechanical yielding of the system during the test. Usually, the compliance factor is a value that is calculated after testing at different loads in a material of known elastic properties and is applied to adjust the measured displacement value. In the case of our apparatus, the compliance proved to be different in loading and unloading, and also, the compliance was better described by a quadratic equation rather than a single value. The verification that the compliance was the same at room and high temperatures allowed the calibration curve to be obtained using Hertzian indentation on fused silica to measure its elastic deformation and subtract this from the total displacement. This procedure permitted visualization of the way in which the machine was deflecting elastically during the indentation experiments.

#### **6.4 Indentation at high temperatures**

The indentation at high temperature was used to characterize the response of the SLS float glass to contact. The study started with the analysis of an industrial case of contact of glass and mould in the manufacturing of automotive glass, and with the investigation of the glass transition temperature of this glass by means of dilatometry and differential thermal analysis (DTA). The temperature of 560°C was identified as the appropriate value to describe the temperature (range) where the glass transition occurs.

A representative example of the contact of glass at elevated temperatures is in the bending of flat glass into a curved shape using a mould, as in the case of the manufacture of automotive windscreens. Specimens with defects generated due to this contact were analysed using different analytical techniques and interesting findings were obtained.

The observation of the mould marks under the microscope revealed that many of them had particles embedded in the surface and subsequent analysis revealed that they were of the same composition of the windscreen material (SLS float glass) and some of them contained traces of the steel

used in the moulds. The adhesion of the glass particles to the mould is feasible as was discussed in the chapter, and it is possible that the characteristics of the steel alloy used in the mould could promote a firm adhesion.

The review of published literature about Vickers indentation at high temperatures revealed discrepancies between the different works in the hardness values reported. One possible explanation was in terms of the different test parameters chosen by each researcher. Therefore it was decided to do a design of experiments to analyse the role that the different stages of an indentation experiment has on the final result. Temperature and maximum load was maintained fixed while the loading speed, dwell time and unloading speed were studied in different levels. The response factor was defined as the hardness value calculated by measuring the average diagonal size left by the indenter in the glass surface.

The dwell time was found as the most significant factor to affect the imprint size followed by the loading speed. The interaction of these two factors was also relevant. The temperature of 560°C at which the experiments were done explained much of the influence of those two factors due to the predominant viscous behaviour of the glass at this temperature.

Room temperature indentations on SLS glass carried out with the instrumented indentation apparatus and the hardness and elastic modulus were calculated. Similar to what was found in the nanoindentation of fresh glass (not exposed to weathering), the value of these two properties was slightly higher for the tin side over the air side.

The temperature and the dwell time had an effect not only in the imprint left by the indenter from which the hardness can be calculated, but also in the shape of the load-displacement curve complicating the analysis to obtain the apparent hardness and the elastic modulus. Two approaches were followed, the first one was to apply a correction to compensate the viscoelastic effect in the Oliver and Pharr method in order to obtain the two properties at different temperatures and dwell times. The second analysis consisted in applying mechanical models and viscoelastic corrections to the contact mechanics

equations to fit the creep curves obtained in the experiments during the dwell time at maximum load. Although the constants obtained do not describe specifically a material property they provide a clear idea of the behaviour of the elastic response and the viscous flow of the glass at those specific conditions.

## **6.5 Further research work**

The study of the properties of the hydrated layer on both surfaces of the SLS float glass offers an insight on how a modified surface can alter the overall performance of the substrate in terms of the resistance to contact. The current study was conducted under laboratory conditions, but it would be interesting to carry out a similar study with glass under actual service environment where contaminants might exist and, where the temperature and humidity may be cyclical.

The scarce information found in the literature regarding the fracture strength of both surfaces of float glass and the lack of conclusive reports on the long term mechanical performance of weathered glass means that this is an interesting field for further research. Regarding Vickers indentation of glass exposed to weathering, the existing studies are rather limited and contradictory. Also, there are no published studies of Hertzian indentation on weathered float glass, which means there is a gap into the existing knowledge that needs to be filled; being this a field of important application for the industry.

The laboratory apparatus developed for this research was used mainly to carry out indentations on the surface of glass in a given range of temperatures, however, slight modifications can expand the temperature working range and its accuracy. The apparatus in its current condition can be used to study other properties of glass such as viscosity and toughness, as well to carry out research in other materials.

The brief analysis carried out on glass samples with mould marks, opened an interesting field of research that can lead to the improvement of the

manufacturing of automotive glass. It is important to define if the adhesion of glass particles to the contact surface of the mould is related to the steel used on them, and if this defect can be reduced by using a different material. By continuing this study, old myths in the tooling fabrication and the glass bending process can be challenged helping to develop new and improved practices.

The analysis carried out about the response to contact at elevated temperatures raises the question on how to apply this knowledge in the prediction models used for the forming of flat glass and in the improvement of tooling and processes to reduce defects caused by contact at high temperatures. The analysis methodology can be applied to the long term contact of glass and moulds in the gravity bending processes of windscreens, or in the short term contact of glass and ceramic and metallic rollers in the tempering process.

It would be interesting to explore the extrapolation of the methodology used here to analyse not only the contact in the surface but, also the contact to modify the shape of the entire piece, such as in the press forming processes of flat glass.

In this study, due to the limitations of the experimental apparatus and time, experiments were conducted only in a short range of temperatures near  $T_g$ . Nevertheless, it would be important to conduct further studies in the whole temperature range from room temperature up to 620°C, which comprises the temperature range that the glass experiences while is formed in the bending furnaces of automotive glass.

## References

- Anstis, G. R., Chantikul, P., Lawn, B. R. and Marshall, D. B. (1981) A critical evaluation of indentation techniques for measuring fracture toughness. 1. Direct crack measurements. *Journal of the American Ceramic Society*, **64**(9), 533-538.
- Arora, A., Marshall, D. B. and Lawn, B. R. (1979) Indentation Deformation-Fracture of normal and anomalous glasses. *Journal of Non-Crystalline Solids*, **31**(3), 415-428.
- ASTM, Standard C1421-10, (1999) "*Standard Test Methods for Determination of Fracture Toughness of Advanced Ceramics at Ambient Temperature*", ASTM International, West Conshohocken, PA, DOI: 10.1520/C1421-10, www.astm.org.
- ASTM, Standard E1545-11, (2011) "*Standard Test Method for Assignment of the Glass Transition Temperature by Thermomechanical Analysis*", ASTM International, West Conshohocken, PA, DOI: 10.1520/E1545-11, www.astm.org.
- ASTM, Standard E1545-11, (2014) "*Standard Test Method for Assignment of the Glass Transition Temperatures by Differential Scanning Calorimetry*", ASTM International, West Conshohocken, PA, DOI: 10.1520/E1356, www.astm.org.
- Bange, K., Anderson, O., Rauch, F., Lehuede, P., Radlein, E., Tadokoro, N., Mazzoldi, P., Rigato, V., Matsumoto, K. and Farnworth, M. (2002) Multi-method characterization of soda-lime glass corrosion. Part 2. Corrosion in humidity. *Glass Science and Technology*, **75**(1), 20-33.
- Bao, Y. W. and Gao, S. J. (2008) Local strength evaluation and proof test of glass components via spherical indentation. *Journal of Non-Crystalline Solids*, **354**(12-13), 1378-1381.
- Bao, Y. W., Su, S. B., Yang, J. J., Sun, L. and Gong, J. H. (2002) Non-destructively determining local strength and residual stress of glass by Hertzian indentation. *Acta Materialia*, **50**(18), 4659-4666.
- Beek, J. J. H. and Lawn, B. R. (1972) An environmental chamber for hertzian fracture testing. *Journal of Physics E: Scientific Instruments*, **5**(7), 710.
- Bent, J.F., Hannon, A.C., Holland, D. and Karim, M.M.A. (1998) The structure of tin silicate glasses. *Journal of Non-Crystalline Solids*, **232-234**, 300-308.

- Bernard, C., Keryvin, V., Sangleboeuf, J. C. and Rouxel, T. (2010) Indentation creep of window glass around glass transition. *Mechanics of Materials*, **42**(2), 196-206.
- Berndt, C. C. (1989) Failure processes within ceramic coatings at high temperatures. *Journal of Materials Science*, **24**(10), 3511-3520.
- Bisrat, Y. and Roberts, S. G. (2000) Residual stress measurement by Hertzian indentation. *Materials Science and Engineering A, Structural Materials: Properties, Microstructure and Processing*, **288**(2), 148-153.
- Bourne, R., Cowan, N. D. and Budd, S. M. (1984) Damage to glass surfaces at elevated temperature: Effects of hardness and thermal conductivity of damaging material. *Glass Technology*, **25**(3), 145-147.
- Bradley, L. C., Dilworth, Z. R., Barnette, A. L., Hsiao, E., Barthel, A. J., Pantano, C. G. and Kim, S. H. (2013) Hydronium Ions in Soda-lime Silicate Glass Surfaces. *Journal of the American Ceramic Society*, **96**(2), 458-463.
- Bridgman, P. W. and Simon, I. (1953) Effects of Very High Pressures on Glass. *Journal of Applied Physics*, **24**(4), 405-413.
- British Stainless Steel Association. (2014) *AISI & UNS compositions and properties*, Technical library. [ONLINE] Available at: [www.bssa.org.uk](http://www.bssa.org.uk). [Accessed 29 July 2014].
- Brückner, R. (1970) Properties and structure of vitreous silica. I. *Journal of Non-Crystalline Solids*, **5**(2), 123-175.
- Budd, S. M., Cowan, N. D. and Bourne, R. (1980) Damage to glass surfaces by various materials at elevated temperature. *Journal of Non-Crystalline Solids*, **38-39**(1), 409-412.
- Chiang, S. S., Marshall, D. B. and Evans, A. G. (1982) The response of solids to elastic/plastic indentation. I. Stresses and residual stresses. *Journal of Applied Physics*, **53**(1), 298-311.
- Clark, D. E., Pantano, C. G. and Hench, L. L. (1979) *Corrosion of Glass*. New York: Magazines for Industry.
- Coney, S.S. (1978) The selection and use of coatings for the glass forming equipment. *Glass Technology*, **19**(6).
- Cook, R. F. and Pharr, G. M. (1990) Direct observation and analysis of indentation cracking in glasses and ceramics. *Journal of the American Ceramic Society*, **73**(4), 787-817.

Cseh, G., Chinh, N. Q., Tasnadi, P., Szommer, P. and Juhasz, A. (1997) Indentation tests for the investigation of the plasticity of glasses. *Journal of Materials Science*, **32**(7), 1733-1739.

CSM Instruments. (2003) *New applications of instrumented Indentation. Applications Bulletin 19* [Online]. Available at: [www.csm-instruments.com](http://www.csm-instruments.com) [Accessed:Nov. 2013]

Dériano, S., Jarry, A., Rouxel, T., Sangleboeuf, J. C. and Hampshire, S. (2004) The indentation fracture toughness (K<sub>IC</sub>) and its parameters: the case of silica-rich glasses. *Journal of Non-Crystalline Solids*, **344**(1), 44-50.

Donald, Ian W. (2009) *Glass-to-metal seals*. Sheffield, U. K.: Society of Glass Technology.

Doremus, R. H. (1979) Chemical Durability of Glass. *Treatise on materials science and technology*, **17**, 41-69.

Doremus, R.H. (1981) Time dependence of the reaction of water with glass. *Nuclear and Chemical Waste Management*, **2**(2), 119-123.

Doremus, R. H. (1994) *Glass Science*. 2nd Edition. New York: John Wiley & Sons.

Doremus, R. H., Mehrotra, Y., Lanford, W. A. and Burman, C. (1983) Reaction of water with glass - Influence of a transformed surface layer. *Journal of Materials Science*, **18**(2), 612-622.

Dorner, D., Röller, K., Skrotzki, B., Stöckhert, B. and Eggeler, G. (2003) Creep of a TiAl alloy: a comparison of indentation and tensile testing. *Materials Science and Engineering A Structural Materials: Properties, Microstructure and Processing*, **357**, 346-354.

Duffrène, L., Gy, R., Burlet, H., Piques, R., Faivre, A., Sekkat, A. and Perez, J. (1997) Generalized Maxwell model for the viscoelastic behaviour of a soda-lime-silica glass under low frequency shear loading. *Rheologica Acta* **36**(2), 173-186.

Evans, A. G. and Charles, E. A. (1976) Fracture toughness determinations by indentation. *Journal of the American Ceramic Society*, **59**(7-8), 371-372.

Faisal, N. H., Ahmed, R. and Reuben, R. L. (2011) Indentation testing and its acoustic emission response: applications and emerging trends. *International Materials Review*, **56**(2), 98-142.

Farber, B. Y., Orlov, V. I. and Heuer, A. H. (1998) Energy Dissipation during High Temperature Displacement-Sensitive Indentation in Cubic Zirconia Single Crystals. *Physica Status Solidi (a)*, **166**(1), 115-126.

Feng, G. and Ngan, A. H. W. (2002) Effects of creep and thermal drift on modulus measurement using depth-sensing indentation. *Journal of Materials Research*, **17**(03), 660-668.

Fischer-Cripps, A. C. (2004) A simple phenomenological approach to nanoindentation creep. *Materials Science and Engineering A Structural Materials: Properties, Microstructure and Processing*, **385**(1-2), 74-82.

Frank, F.C. and Lawn, B.R. (1967) On the theory of Hertzian fracture. *Proceedings of the Royal Society A*, **229**, 291-306.

Freiman, S. W., Wiederhorn, S. M. and Mecholsky, J. J. (2009) Environmentally Enhanced Fracture of Glass: A Historical Perspective. *Journal of the American Ceramic Society*, **92**(7), 1371-1382.

Frischat, G. H., Müller-Fildebrandt, C., Moseler, D. and Heide, G. (2001) On the origin of the tin hump in several float glasses. *Journal of Non-Crystalline Solids*, **283**(1-3), 246-249.

Fulcher, J. T., Lu, Y. C., Tandon, G. P. and Foster, D. C. (2010) Thermomechanical characterization of shape memory polymers using high temperature nanoindentation. *Polymer Testing*, **29**(5), 544-552.

Geandier, G., Denis, S. and Mocellin, A. (2003) Float glass fracture toughness determination by Hertzian contact: experiments and analysis. *Journal of Non-Crystalline Solids*, **318**(3), 284-295.

Geng, K., Yang, F. and Grulke, E. A. (2008) Nanoindentation of submicron polymeric coating systems. *Materials Science and Engineering A Structural Materials: Properties, Microstructure and Processing*, **479**(1-2), 157-163.

Gong, J. H., Chen, Y. F. and Li, C. Y. (2001). Statistical analysis of fracture toughness of soda-lime glass determined by indentation. *Journal of Non-Crystalline Solids*, **279**(2-3), 219-223.

Griffith, A.A. (1921). The Phenomena of Rupture and Flow in Solids. *Philosophical Transactions of the Royal Society A*, **221**(582-593), 163-198

Gulati, S. T., Akcakaya, R. and Varner, J. R. (2000). *Fracture behaviour of tin vs. air side of float glass*. *Ceramic Transactions* **122**, 317-325.

Hayashi, Y., Matsumoto, K. and Kudo, M. (2001) The diffusion mechanism of tin into glass governed by redox reactions during the float process. *Journal of Non-Crystalline Solids*, **282**(2-3), 188-196

Hayashi, Y., Fukuda, Y. and Kudo, M. (2002) Investigation on changes in surface composition of float glass--mechanisms and effects on the mechanical properties. *Surface Science*, **507-510**, 872-876.

Hertz, H. (1896) *Hertz's Miscellaneous Papers*. London: Macmillan.

Holland, Leslie. (1964) *The properties of glass surfaces*. London: Chapman & Hall.

Huang, L. and Kieffer, J. (2004) Amorphous-amorphous transitions in silica glass. I. Reversible transitions and thermo-mechanical anomalies. *Physical Review B*, **69**(22), 224203.

Hull, A. W. and Burger, E. E. 1934. Glass to Metal Seals. *Journal of Applied Physics* **5**(12), 384-405.

Johnson, K. L. (1985) *Contact mechanics*. Cambridge, UK: Cambridge University Press.

Kalidindi, S. R., Abusafieh, A. and El-Danaf, E. (1997) Accurate characterization of machine compliance for simple compression testing. *Experimental Mechanics*, **37**(2), 210-215.

Kese, K., Sangleboeuf, J. C. and Rouxel, T. (2008) Effect of high-temperature ambience during sharp indentation on the residual contact site properties. *Journal of Physics D: Applied Physics*, **41**(7).

Kim, K. Y. and Sachse, W. (1984) Characteristics of acoustic emission signals of Hertzian and unloading cracks in glass. *Journal of Applied Physics*, **55**(8), 2847-2856.

Krohn, M. H., Bradt, R. C., Munz, D., Sakai, M., White, K. W., Hellmann, J. R., Pantano, C. G., Lower, N. P. and Brow, R. K. (2005). *Effects of Tin on the Physical Properties and Crack Growth in Soda-Lime-Silica Float Glass*. In: *Fracture Mechanics of Ceramics*. Springer US, 135-148.

Krohn, M. H., Hellmann, J. R., Shelleman, D. L. and Pantano, C. G. (2002). Biaxial Flexure Strength and Dynamic Fatigue of Soda-Lime-Silica Float Glass. *Journal of the American Ceramic Society* **85**(7), 1777-1782.

Kurkjian, C. R. and Prindle, W. R. (1998) Perspectives on the History of Glass Composition. *Journal of the American Ceramic Society*, **81**(4), 795-813.

Lanford, W. A., Davis, K., Lamarche, P., Laursen, T., Groleau, R. and Doremus, R. H. (1979) Hydration of soda-lime glass. *Journal of Non-Crystalline Solids*, **33**(2), 249-266.

Lawn, B. (1993) *Fracture of Brittle Solids*. 2nd Edition. Cambridge: Cambridge University Press.

Lawn, B. and Wilshaw, R. (1975) Indentation fracture - Principles and applications. *Journal of Materials Science*, **10**(6), 1049-1081.

Lawn, B. R., Evans, A. G. and Marshall, D. B. (1980) Elastic/Plastic indentation damage in ceramics: the median/radial crack system. *Journal of the American Ceramic Society*, **63**(9-10), 574-581.

Lawn, B. R. and Swain, M. V. (1975) Microfracture beneath point indentations in brittle solids. *Journal of Materials Science*, **10**(1), 113-122.

Le Bourhis, E. (1998) Tin influence on the thermomechanical behaviour of silico-soda-lime glass. *Verre*, **4**(5), 5-8.

Le Bourhis, E. and Metayer, D. (2000) Indentation of glass as a function of temperature. *Journal of Non-Crystalline Solids*, **272**(1), 34-38.

Le Bourhis, E. and Rouxel, T. (2003) Indentation response of glass with temperature. *Journal of Non-Crystalline Solids*, **316**(1), 153-159.

Le Houerou, V., Sangleboeuf, J. C., Deriano, S., Rouxel, T. and Duisit, G. (2003) Surface damage of soda-lime-silica glasses: indentation scratch behavior. *Journal of Non-Crystalline Solids*, **316**(1), 54-63.

Lee, E. H. and Radok, J. R. M. (1960) The Contact Problem for Viscoelastic Bodies. *Journal of Applied Mechanics*, **27**(3), 438-444.

Mathworks Documentation. (2013) *Least-Squares (Model Fitting) Algorithms*. [Online] Available at: [www.mathworks.com/help/optim/ug/least-squares-model-fitting-algorithms.html](http://www.mathworks.com/help/optim/ug/least-squares-model-fitting-algorithms.html) [Accessed:9th Sep. 2013]

Lombardo, T., Chabas, A., Lefevre, R. A., Verita, M. and Geotti-Bianchini, F. (2005) Weathering of float glass exposed outdoors in an urban area. *Glass Technology*, **46**(3), 271-276.

Lu, Y. C., Jones, D. C., Tandon, G. P., Putthararat, S. and Schoeppner, G. A. (2010) High Temperature Nanoindentation of PMR-15 Polyimide. *Experimental Mechanics*, **50**(4), 491-499.

Makishima, A. and Mackenzie, J. D. (1973) Direct calculation of Young's modulus of glass. *Journal of Non-Crystalline Solids*, **12**(1), 35-45.

Mazurin, O. V. and Gankin, Yu V. (2008) Glass transition temperature: problems of measurement procedures. *Glass Technology - European Journal of Glass Science and Technology Part A*, **49**(5), 229-233.

Mencik, J., He, L. H. and Nemecek, J. (2011) Characterization of viscoelastic-plastic properties of solid polymers by instrumented indentation. *Polymer Testing*, **30**(1), 101-109.

Mencik, J., He, L. H. and Swain, M. V. (2009) Determination of viscoelastic-plastic material parameters of biomaterials by instrumented indentation. *Journal of the mechanical behaviour of biomedical materials*, **2**(4), 318-325.

Meszaros, R., Wild, M. and Wondraczek, L. (2013) Effects of substrate and long term corrosion on PVD-multilayer coatings for architectural glazing. *Glass Technology-European Journal of Glass Science and Technology Part A*, **54**(5), 177-184.

Michalske, T.A. and Freiman, S.W. (1983) Molecular mechanism for stress corrosion in vitreous silica. *Journal of the American Ceramic Society*, **66**(4), 284-288.

Michel, M. D., Mikowski, A., Lepienski, C. M., Foerster, C. E. and Serbena, F. C. (2004) High temperature microhardness of soda-lime glass. *Journal of Non-Crystalline Solids*, **348**, 131-138.

Ngan, A. H. W. and Tang, B. (2002) Viscoelastic effects during unloading in depth-sensing indentation. *Journal of Materials Research*, **17**(10), 2604-2610.

NIST/Sematech. (2012) *e-Handbook of Statistical Methods*, [ONLINE] Available at: [www.itl.nist.gov/div898/handbook/](http://www.itl.nist.gov/div898/handbook/), [Accessed 24<sup>th</sup> Apr 2012]

NSG Group. (2013) *Properties of soda lime silica float glass*. [ONLINE] Available at: [www.pilkington.com/resources/](http://www.pilkington.com/resources/). [Accessed 4th Aug 2014].

Odegard, G. M., Gates, T. S. and Herring, H. M. (2005) Characterization of viscoelastic properties of polymeric materials through nanoindentation. *Experimental Mechanics*, **45**(2), 130-136.

Ojovan, M. I., Hand, R. J., Ojovan, N. V. and Lee, W. E. (2005) Corrosion of alkali-borosilicate waste glass K-26 in non-saturated conditions. *Journal of Nuclear Materials*, **340**(1), 12-24.

Oliver, W. C. and Pharr, G. M. (1992) Improved technique for determining hardness and elastic modulus using load and displacement sensing indentation experiments. *Journal of Materials Research*, **7**(6), 1564-1580.

Oyen, M. L. (2005) Spherical Indentation Creep Following Ramp Loading. *Journal of Materials Research*, **20**(08), 2094-2100.

Oyen, M. L. (2006) Analytical techniques for indentation of viscoelastic materials. *Philosophical Magazine*, **86**(33-35), 5625-5641.

Oyen, M. L. and Cook, R. F. (2003) Load-displacement behaviour during sharp indentation of viscous-elastic-plastic materials. *Journal of Materials Research*, **18**(1), 139-150.

Pantano, C.G., Bojan, V., Verità, M., Geotti-Bianchini, F. and Hreglich, S. (1993) Tin Profiles in the bottom surface of float glass: Manufacturing and heat treatments effects. *Fundamentals of Glass Science and Technology. ESG. Venice. Supplement to Rivista della Stazione Sperimentale del Vetro*, **23**, 285-290.

Pech, J., Braccini, M., Mortensen, A. and Eustathopoulos, N. (2004) Wetting, interfacial interactions and sticking in glass/steel systems. *Materials Science and Engineering A Structural Materials: Properties, Microstructure and Processing*, **384**(1-2), 117-128.

Perriot, A. and Barthel, J. (2004) Elastic contact to a coated to a coated half-space: Effective elastic modulus and real penetration. *Journal of Materials Research*, **19**(2), 600-608.

Peter, K. W. (1970) Densification and flow phenomena of glass in indentation experiments. *Journal of Non-Crystalline Solids*, **5**(2), 103-115.

Pilkington, L. A. B. (1969) Review lecture. The Float Glass Process. Proceedings of the Royal Society of London. Series A, Mathematical and Physical Sciences, **314**(1516), 1-25.

Ponton, C. B. and Rawlings, R. D. (1989a) Vickers Indentation fracture toughness test. 1. Review of literature and formulation of standardized indentation toughness equations. *Journal of Materials Science and Technology*, **5**(9), 865-872.

Ponton, C. B. and Rawlings, R. D. (1989b) Vickers indentation fracture toughness test. 2. Application and critical evaluation of standardized indentation toughness equations. *Journal of Materials Science and Technology*, **5**(10), 961-976.

Puyane, R. (1976) *Damage to glass surfaces at high temperature*. PhD Thesis, Dept. of Ceramics, Glasses and Polymers, University of Sheffield.

Puyane, R. and Rawson, H. (1979) Reduction in the strength of glass by high temperature damage. *Glass Technology*, **20**(5), 186-193.

Quinn, G. D. and Bradt, R. C. (2007) On the Vickers indentation fracture toughness test. *Journal of the American Ceramic Society*, **90**(3), 673-680.

Rawson, H. (1988) Glass and its history of service. IEEE Proceedings A: Physical Science. Measurement and Instrumentation. Management and Education. Reviews, **135** (6), 325-345.

Reed, S. J. B. *Electron Microprobe Analysis and Scanning Electron Microscopy in Geology*. [Electronic version]. Cambridge. Cambridge University Press. Available at: <http://lib.myilibrary.com/Open.aspx?id=43496> [Accessed 28 July 2014]

Rieser, D., Spieß, G. and Manns, P. (2008) Investigations on glass-to-mold sticking in the hot forming process. *Journal of Non-Crystalline Solids*, **354**(12-13), 1393-1397.

Roberts, S. G., Lawrence, C. W., Bisrat, Y., Warren, P. D. and Hills, D. A. (1999) Determination of Surface Residual Stresses in Brittle Materials by Hertzian Indentation: Theory and Experiment. *Journal of the American Ceramic Society*, **82**(7), 1809-1816.

Rouxel, T. (2007) Elastic properties and short-to medium-range order in glasses. *Journal of the American Ceramic Society*, **90**(10), 3019-3039.

Sawa, T., Tsujii, M. and Kawazoe, M. (2006) *Instrumented Indentation test for high-temperature specimen*. XVIII Imeko World Congress. Rio de Janeiro, Brazil.

Scherer, G.W. (1986) *Relaxation in Glasses and Composites*. 1st. Edition. New York: John Wiley & Sons, Inc.

Scholze, H. (1988) Glass - Water Interactions. *Journal of Non-Crystalline Solids*, **102**(1-3), 1-10.

Shang, H., Rouxel, T., Buckley, M. and Bernard, C. (2006) Viscoelastic behaviour of a soda-lime-silica glass in the 293-833 K range by micro-indentation. *Journal of Materials Research*, **21**(3), 632-638.

Shinkai, N., Bradt, R. C. and Rindone, G. E. (1981) Fracture Toughness of Fused SiO<sub>2</sub> and Float Glass at Elevated Temperatures. *Journal of the American Ceramic Society*, **64**(7), 426-430.

Smedskjaer, M., Jensen, M. and Yue, Y. (2010) Effect of thermal history and chemical composition on hardness of silicate glasses. *Journal of Non-Crystalline Solids*, **356**(18-19), 893-897.

Sneddon, I. N. (1965) The relation between load and penetration in the axisymmetric boussinesq problem for a punch of arbitrary profile. *International Journal of Engineering Science*, **3**(1), 47-57.

Spinner, S. A. M. (1956) Elastic Moduli of Glasses at Elevated Temperatures by a Dynamic Method. *Journal of the American Ceramic Society*, **39**(3), 113-118.

Spinner, S. A. M. 1962. Temperature Dependence of Elastic Constants of Vitreous Silica. *Journal of the American Ceramic Society*, **45**(8), 394-397.

Ståhlberg, D., Nordin, L., Varna, J. and Johansson, M. (2005) Mechanical Response of Thermoset Polymers under High Compressive Loads, 1. *Macromolecular Materials and Engineering*, **290**(11), 1063-1072.

Szuecs, F., Werner, M., Sussmann, R. S., Pickles, C. S. J. and Fecht, H. J. (1999) Temperature dependence of Young's modulus and degradation of chemical vapour deposited diamond. *Journal of Applied Physics*, **86**(11), 6010-6017.

Tadjiev, D. R. and Hand, R. J. (2010) Surface hydration and nanoindentation of silicate glasses. *Journal of Non-Crystalline Solids*, **356**(2), 102-108.

Tadjiev, D. R., Hand, R. J. and Hayes, S. A. (2010) Calibrating a nanoindenter for very shallow depth indentation using equivalent contact radius. *Philosophical Magazine*, **90**(13), 1819-1832.

Tadjiev, D. R., Hand, R. J. and Zeng, P. (2010) Comparison of glass hydration layer thickness measured by transmission electron microscopy and nanoindentation. *Materials Letters*, **64**(9), 1041-1044.

Takeda, S., Yamamoto, K., Hayasaka, Y. and Matsumoto, K. (1999) Surface OH group governing wettability of commercial glasses. *Journal of Non-Crystalline Solids*, **249**(1), 41-46.

Tool, A. Q. (1946) Relation between inelastic deformability and thermal expansion of glass in its annealing range. *Journal of the American Ceramic Society*, **29**(9), 240-253.

Tooley, F. V. (1984) *The Handbook of Glass Manufacture*. 3rd Edition. New York: Ashlee Publishing Co.

Townsend, P. D., Can, N., Chandler, P. J., Farmery, B. W., Lopez-Herederó, R., Peto, A., Salvin, L., Underdown, D. and Yang, B. (1998) Comparisons of tin depth profile analyses in float glass. *Journal of Non-Crystalline Solids*, **223**(1), 73-85.

Tribometrix. (2013) *Very high temperature indentation*. [Online] Available at: [www.tribometrix.com/901/12922.html](http://www.tribometrix.com/901/12922.html) [Accessed:1st Sep. 2013]

Tummala, R. R. and Foster, B. J. (1975). Strength and dynamic fatigue of float glass surfaces. *Journal of the American Ceramic Society* **58**(3-4), 156-156.

Varshneya, A. K. (2006) *Fundamentals of Inorganic Glasses*. 2nd Edition. Sheffield: Society of Glass Technology.

Verità, M., Falcone, R., Sommariva, G., Chopinet, M.-H. and Lehuédé, P. (2009) Weathering of the inner surface of soda-lime-silica glass containers exposed to the atmosphere. *Glass Technology; European Journal of Glass Science and Technology Part A*, **50**(1), 65-70.

Verità, M., Geotti-Bianchini, F., Guadagnino, E., Stella, A., Pantano, C.G. and Paulson, T. (1995) "Chemical characterization of the bottom side of green float glasses." In *Fundamentals of Glass Science & Technology - 3rd ESG: Glastechnische Berichte - Glass Science and Technology*.

Verità, M., Geotti-Bianchini, F., Hreglich, S., Pantano, C.G. and Bojan, V. (1992) EPMA, RBS and SIMS analyses of Tin profiles in commercial float glasses. *Boletín de la Sociedad Española de Cerámica y Vidrio*, **31**-C(6).

Warren, B. E. (1934) X-Ray Determination of the structure of glass. *Journal of the American Ceramic Society*, **17**(1-12), 249-254.

Warren, P. D. (1995) Determining the fracture toughness of brittle materials by Hertzian indentation. *Journal of the European Ceramic Society*, **15**(3), 201-207.

Warren, P. D. and Hills, D. A. (1994) The influence of elastic mismatch between indenter and substrate on Hertzian fracture. *Journal of Materials Science*, **29**(11), 2860-2866.

Watanabe, M., Mercer, C., Levi, C. G. and Evans, A. G. (2004) A probe for the high temperature deformation of thermal barrier oxides. *Acta Materialia*, **52**(6), 1479-1487.

Watanabe, T., Benino, Y. and Komatsu, T. (2001) Change in Vickers hardness at the glass transition region for fragile and strong glasses. *Journal of Non-Crystalline Solids*, **286**(3), 141-145.

Westbrook, J. H. (1960) Hardness-temperature characteristics of some simple glasses. *Physics and Chemistry of Glasses*, **1**(1), 32-36.

Whittle, B. R. and Hand, R. J. (2001) Morphology of Vickers indent flaws in soda-lime-silica glass. *Journal of the American Ceramic Society*, **84**(10), 2361-2365.

Wiederhorn, S.M. (1967) Influence of Water Vapor on Crack Propagation in Soda-Lime Glass. *Journal of the American Ceramic Society*, **50**(8), 407-414.

Wilantewicz, T. E. and Varner, J.R. (2008) Vickers indentation behaviour of several commercial glasses at high temperatures. *Journal of Materials Science*, **43**(1), 281-298.

Williams, K. F. E., Johnson, C. E., Nikolov, O., Thomas, M. F., Johnson, J. A. and Greengrass, J. (1998) Characterization of tin at the surface of float glass. *Journal of Non-Crystalline Solids*, **242**(2), 183-188.

Yamamoto, A. (1965) *Detection of Characteristics points of commercial glasses by differential thermal analysis*. In: Robredo J., ed./eds. L'Analyse thermique differentielle en verrerie. Differential thermal analysis in glass. Commission Internationale du Verre 1967, 159-163.

Yamane, M. and Mackenzie, J. (1974) Vickers Hardness of Glass. *Journal of Non-Crystalline Solids*, **15**(2), 153-164.

Yoshida, S., Isono, S., Matsuoka, J. and Soga, N. (2001) Shrinkage Behaviour of Knoop Indentations in Silica and Soda-Lime-Silica Glasses. *Journal of the American Ceramic Society*, **84**(9), 2141-2143.

Yoshida, S., Sangleboef, J. C. and Rouxel, T. (2007) Indentation-induced densification of soda-lime silicate glass. *International Journal of Materials Research*, **98**(5), 360-364.

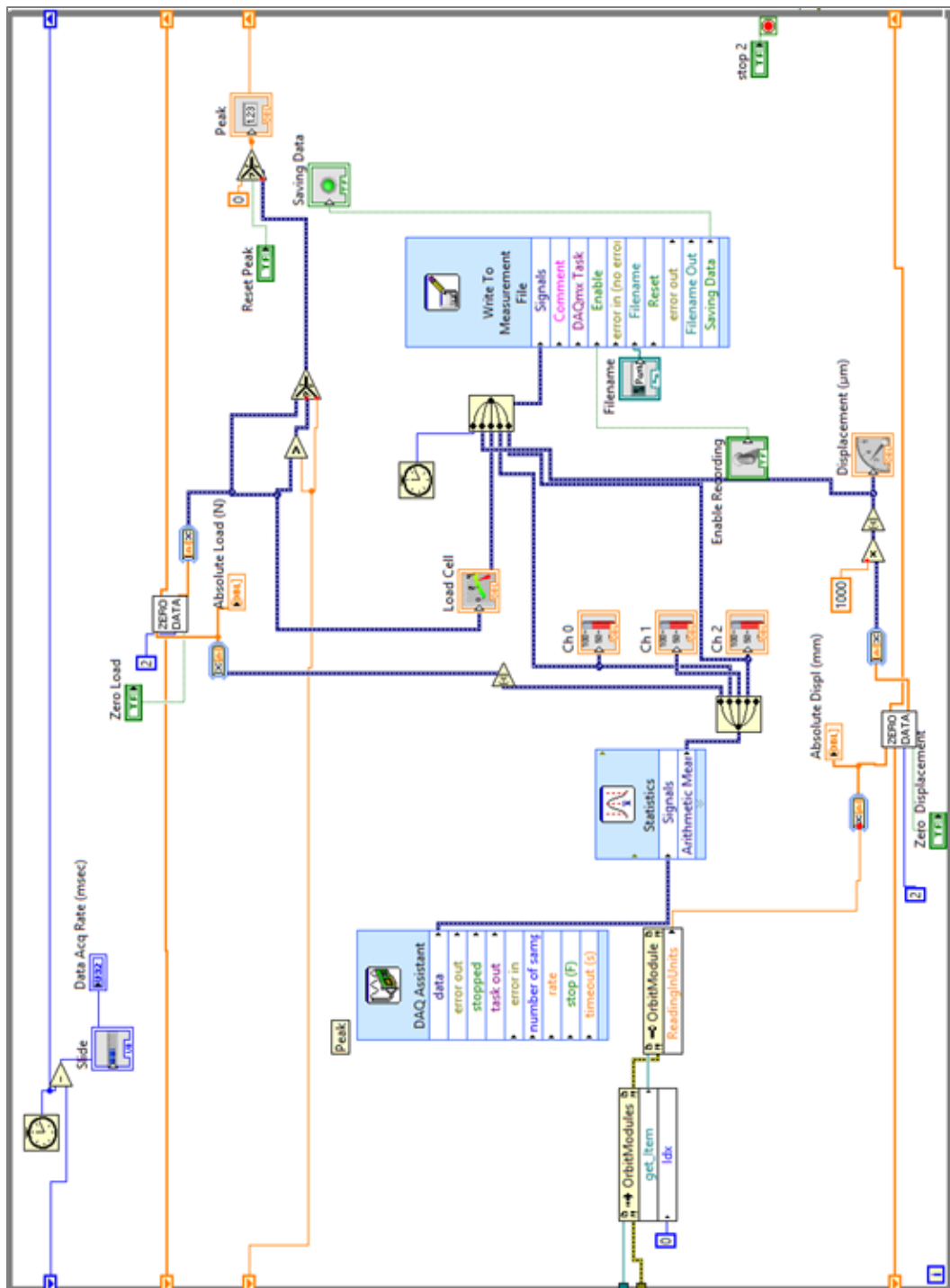
Zachariasen, W. H. (1932) The atomic arrangement in glass. *Journal of the American Chemical Society*, **54**(10), 3841-3851.

Zakharov, D., Pichkov, S. and Shemyakin, V. (2010) *Acoustic emission signal attenuation in the waveguides used in underwater AE testing*. 10th European Conference on Non-Destructive Testing. NDT. Moscow. Vol. 1

Ziemath, E. C., Saggiaro, B. Z. and Fossa, J. S. (2005) Physical properties of silicate glasses doped with SnO<sub>2</sub>. *Journal of Non-Crystalline Solids*, **351**(52-54), 3870-3878.

## Appendix A

### Software Control Interface for Instrumented Macroindentation



Labview Data Acquisition Program

Figure A. 1 Labview program for data acquisition of indentation apparatus.

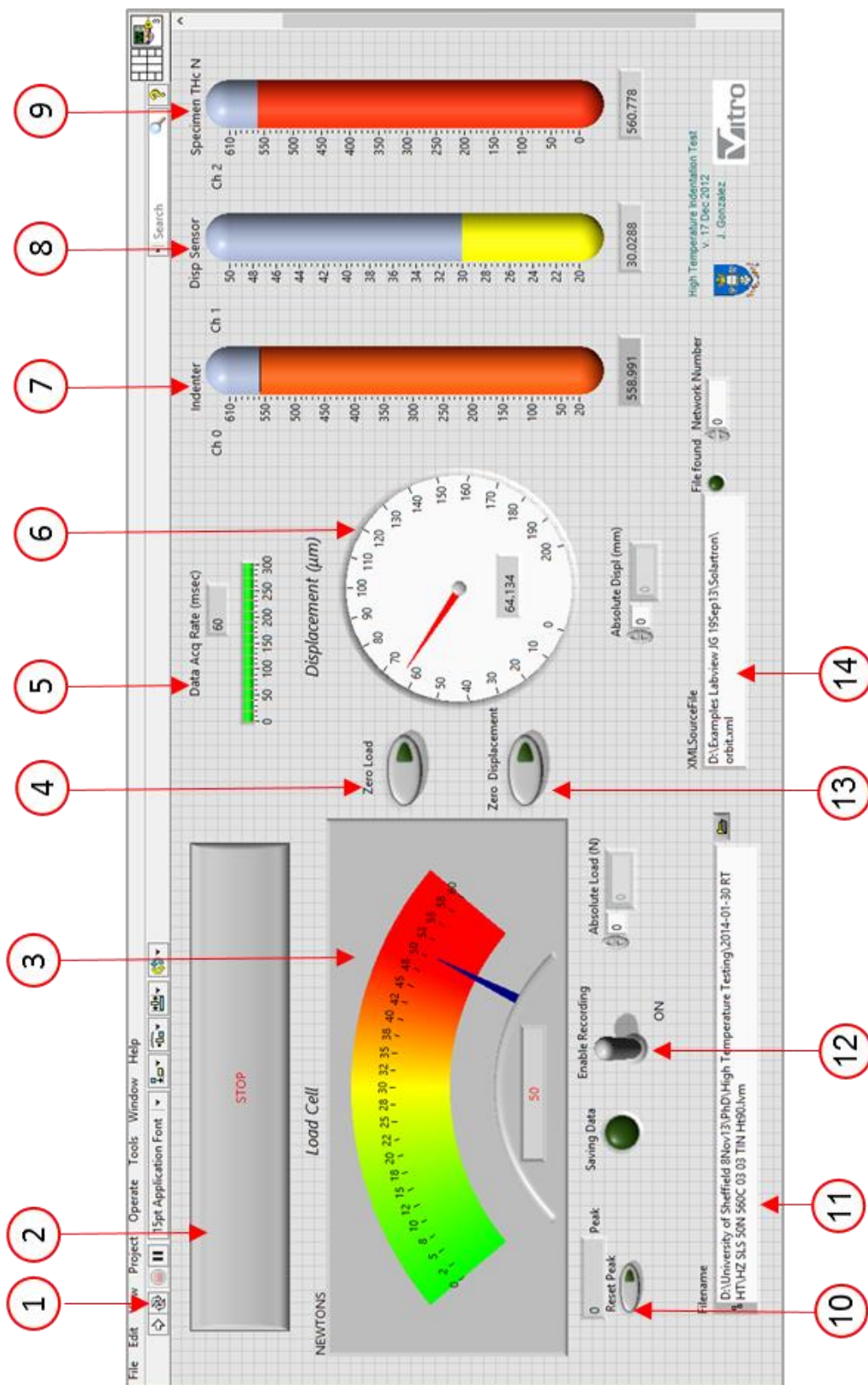


Figure A. 2 Graphical interface for the operation of the data acquisition system

Table A. 1 Description of the controls and indicators of the graphical interface

Index	Description
1	<i>Run</i> – Starts the data acquisition routine
2	<i>Stop</i> – Stops the data recording and the acquisition routine
3	Load indicator.
4	<i>Load Zero or tare</i> -. Adjust to zero the dial indicator and the data that is being recorded.
5	Data Acquisition rate indicator.
6	Displacement indicator
7	Indenter column temperature indicator.
8	Displacement sensor temperature indicator.
9	Specimen temperature indicator.
10	<i>Peak load indicator and reset</i> -. Maximum load reached on each experiment is recorded in this indicator.
11	Field to enter the file name and folder path where the log file will be saved.
12	<i>Enable / disable recording</i> - Enables the data recording to a file during the acquisition routine.
13	<i>DisplacementZero</i> -Adjust to zero the dial indicator and the data that is being recorded.
14	Field to enter the path where the file drivers for the displacement sensor are saved. It is required to initiate the sensor.